2016

Deformation Induced Martensitic Transformation In 304 Stainless Steels

Junliang Liu
University of South Carolina

DEFORMATION INDUCED MARTENSITIC TRANSFORMATION IN 304 STAINLESS STEELS

by

Junliang Liu

Bachelor of Engineering
Nanjing University of Aeronautics and Astronautics, 2013

Submitted in Partial Fulfillment of the Requirements

For the Degree of Master of Science in

Nuclear Engineering

College of Engineering and Computing

University of South Carolina

2016

Accepted by:

Djamel Kaoumi, Director of Thesis

Theodore M. Besmann, Reader

Lacy Ford, Senior Vice Provost and Dean of Graduate Studies

DEDICATION

I dedicate this work to all my family and friends for their unconditional support and encouragement since the first day.

ACKNOWLEDGEMENTS

I want to thank my supervisor, Dr. Djamel Kaoumi, for his guidance and assistance throughout the completion of this research work and for operating the TEM during the in-situ tensile tests. Thanks to his support and guidance, I'm growing more prepared as a professional researcher. Thanks to Mark KirK, Pete Baldo and Ed Ryan for their time and help at IVEM at Argonne National Laboratory.

I also want to thank Dr. Theodore M. Besmann to be the second reader of my thesis. Thanks for his review, suggestions and support. And thanks to all of my professors for their education, guidance and encouragement throughout my time in the Nuclear Engineering program at USC.

Last but not least, I would like to thank my family, friends and colleagues for their help, support and encouragement.

ABSTRACT

304 stainless steel is an austenitic steel widely used for various applications due to a good combination of strength and ductility and relative low cost. It is known to be metastable as the austenite phase can transform into martensite under stress. In this work, a new method (in-situ tensile TEM) and the traditional method (ex-situ tensile tests and TEM, XRD characterization) were used to investigate the mechanisms of deformation-induced martensitic transformation in 304SS samples at different temperatures.

The ex-situ tensile tests were conducted under a strain rate of 10^{-3} s^{-1} until rupture. After the tensile tests, the fractured area was examined under transmission electron microscopy (TEM) evidencing the phase transformation. Some samples were also interrupted after reaching a strain of 7%, 18%, and 30% with the goal of investigating the intermediate microstructure. Such ex-situ investigation can help evidence the changes incurred by the microstructure but provides limited information on the mechanisms and kinetics of the processes leading to that final microstructure. Thus, in complement to the ex-situ investigation, tensile tests were conducted in-situ in a TEM at 25°C down to cryogenic temperatures (-100°C) using a special straining-stage with the goal of capturing the growth of the martensitic phase as it develops under stress in the material and capture it on video. Through such experiments, it was observed that the austenitic phase (fcc) can transform into both ε-martensite (hcp) and α'-martensite (bcc), and ε-martensite (hcp) can be further transformed into α'-martensite (bcc). Stacking faults (SFs) and mechanical twinning are often formed as an intermediate step during the

transformations from γ-austenite to the ε-martensite. Such processes could be observed and recorded in-situ.

Through this work, it was thus shown that in-situ tensile TEM, as a small scale tensile technique, is a good technique to investigate the mechanisms of deformation induced phase transformations.

TABLE OF CONTENTS

DEDICATION iii

ACKNOWLEDGEMENTS iv

ABSTRACT v

LIST OF TABLES ix

LIST OF FIGURES x

LIST OF ABBREVIATIONS xv

CHAPTER 1 LITERATURE REVIEW 1

1.1. Stainless Steels 1

1.2. TRIP/TWIP Steels 2

1.3. 304 Stainless Steels 4

1.4. Martensitic Transformation in 304 and 304L Stainless Steels 6

1.5. Mechanisms of Martensitic Transformation 16

1.6. Motivation for This Study 26

CHAPTER 2 MATERIALS AND EXPERIMENTAL METHODS 28

2.1. Materials 28

2.2. Characterization of As-received Samples 29

2.3. Experimental Methods 32

CHAPTER 3 RESULTS AND DISCUSSION 37

3.1. Mechanical Properties 37

3.2. X-Ray Diffraction (XRD) Characterization of Tested Samples 37

3.3. Ex-situ TEM Microstructure Examination..... 39

3.4. In-Situ TEM Tensile Tests at 25°C..... 48

3.5. In-Situ TEM Tensile Tests at Cryogenic Temperature 66

CHAPTER 4 CONCLUSIONS 72

REFERENCES 75

LIST OF TABLES

Table 1.1 Major use of 304 type stainless steels in kinds of nuclear reactor[12] 4

Table 1.2 Mechanical properties of 304SS at different temperatures[15] 6

Table 1.3 Mechanical properties and fraction of martensite at fracture in 304ss[15] 12

Table 1.4 Summary of possible nucleation sites shown in the figures 20

Table 2.1 Chemical composition of 304 SS and 304L SS in wt. % 28

Table 2.2 Ms and Md30 temperatures of 304 SS and 304L SS 29

Table 2.3 Testing Matrix of 304 sheet and 304L sheet 34

Table 2.4. Parameters set for the electropolishing 34

Table 2.5 Summary of in-situ tensile tests 36

Table 3.1 Mechanical properties of 304 and 304L sheet sample at different temperature 37

LIST OF FIGURES

Figure 1.1 Schematic flow curves with and without TRIP/TWIP effect[7] 3

Figure 1.2 The TTT diagrams for 304 type stainless steels[13] 5

Figure 1.3 Engineering stress strain curve for 304 SS at different temperatures at a strain rate of 1.5×10^{-2} s^{-1}[25] 8

Figure 1.4: (a) Lattice strain of (111) and stress as a function of tensile engineering strain at -63°C.; typical XRD data for (b) zone II and (c) zone III[27] 9

Figure 1.5 Temperature dependence of the kinetic parameters[37] 11

Figure 1.6 Volume fraction of DIM as a function of strain and temperature. Solid curves stand for the theory data. The points stand for the experiment data[37] 12

Figure 1.7 Stress strain curve of 316L sample at different temperatures and the volume fraction of martensite respectively.[38] 13

Figure 1.8 Evolution of α'and ε-martensite volume fraction as a function of strain at 77K[38] 14

Figure 1.9 Engineering stress-strain curve and volume fraction of DIM as a function of true strain at various strain rates of 304ss[23] 14

Figure 1.10 Intensity of austenite and martensite in 304ss as a function of strain and strain rate[24] 15

Figure 1.11 Volume of martensite as a function of strain level at different strain rate in 304ss[24] 16

Figure 1.12 Bain correspondence for martensitic transformation[17, 40] 17

Figure 1.13 The combination of rotation mechanism and Bain strain[15] 17

Figure 1.14 Schematic of γ-austenite → ε-martensite transformation[27] 18

Figure 1.15 Schematic of ε-martensite → α'-martensite transformation[27] 19

Figure 1.16 TEM showing the formation of martensite in austenite at the micro shear-band intersection at SR of 1.0/s[23] 21

Figure 1.17 TEM showing the formation of martensite in austenite at the micro shear-band intersection at strain amplitude of ±0.35%.[18] 21

Figure 1.18 TEM showing the formation of martensite at the interaction of bands of ε-martensite[38] 21

Figure 1.19 TEM showing the formation of martensite at the interaction of bands of ε-martensite[48] 22

Figure 1.20 TEM showing the evolution of ε-martensite and α'-martensite in γ-austenite from isolated shear band at SR of 0.001/s[23] 22

Figure 1.21 TEM showing the evolution of ε-martensite and α-martensite in γ-austenite from isolated shear band at strain amplitude of ±0.85%[18] 22

Figure 1.22 TEM showing the formation of ε-martensite and α'-martensite in γ-austenite at shear band-grain boundary intersection at SR of 0.0001/s[23] 23

Figure 1.23 TEM showing the formation of ε-martensite and α'-martensite in γ-austenite on the parallel shear bands at SR of 0.01/s[23] 23

Figure 1.24 TEM showing the formation of martensite in austenite at grain boundary triple point at strain amplitude of ±0.7%[18] 23

Figure 1.25 TEM showing the formation of martensite in austenite at grain boundary triple point at SR of 0.0001/s[23] 24

Figure 1.26 TEM showing the formation of martensite on twin boundary[38] 24

Figure 1.27 TEM showing the formation of martensite at the twin interactions[49] 24

Figure 1.28 TEM showing the formation of martensite on twin interactions[24] 25

Figure 2.1 XRD pattern of as-received samples 29

Figure 2.2 SEM characterization of as-received (a) 304 sheet and (b) 304L bar samples 30

Figure 2.3 EDX analysis of Cr and Mn enriched carbides shown in 304 sheet 31

Figure 2.4 TEM characterization of as-received 304 sheet and 304L bar sample 32

Figure 2.5 Geometry of tensile specimen (unit: cm) 32

Figure 2.6 Engineering stress-strain curves of (a) 304 sheet 304L sheet at 25°C (b) 304 sheet at 25°C, 50°C and 100°C 33

Figure 2.7 Geometry of in-situ TEM tensile specimen (unit: mm) 35

Figure 2.8 IVEM setup at Argonne National Laboratory and the special straining holder 35

Figure 3.1 X-ray diffraction of 304 sheet samples at different engineering strain level at 25°C 38

Figure 3.2 X-ray diffraction of 304 sheet sample strained at 25°C, 50°C and 100°C 39

Figure 3.3 Stacking faults formed in 7% strained 304 sheet sample 40

Figure 3.4 Formation of ε-martensite with zone axis of [1-210] in γ-austenite with zone axis of [0-11] 40

Figure 3.5 Formation of ε-martensite shear bands with zone axis of [-12-10] and α'-martensite with zone axis of [0-11] in γ-austenite with zone axis of [-112] 41

Figure 3.6 Formation of α'-martensite with zone axis of [00-1] in γ-austenite with zone axis of [-110] 41

Figure 3.7 ε-martensite and α'-martensite formed in γ-austenite matrix in 18% strained 304SS specimen 43

Figure 3.8 ε-martensite and α'-martensite formed in γ-austenite matrix in 30% strained 304SS specimen 45

Figure 3.9 Formation of and α'-martensite with zone axis of [010] and [-111] in γ-austenite with zone axis of [011] 46

Figure 3.10 Formation of ε-martensite shear bands and α'-martensitein in fractured 304 sheet sample 47

Figure 3.11 Steps of formation of stacking faults and α'-martensite in 304L (sample 5) 49

Figure 3.12 Steps of changes of stacking faults in 304L bar (sample 5) 50

Figure 3.13 Formation of ε-martensite shear bands with zone axis of [1-21-3] and [44-83] in γ-austenite with zone axis of [-110] in 304L bar (sample 5) 51

Figure 3.14 Steps of changes of stacking faults in 304L bar (sample 3) 51

Figure 3.15 Shear bands evolution and formation of ε-martensite in 304L bar (sample 6) 52

Figure 3.16 Formation of ε-martensite with zone axis of [000-1] in γ-austenite with zone axis of [1-1-2] in 304L bar (sample 6) 53

Figure 3.17 BF TEM images and SAD of same region at different pulling distance (a) 389.2um (b) 693.8um in 304L bar (sample 1) 54

Figure 3.18 Formation of α'-martensite with zone axis of [0-11] following the formation of ε-martensite with zone axis of [01-1-1] in γ-austenite with zone axis of [0-11] in 304L bar sample (a) 131um (b) 161um (sample 4) 55

Figure 3.19 Formation of ε-martensite shear bands with zone axis of [000-1] in γ-austenite with zone axis of [0-11] and [1-1-2] in 304L bar (sample 5) 56

Figure 3.20 Steps of formation and growth of α'-martensite in 304L bar (sample 5)..... 56

Figure 3.21Bright field TEM of the area followed showing the formation of α'-martensite in 304L bar (sample 5) 56

Figure 3.22 Growth of α' and εmartensite in γ-austenite in 304L bar (sample 6) 57

Figure 3.23 BF taken at pulling distance equal to 471um and SAD from different area revealing the crystal structure of the new phase in 304L bar (sample 6) 58

Figure 3.24 BF and DF TEM showing the matrix and ε-martensite in 304L bar (sample 6) 58

Figure 3.25 Changes of microstructure at different strain levels in 304L bar (sample 6) 59

Figure 3.26 SADs revealing α' with zone axis of [01-1] and εwith zone axis of [2-42-3] and the matrix to be fcc with zone axis of [1-12] in 304L bar (sample 6)..... 59

Figure 3.27 TEM of region 2 in figure 2 showing the growth of α' in 304L bar (sample 1) 60

Figure 3.28 BF, DF TEM and SAD taken from region 2 showing the α' with zone axis of [1-1-1] at pulling distance to be 534.2um in 304L bar (sample 1) 60

Figure 3.29 steps of interface migration in 304L bar (sample 5)..... 61

Figure 3.30 SADs taken from matrix and new phase 61

Figure 3.31 Bright field, dark field TEM and corresponding SAD from the same area at different strain level (a) d=644 um (b) d=811um in 304L bar (sample 2)..... 62

Figure 3.32 Steps of interface motion between α' and γ in 304L bar (sample 2)..... 63

Figure 3.33 BF and DF TEM taken at pulling distance equal to 327um and SAD from the new crystal revealing the crystal structure to be α'-martensite in 304L bar (sample 6)... 64

Figure 3.34 BF and DF TEM taken at pulling distance equal to 327um and SAD from different area revealing the crystal structure in (1),(3) the matrix phase and (2) the new phase in 304L bar (sample 6)..... 65

Figure 3.35 Steps of interface migration between γ and α' in 304L bar (sample 6)..... 66

Figure 3.36 Formation of stacking faults at -50°C in 304L bar in 304L bar (sample 1) .. 67

Figure 3.37 Steps of stacking faults growth at cryogenic temperature in 304(sample 5). 67

Figure 3.38 Steps of stacking faults growth at cryogenic temperature in 304L (sample 4) 68

Figure 3.39 Formation of ε-martensite with zone axis of [52-7-6] in γ-austenite with zone axis of [01-1] and [1-1-1] (a) 39um, 0°C, (b) 56um, -6°C in 304L bar (sample 4)..... 69

Figure 3.40 steps of interface migration in 304L bar (sample 3)..... 69

Figure 3.41 Initial and final position of interface in 304L bar (sample 3)..... 70

Figure 3.42 Formation of α'-martensite with zone axis of [-1-13] in γ-austenite with zone axis of [01-1] and [5-5-8] at pulling distance 189um in 304L bar (sample 3)..... 70

Figure 3.43 Steps of interface migration during cooling process with strain in 304L bar (sample 4) from -14.3°C to -14.9°C 71

LIST OF ABBREVIATIONS

BCC.....Body Centered Cubic

DIM.....Deformation Induced Martensite

FCC.....Face Centered Cubic

HCP.....Hexagonal Close Packing

MT.....Martensitic Transformaion

RT .....Room Temperature

SAM.....Stress Assisted Martensite

SEM .....Scanning Electron Microscopy

SFE.....Stacking Fault Energy

SIM .....Strain Induced Martensite

SR.....Strain Rate

SS .....Stainless Steel

TEM .....Transmission Electron Microscopy

TTT .....Time-Temperature-Transformation

wt % .....weight percentage

XRD .....X-Ray Diffraction

CHAPTER 1

LITERATURE REVIEW

1.1. Stainless Steels

Stainless steels contain principally iron and a minimum of 10.5% chromium[1]. Chromium reacts with oxygen and forms a protective, adherent and coherent oxide layer that envelops the entire surface of the material, which can protect the steels from being corroded in ambient conditions. Additional alloying elements like Ni, Mn can increase the corrosion resistance at elevated temperature[2]. Stainless steels can be divided into five branches by the metallurgical phases present in their microscopic structures[3]:

- Ferritic (bcc structure)
- Martensitic (bct structure)
- Austenitic (fcc structure)
- Duplex steels, consisting of mixture of ferrite and austenite

1.1.1. Effects of Main Alloying Elements on Structure and Properties

Cr: Chromium is by far the most important alloying element in stainless steel production. A minimum of 10.5% chromium is required for the formation of a protective layer of chromium oxide on the steel surface. The strength of this protective (passive) layer increases with increasing chromium content. Chromium prompts the formation of ferrite within the alloy structure and is described as ferrite stabilizer[1].

Ni: Nickel improves general corrosion resistance and prompts the formation of austenite (i.e. it is an austenite stabilizer). Stainless steels with 8-9% nickel have a full austenitic structure and exhibit superior welding and working characteristics compared to ferritic stainless steels. Increasing nickel content beyond 8-9% further improves both corrosion resistance (especially in acid environments) and workability[1, 2].

Mo and W: Molybdenum increases resistance to both local (pitting, crevice corrosion, etc.) and general corrosion. Molybdenum and tungsten are ferrite stabilizers which, when used in austenitic alloys, must be balanced with austenite stabilizers in order to maintain the austenitic structure. Molybdenum is added to martensitic stainless steels to improve high temperature strength[1].

N: Nitrogen can increases strength by solid solution strengthening and enhance resistance to localized corrosion[1].

Cu: Copper increases general corrosion resistance to acids and reduces the rate of work hardening (e.g. it is used in cold-headed products such as nails and screws). It is an austenite stabilizer[1].

1.2. TRIP/TWIP Steels

Material strength and ductility are two main characteristics for structural materials. However, these two properties are always mutually exclusive which makes it a hard task to improve both at the same time. By a combination of several microstructural processes activated during plastic deformation, such as dislocation glide, formation of stacking faults, martensitic phase transformation and mechanical twinning, we can achieve materials with “delayed necking”(i.e. enhance plastic region) [4]. A significance increase of the plasticity is obtained when the martensite and twins are formed during

deformation. This phenomenon is called transformation-induced plasticity (TRIP)[5] or twinning induced plasticity (TWIP) [6].

Figure 1.1 shows the effect of TRIP/TWIP on engineering stress-strain curve[7]. The lower curve describes the mechanical behavior of austenitic steel without martensitic transformation and deformation twinning. The upper curve describes the behavior of the steel with TRIP or TWIP effect. The TRIP/TWIP effect results in an increase of the tensile strength and the uniform elongation of the material simultaneously.

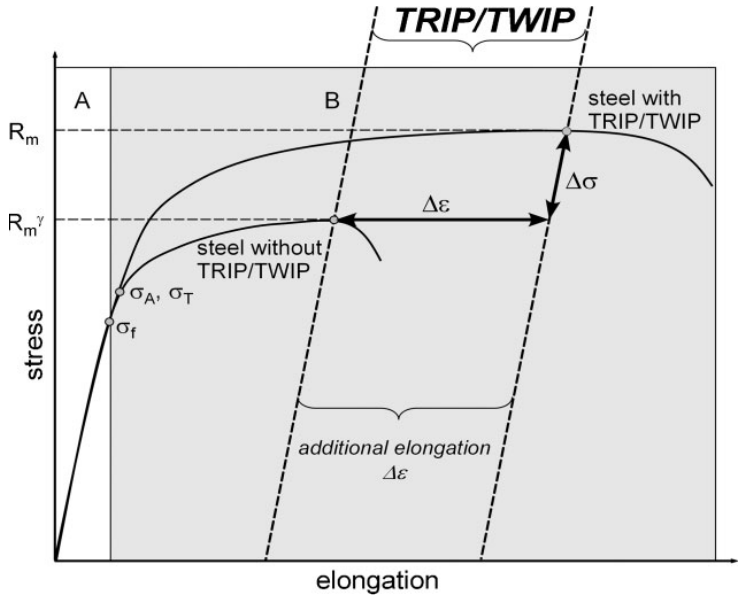

Figure 1.1 Schematic flow curves with and without TRIP/TWIP effect[7]

The metastable stainless steels have an austenitic structure in annealed conditions, but can partially transform into martensite during deformation. Through martensitic transformation, strong phase, ε-martensite and α'-martensite, are formed in the austenitic matrix, which can also serve as the barriers for dislocations motion. Hence, it is important to understand in which conditions the martensite favors. Also, boundaries of deformation induced twin bundles can also act as strong barriers for gliding dislocations, thus leading to a dynamic Hall-Petch effect promoting strain hardening and delaying necking[4, 8].

The deformation mechanism and mechanical properties of FCC metals are related to their stacking faults energy, which changes with the alloy chemical composition, temperature and strain rate etc. At relatively low values of SFE (18-45mJ/m2), TWIP is energetically favorable. And if SFE is lowered even more (<18mJ/m2), TRIP may take place [9, 10]. Details of SFE are discussed later in this chapter. For 304SS, SFE values are lower than 18mJ/m2, which means that TRIP is more favorable to occur.

1.3. 304 Stainless Steels

304SS is an austenitic stainless steels with a face centered cubic (FCC) crystal structure, which shows high corrosion resistance up to 900°C and excellent mechanical properties both at room and elevated temperature. Nevertheless, the use of this alloy is recommended in the 425-850°C range when a good corrosion resistance is required. The density of the alloy is close to 8.03g/cm3. This alloy finds many applications in engineering. The major use of 304 SS in nuclear power plant is listed in Table 1.1[11].

Table 1.1 Major use of 304 type stainless steels in kinds of nuclear reactor[11]

	BWR	PWR	LMFBR	ITER
Components	Control rod container, piping	Control rod container, piping	Pressure vessel, piping, steam generator	Thermal shield, vacuum vessel, ports, vacuum vessel support

Different grades of this alloy exist, 304, 304L and 304H. The main difference between these three grades is the carbon content. Other elements are in basically no difference. 304H has the highest carbon content in the range from 0.04-0.1 wt. %, regular 304 has a carbon concentration between 0.03 wt.% and 0.07 wt.%. 304L has less than 0.03wt. %[12]. 304 and 304L grades stainless steels are used in the current research.

1.3.1. Production Process

The melting of raw materials for 304 stainless steel production is normally performed in an electric arc furnace and the melt is then transferred to a refining vessel. The initial carbon content of the steel in the refining vessel can be as high as 1.5 to 2% and this needs to be reduced by decarburization to levels below 0.04% carbon. Following decarburization, the refined steel is either poured into ingot mold or cast into slabs in a continuous casting machine.

Annealing is performed at about 1100°C followed by air quenching or water quenching to avoid precipitation of unwanted phases. Stress relief annealing is performed at around 400°C for 0.5 to 2 hrs.

TTT curves for a number of 304 stainless steels with a variety of carbon contents are shown in Figure 1.2. Above 900°C, the steels remain completely austenite. From a practical standpoint, the curves show that when annealing or welding, 304SS must be cooled rapidly below the nose of the curves to avoid sensitization and formation of other phases. Lowering the carbon content extends the available time for cooling and makes it easier to avoid sensitization.

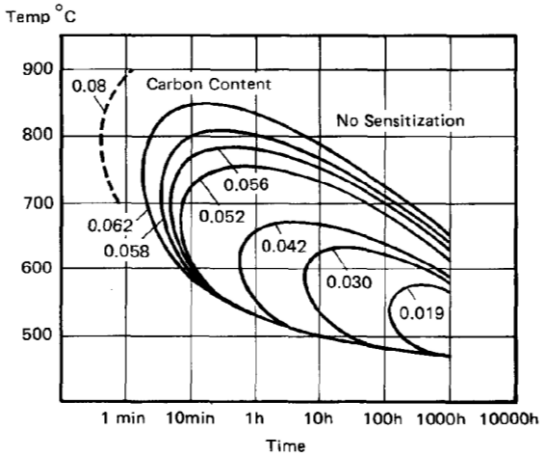

Figure 1.2 The TTT diagrams for 304 type stainless steels[13]

1.3.2. Mechanical Properties

The mechanical properties of 304SS are shown in Table 1.2 for temperatures of interest for this study. Both the yield stress (YS) and ultimate tensile strength (UTS) increase when the temperature decreases. After initial yielding, the stress increases on continued plastic deformation due to the generation of dislocations and interactions of dislocations among themselves and with various types of microstructural barriers. Additionally, deformation induced martensite in the metastable austenitic stainless steels becomes another source of hardening. This transformation is the object of this study.

Table 1.2 Mechanical properties of 304SS at different temperatures[14]

Temperature (°C)	-60	-30	0	25
Yield stress (MPa)	434	393	333	302
UTS (MPa)	1035	914	804	649

The martensite is stronger and harder than the austenitic structure and can also serve as barriers for the dislocation motions, causing a composite-like strengthening and thus a higher strain hardening effect. This strain hardening causes high strengths after cold working and can also contribute to the high ductility in annealed conditions.

1.4. Martensitic Transformation in 304 and 304L Stainless Steels

1.4.1. Terminologies Used in Martensitic Transformation

"Martensite" is named after the German scientist Martens and the term was used originally to describe the hard micro constituents in quenched steels[15].

"Martensitic transformation" is a diffusionless phase transformation that occurs by cooperative atomic movements rather than the long-range diffusion of atoms[16, 17].

"Stacking fault" is a planar crystallographic defect which characterizes the disordering of crystallographic plane. Face-centered cubic structure differs from the

hexagonal closed packed structure only in stacking order. The first two layers are identical for hcp and fcc, which could be labelled as AB. If the third layer is placed directly above the first layer, the stacking will be ABA — this is the hcp structure and it continues as ABABABAB. If it is the forth rather that the third layers that lays directly above the first layer, it will produce the stacking ABCABCABC. In that case, fcc can be transformed into hcp just with the stacking changes.

"Shear band": when ε-martensite (hcp) is formed by overlapping stacking faults, it is finely dispersed and its morphology is heavily faulted. It is difficult to distinguish between single stacking faults, bundles of overlapping stacking faults and ε-martensite. Therefore, the term "shear band" is used to describe the microstructure originating from the formation and overlapping of stacking faults in austenitic stainless steels.[18]

"Deformation induced martensitic transformation" refers to the martensitic transformation that can occur above the temperature Ms (the temperature at which spontaneous transformation will start).

The deformation induced martensitic transformation is separated into two types. In Olson[19], Maxwell[20], Lecroisey[21] and Das[18, 22, 23]'s work, these two types of martensitic transformation are defined as the below descriptions. One is the stress assisted transformation where stress can help to initiate transformation. It has the same nucleation sites and embryos as does the regular spontaneous transformation. Martensite formed from stress assisted transformation is named "stress-assisted martensite" (SAM) and is usually in the shape of plates. The other type is the "strain induced martensitic transformation", which depends on the creation of new nucleation sites and embryos by plastic deformation. In Shen's work[24], the transformation from γ-austenite to α'-

martensite is named strain induced transformation. Transformation from γ-austenite to ε-martensite to α'-martensite is usually named stress induced transformation.

1.4.2. Influence of Martensitic Transformation on Mechanical Properties

Figure 1.3 reveals the stress-strain curves at different low temperatures[25]. When the temperature is below room temperature, during the plastic deformation, it is found that there are two stages, an initial stage of rapidly decreasing strain hardening rate and a second stage of increasing strain hardening rate. The initial stage of rapidly decreasing strain hardening rate occurs with the formation of ε-martensite. The formation of martensitic phases alters the volume of the lattice sites, compromising the specific strain/stress concentration that allows the material to be further deformed. The formation of the ε-martensite relaxes the stress of austenitic grains. And in the second stage, the increasing strain hardening rate corresponds to the formation of α'-martensite. The martensite can accommodate a large amount of strain and dissipates local stress concentrations, promoting uniform tensile deformation [25-27].

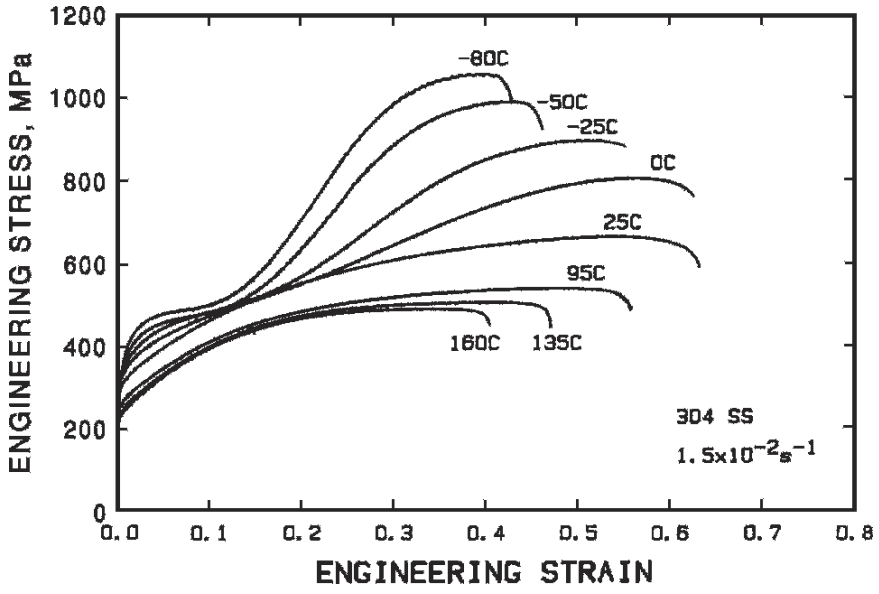

Figure 1.3 Engineering stress strain curve for 304 SS at different temperatures at a strain rate of 1.5×10^{-2} s^{-1}[25]

Li[27] conducted XRD characterizations of 304 in different straining stage at -63°C. XRD patterns in his research are shown in Figure 1.4. By analyzing XRD data from zone I, II and III, ε-martensite seems to be forming at low strain in the 2-8% strain range (zone II) which corresponds to the initial rapid decrease of work hardening rate. And α'-martensite is formed at strains above 8% which corresponds to the increasing strain hardening rate. In addition, in the very initial stage, 0-2% (zone I), no martensite is observed. In De's research, it is reported that the ε-martensite is formed in the range up to 15% strain and the range increase with lower temperature[25].

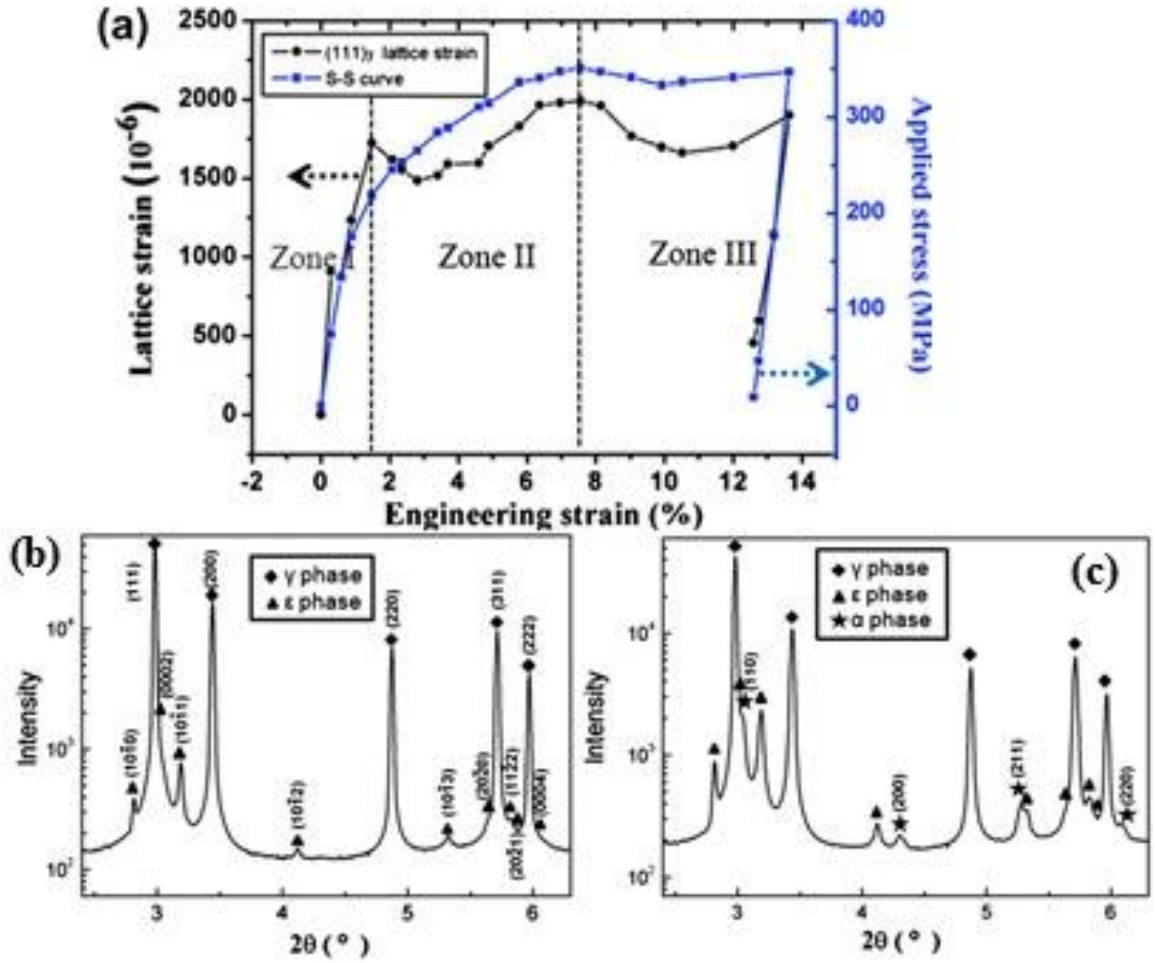

Figure 1.4: (a) Lattice strain of (111) and stress as a function of tensile engineering strain at -63°C.; typical XRD data for (b) zone II and (c) zone III[27]

The extent of deformation induced martensite formation depends on several factors such as: material chemistry, temperature, plastic strain, strain rate, deformation mode, grain size, grain orientation, etc.[18].

1.4.3. Influence of Temperature on Martensitic Transformation

M_S, M_d and M_{d30} are used to estimate the austenite stability [17, 28]. M_S temperature refers to the temperature at which spontaneous transformation will start. The M_d temperature is the limit for deformation induced martensitic transformation, and no martensite can form above this temperature. M_{d30} is the temperature where 50% of martensite has been formed at 30% true strain. This temperature is a good measure of the stability of the metastable stainless steels. Multiple empirical formulas have been developed to estimate the austenite stability by the specific parameters of the M_S and M_{d30} temperature.

$$M_{S,Eichelmann} = 1350 - 1665(C+N) - 28Si - 33Mn - 42Cr - 61Ni \text{ [29] (1.1)}$$

$$M_{S,Monkman} = 1182 - 1456(C+N) - 37Cr - 57Ni \text{ [30] (1.2)}$$

$$M_{S,Pickering} = 502 - 810C - 1230N - 13Mn - 30Ni - 12Cr - 54Cu - 46Mo \text{ [31] (1.3)}$$

$$M_{d30,Angel} = 413 - 462(C+N) - 9.2Si - 8.1Mn - 13.7Cr - 9.5Ni - 18.5Mo \text{ [32] (1.4)}$$

$$M_{d30,Gladman} = 497 - 462(C+N) - 9.2Si - 8.1Mn - 13.7Cr - 20Ni - 18.5Mo \text{ [33] (1.5)}$$

$$M_{d30,Sjoberg} = 608 - 515C - 821N - 7.8Si - 12Mn - 13Cr - 34Ni - 6.5Mo \text{ [34] (1.6)}$$

$$M_{d30,Nohara} = 551 - 462(C+N) - 9.2Si - 8.1Mn - 13.7Cr - 29(Ni+Cu) - 18.5Mo - 68Nb$$

[35] (1.7)

$$M_{d30,Nohara,GS} = M_{d30,Nohara} - 1.42(v-8), v = ASTM\ \ No. \text{ [36] (1.8)}$$

Where the alloying elements are in weight percentage.

It is obvious that the stability of austenite increases along with increasing amount of alloying elements. Among the alloying elements, carbon and nitrogen have the largest influence on austenite stability.

According to [37], during deformation, the relationship between the volume fraction of DIM and the plastic strain can be shown like the equation below.

$$f^{\alpha'} = 1 - \exp\{-\beta[1-\exp(-\alpha\varepsilon)]^n\} \text{ where } \beta = \frac{\overline{v^{\alpha'}} k_p}{(\overline{v^{sb}})^n} \text{ [37]}$$

α and β have a function of temperature so that we can say the volume fraction also depends on temperature. The α parameter is temperature sensitive due to its dependence on stacking-fault energy. The β parameter is proportional to the probability that an intersection of shear bands will form the embryo, and this probability is temperature dependent through its relation to the chemical driving force.

The parameter α and β as a function of temperature is shown in Figure 1.5. The volume fraction of DIM in 304ss as a function of temperature and plastic strain is shown in Figure 1.6. From these two figures, we can say that when the temperature is above 50°C, little martensite is formed in 304ss.

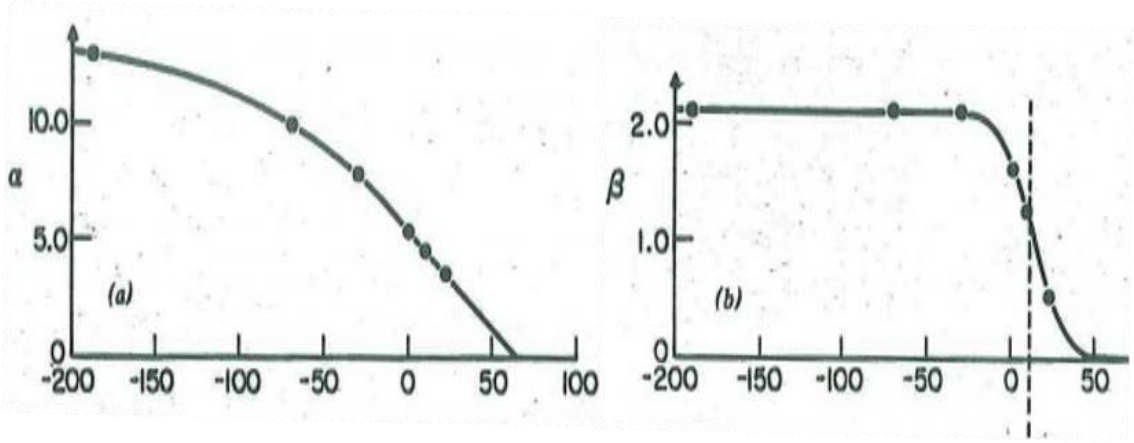

Figure 1.5 Temperature dependence of the kinetic parameters[37]

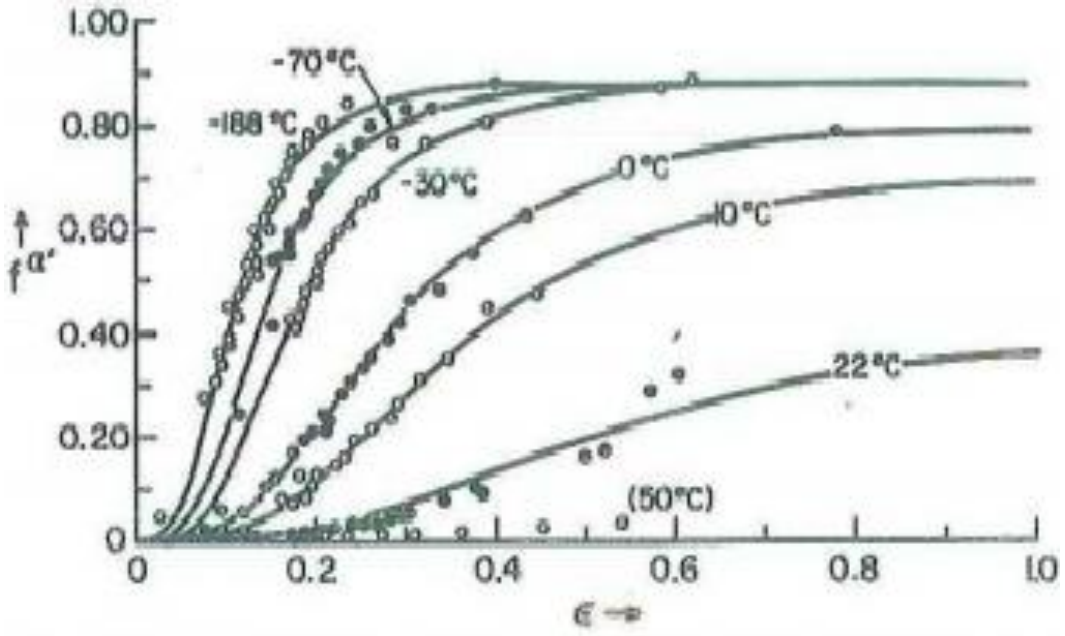

Figure 1.6 Volume fraction of DIM as a function of strain and temperature. Solid curves stand for the theory data. The points stand for the experiment data[37]

Table 1.3, we can see the decreasing of volume fraction of martensite along with the increasing temperature in the fracture samples.

Table 1.3 mechanical properties and fraction of martensite at fracture in 304ss[14]

Temperature(°C)	Yield stress(MPa)	UTS(MPa)	EL (%)	ξ(FE-%) at fracture
-60	434	1035	70	48.1
-30	393	914	84	44.9
0	333	804	96	35.4
25	302	649	92	9.4

This is similar to observation done on 316L stainless steels. Spence has reported the volume fraction of martensite in 316L stainless steel as a function of temperature and strain[38].

Figure 1.7 shows the mechanical response of 316L stainless steel deformed at different temperatures and the amount of martensite fraction when the sample is in necking process. The tensile test strain rate is $5*10^{-4}$/s. At 450 K, there is no martensite

formed. And reducing the deformation temperature results in an increase in the content of martensite formed. It also shows that the form of the engineering stress-strain curve tends to an S shape with decreasing temperature[38].

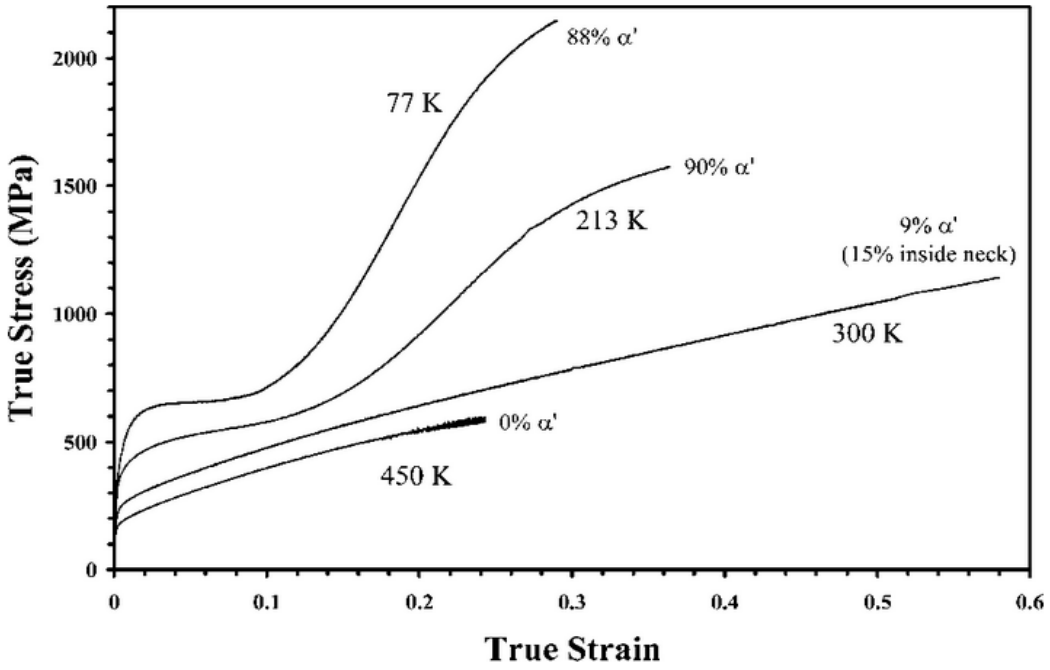

Figure 1.7 Stress strain curve of 316L sample at different temperatures and the volume fraction of martensite respectively.[38]

Especially for the sample deformed at cryogenic temperature, there are 2 steps of deformation. Again, it is believed that the first step, low strengthening rate, is due to the formation of ε-martensite. Due to the low stacking fault energy at 77K (~10mJ/m^2)[21], the martensite transformation prefers to follow the indirect way. From Figure 1.8 we can see that at the beginning of the deformation, the increasing rate of α'-martensite is low, however after the ε martensite volume fraction reaches a maximum, the volume fraction of ε-martensite begins to decrease and meanwhile the α'-martensite volume fraction becomes very high at an increasing rate. Compared Figure 1.6 and Figure 1.7, we can find that the flat part in the engineering stress-strain curve is mainly related to the increasing formation of ε-martensite.

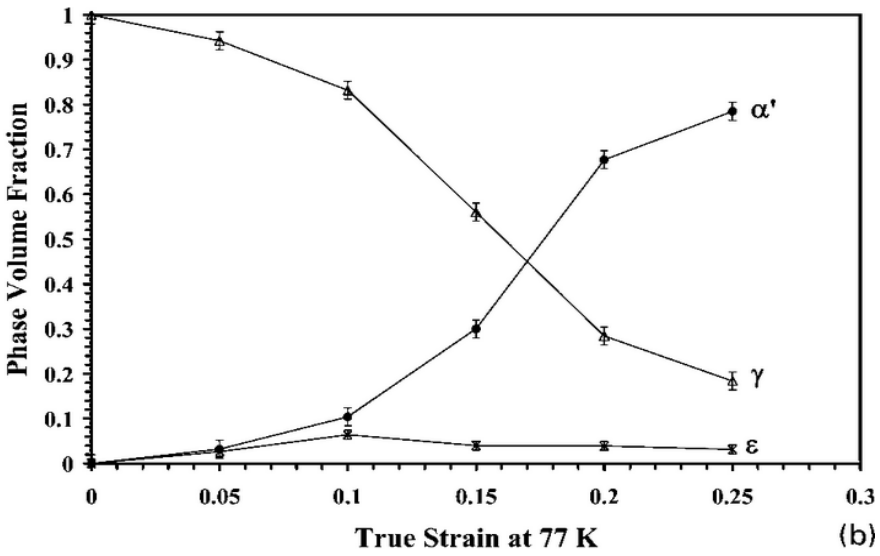

Figure 1.8 Evolution of α'and ε-martensite volume fraction as a function of strain at 77K[38]

1.4.4. Influence of Strain Rate on Martensitic Transformation

Figure 1.9 shows the engineering stress-strain curves and volume fractions of martensite at different strain rates from a study done by Das[23].

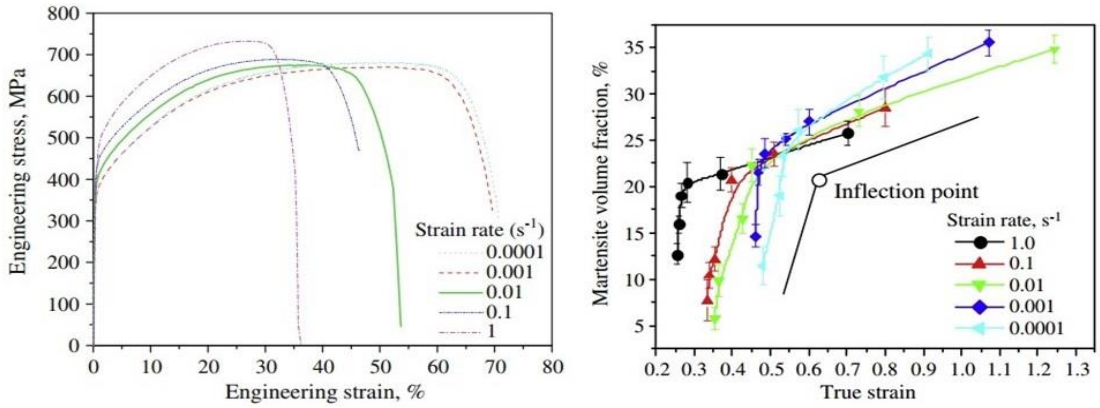

Figure 1.9 Engineering stress-strain curve and volume fraction of DIM as a function of true strain at various strain rates of 304ss[23]

While the increasing strain rate can favor martensite formation at low strain level, the maximum amount of martensite formed due to tensile deformation is reduced with increasing SR[23]. This is mainly attributed to the local variation of SFE of the material. A possible explanation is that at the higher strain rate, the heat of deformation is retained

in the specimen and temperature increases during plastic deformation. Austenite stability may increase because of this, and less martensite is formed[39].

The extent of martensitic transformation can also be shown by the intensity of peaks in XRD pattern in Figure 1.10. From Figure 1.10, we can find that low SR can enhance the martensitic formation. When the strain is higher than 40%, the extent of martensitic transformation under low strain rate is higher than that under high SR[24].

One may also observe that there is a difference in measured martensite volume fractions between XRD and EBSD which is shown in Figure 1.11[24]. The results measured from XRD is consistently higher than that from the EBSD measurement. Two reasons may cause the discrepancy. One is the limited resolution of SEM in EBSD measurement which may lose sights of some fine martensite particles. The other one is that the X-ray can go farther than the electrons so that the EBSD can only give the information close to the surface. As a result, the amounts measured by XRD is larger than those by the EBSD[24].

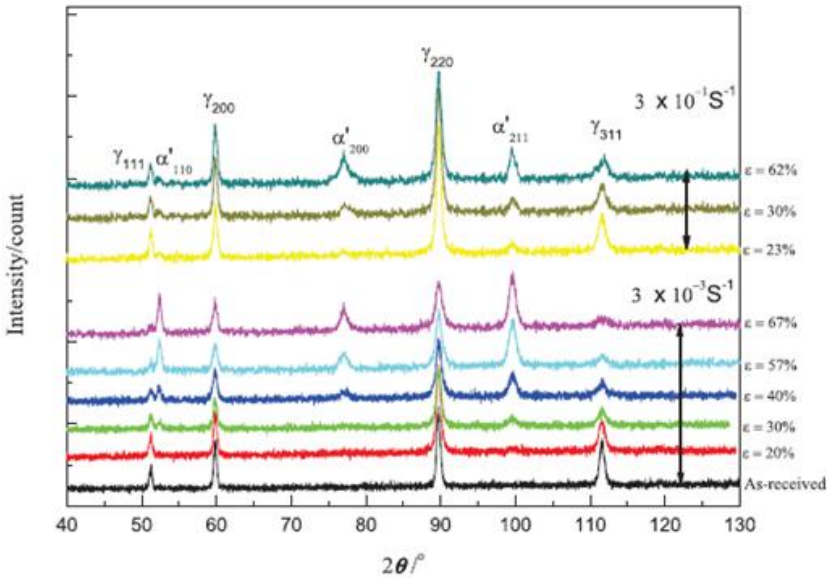

Figure 1.10 Intensity of austenite and martensite in 304ss as a function of strain and strain rate[24]

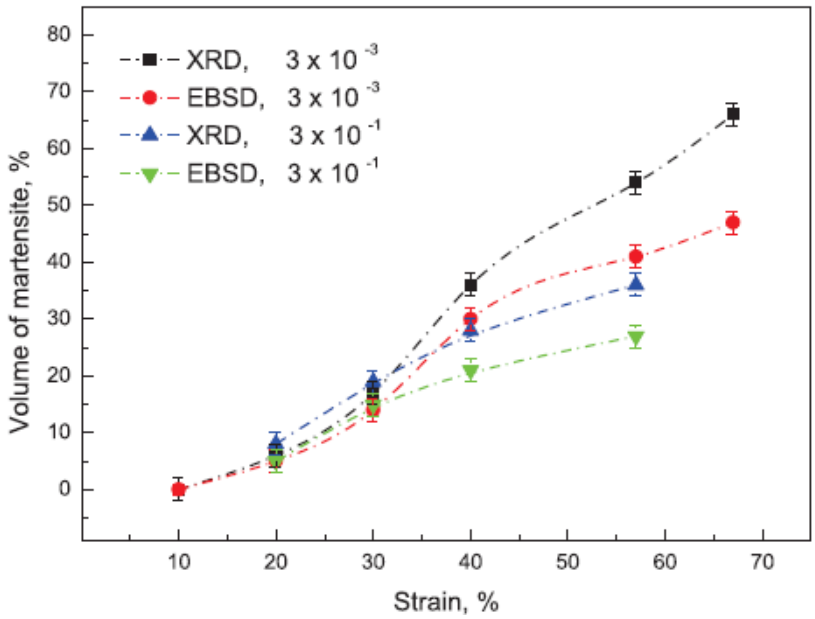

Figure 1.11 Volume of martensite as a function of strain level under different strain rate in 304ss[24]

1.5. Mechanisms of Martensitic Transformation

Martensitic transformation is diffusionless. The speed of transformation is rapid; it can happen at extremely low temperature and during the transformation, there is no chemical composition change.

From literature review, there are two paths that the transformations can follow

Direct way: γ-austenite → α'-martensite

Indirect way: γ-austenite → ε-martensite → α'-martensite

1.5.1. Mechanism of "γ-austenite → α'-martensite"

Bain introduced a theory on how to transform the face-centered cubic austenite, to the body-centered cubic or body-centered tetragonal α'-martensite by a cooperative movement of atoms. The Bain theory was adopted, because it theoretically demonstrated the martensitic transformation by minimum of atomic movements. Figure 1.12 shows the schematic process of Bain strain.

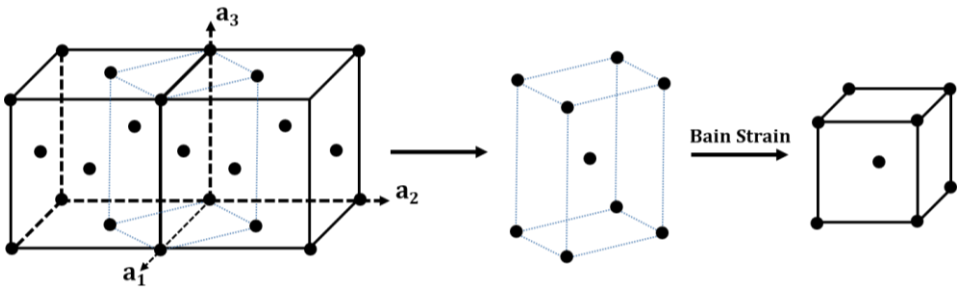

Figure 1.12 Bain correspondence for martensitic transformation[17, 40]

The orientation relationships in the Bain model are:

$$(111)_{\gamma} \Leftrightarrow (011)_{\alpha'}, [101]\gamma \Leftrightarrow [111]_{\alpha'}\ [110]_{\gamma} \Leftrightarrow [100]_{\alpha'}, [112]_{\gamma} \Leftrightarrow [011]_{\alpha'}$$

However, in the experiments, during the transformation between the γ crystal and α' crystal, the interface plane between austenite and martensite which is named the habit plane should stay invariant so that an invariant plane strain is required[15]. In that case the rotation mechanism is introduced to make up Bain Strain model.

Figure 1.13(a) and (b) show the effect of the Bain strain on austenite, which the undeformed austenite is represented as a sphere of diameter wx = yz in three–dimensions. The strain transforms it to an ellipsoid of revolution. Figure 1.13(c) shows the invariant–plain strain obtained by combining the Bain strain with a rigid body rotation through an angle theta[15].

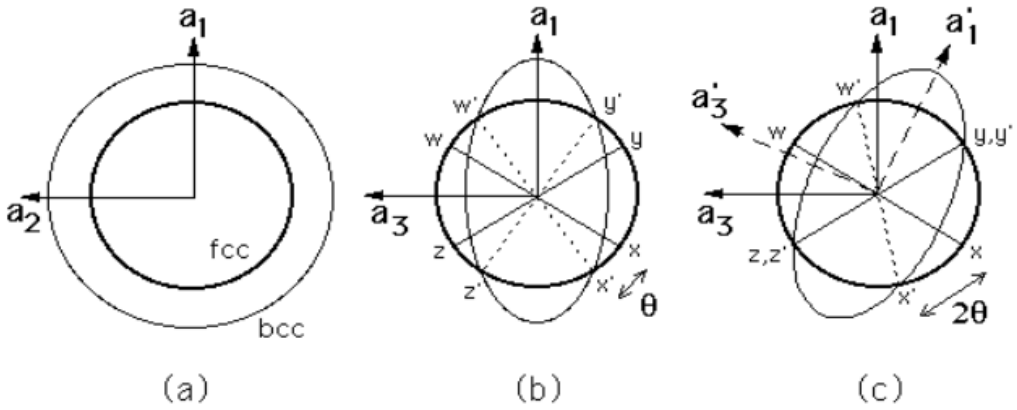

Figure 1.13 The combination of rotation mechanism and Bain strain[15]

In a summary, the Bain theory proposed the mechanism with a minimum of atomic movements. With the rotation mechanism, it can help to explain martensitic transformation theoretically.

The habit plane such as $(225)_\gamma$, $(259)_\gamma$, $(111)_\gamma$ has been reported[41, 42]. And several orientation relationships between austenite and martensite have been reported as

$(111)_\gamma \,||\, (011)_{\alpha'}, [\bar{1}01] \,||\, [\bar{1}\bar{1}1]$ (Kurdjumov and Sachs) [41]

$(111)_\gamma \,||\, (011)_{\alpha'}, [\bar{1}01] \,||\, [001]$ (Nishiyama-Wasserman) [43]

$(111)_\gamma \,||\, (011)_{\alpha'}, [\bar{1}\bar{1}2] \,||\, [0\bar{1}1]$ (Nishiyama) [44]

$(111)_\gamma \overset{1^\circ}{\sim} (011)_{\alpha'}, [\bar{1}\bar{1}2] \overset{2.5^\circ}{\sim} [0\bar{1}1]$ (Greninger-Troiano) [45]

1.5.2. Mechanism of "γ-austenite → ε-martensite"

By adding a partial Shockley dislocation with Burgers vector 1/6[11-2] into two adjoining (111) plane in FCC structure, the hcp structure is obtained which is indicated in Figure 1.14. When the atoms in the first layer are displaced in the [11-2] direction by $a/\sqrt{6}$, the green ones change to orange. The new first layer combines with the lower two layers to compose the new hcp cell [27, 28].

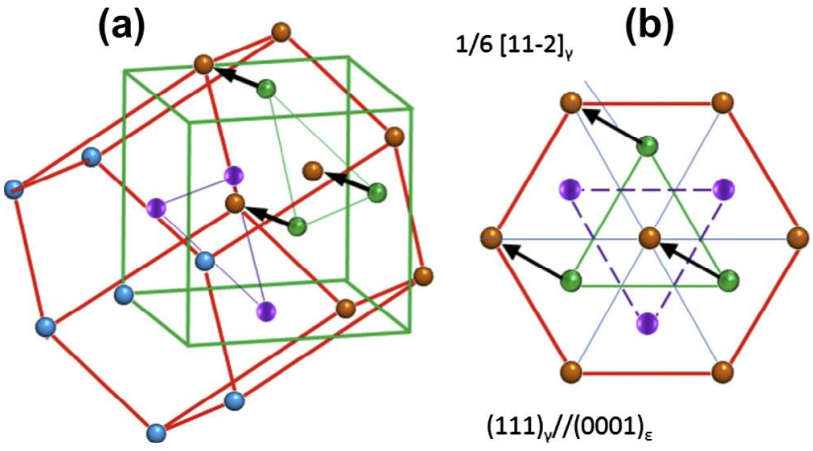

Figure 1.14 Schematic of γ-austenite → ε-martensite transformation[27]

The orientation relationship between ε-martensite and γ-austenite is expressed by Shoji and Nishiyama as Shoji-Nishiyama relation[46, 47]

$(111)_\gamma \,||\, (0001)_\varepsilon, [11\bar{2}] || [1\bar{1}00]_\varepsilon$ or $[1\bar{1}0] || [11\bar{2}0]_\varepsilon$ (Shoji-Nishiyama)

1.5.3. Mechanism of "ε-martensite → α'-martensite"

Figure 1.15 shows the phase transformation mechanism from ε-martensite to α'-martensite. The crystallographic relationship yields (0001) ε (red frame) // (110) α' (blue frame). (2 -1 -1 0) ε is the invariable line; its direction does not change after transformation, but a slight elongation occurs from (2 -1 -1 0)ε to ½(1 1 -1)α', with a corresponding dilatation strain of $\frac{a_{\alpha'}\sqrt{3}}{2a_\varepsilon}$. The vectors (1 1 -2 0) and (-1 2 -1 0) rotate around the [0001] axis, changing the 60° angle (red atoms) to 70.53 and 49.47° (blue atoms), respectively. To adjust the structure of α'-martensite, the distance between the (00 01) ε planes becomes$\sqrt{2}a_{\alpha'}$[27].

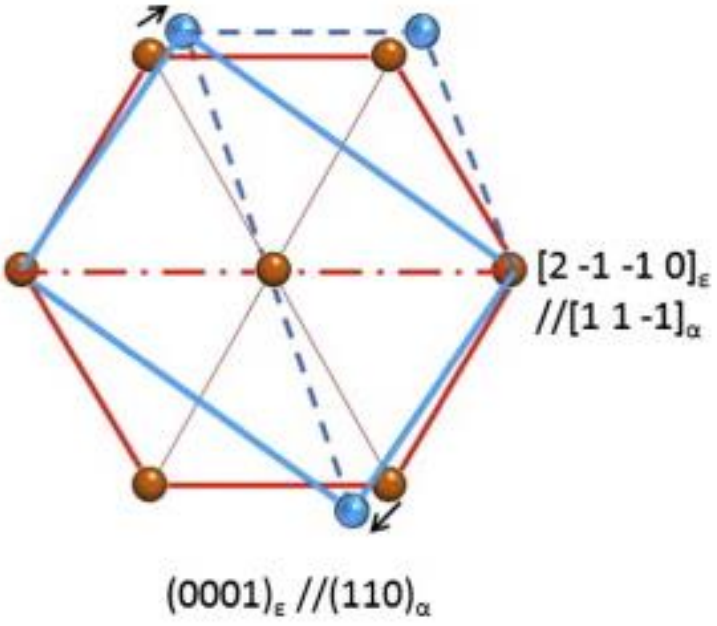

Figure 1.15 Schematic of ε-martensite → α'-martensite transformation[27]

1.5.4. Nucleation Sites

There are several possible nucleation sites of martensitic transformation. In this part, they are summarized based on the literature in Table 1.4 and shown in Figure 1.16 to Figure 1.28.

Table 1.4 Summary of possible nucleation sites shown in the figures

Nucleation sites	Figure #	Reference
shear bands intersection	Figure 1.16	[23]
	Figure 1.17	[18]
	Figure 1.18	[38]
	Figure 1.19	[48]
isolated shear band	Figure 1.20	[23]
	Figure 1.21	[18]
shear band-grain boundary intersection	Figure 1.22	[23]
parallel shear bands	Figure 1.23	[23]
grain boundary triple point	Figure 1.24	[18]
	Figure 1.25	[23]
twin boundary	Figure 1.26	[38]
twin intersection	Figure 1.27	[49]
	Figure 1.28	[24]

Possible nucleation sites of deformation induced martensite were previously characterized by ex-situ TEM, which are shown in Figure 1.16 to Figure 1.28. There are various possible nucleation sites of martensite: shear-band intersections shown in Figure 1.16 (Das, [23]), Figure 1.17 (Das, [23]), Figure 1.18 (Spencer, [38]) and Figure 1.19 (Talonen, [48]), isolated shear-band shown in Figure 1.20 (Das, [23]) and Figure 1.21 (Das, [18]), parallel shear-bands shown in Figure 1.23 (Das, [23]), shear band- grain boundary intersection shown in Figure 1.22 (Das, [23]), grain boundary triple point shown in Figure 1.24 (Das, [18]) and Figure 1.25 (Das, [23]), twin intersection shown in Figure 1.27 (Nishiyama, [49]) and Figure 1.28 (Eichelman, [24]), twin boundary shown

in Figure 1.26 (Spencer, [38]). From literature review, mainly shear band intersections are observed as nucleation sites of martensite.

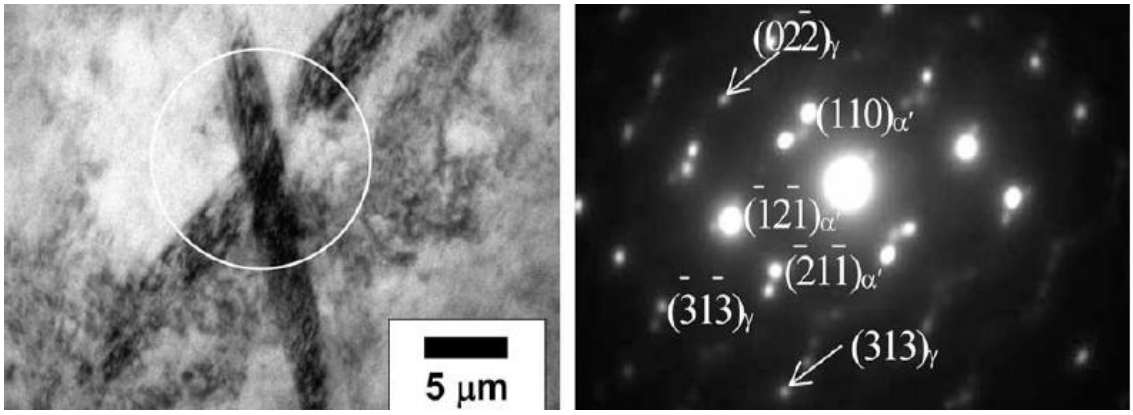

Figure 1.16 TEM showing the formation of martensite in austenite at the micro shear-band intersection at SR of 1.0/s[23]

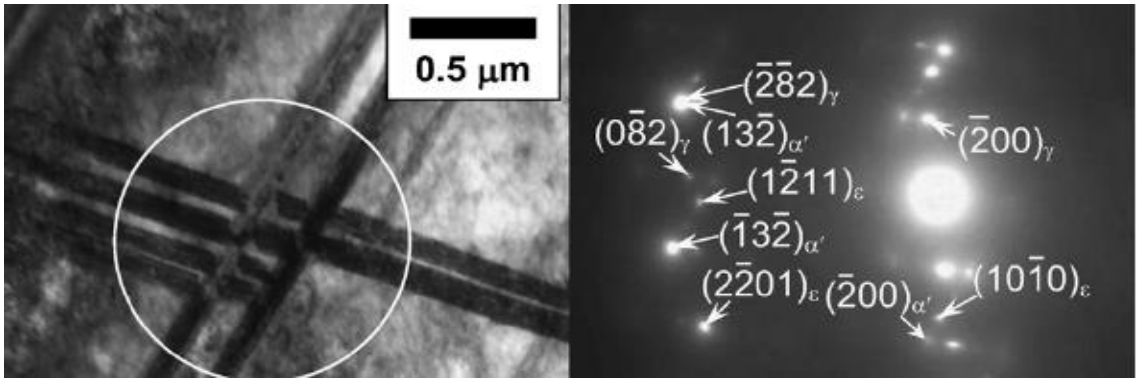

Figure 1.17 TEM showing the formation of martensite in austenite at the micro shear-band intersection at strain amplitude of ±0.35%.[18]

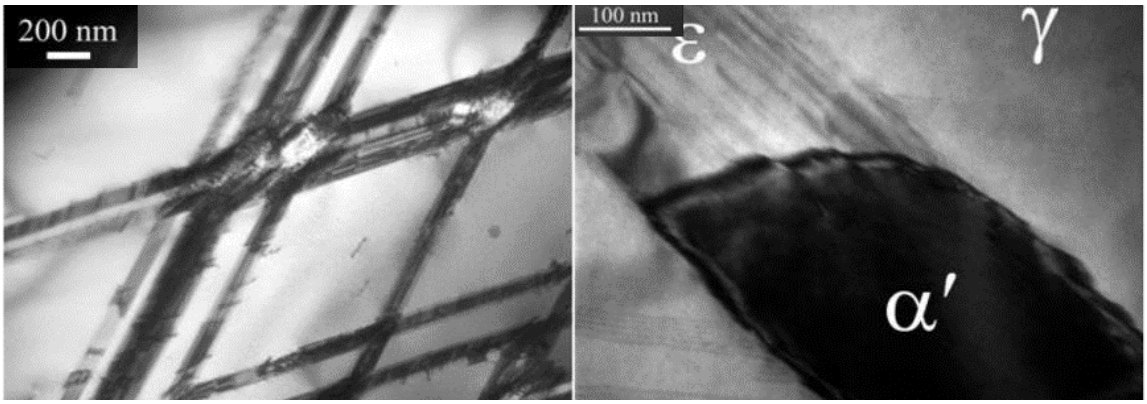

Figure 1.18 TEM showing the formation of martensite at the interaction of bands of ε-martensite[38]

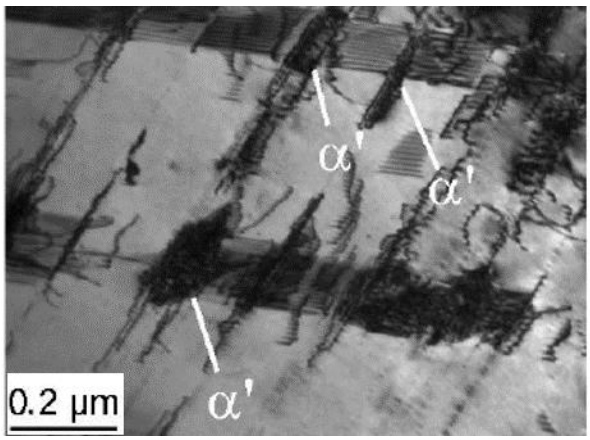

Figure 1.19 TEM showing the formation of martensite at the interaction of bands of ε-martensite[48]

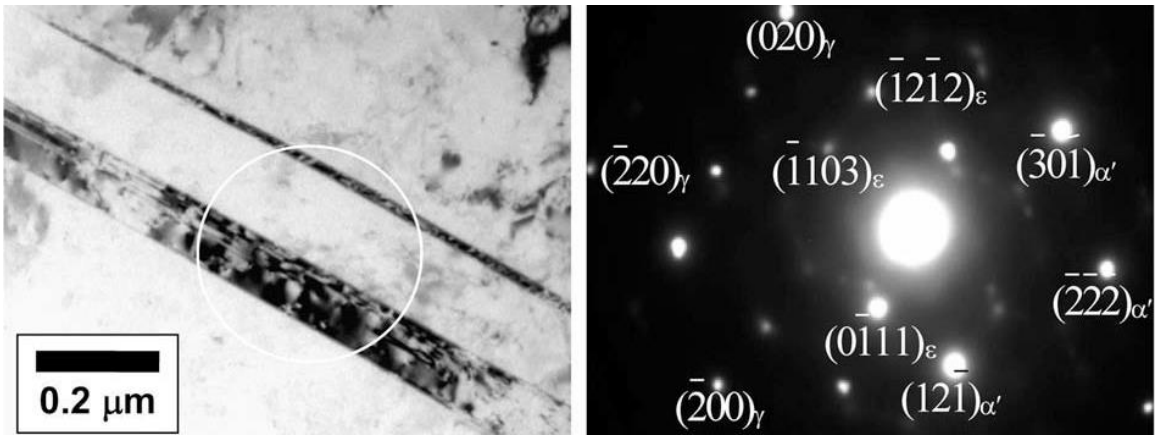

Figure 1.20 TEM showing the evolution of ε-martensite and α'-martensite in γ-austenite from isolated shear band at SR of 0.001/s[23]

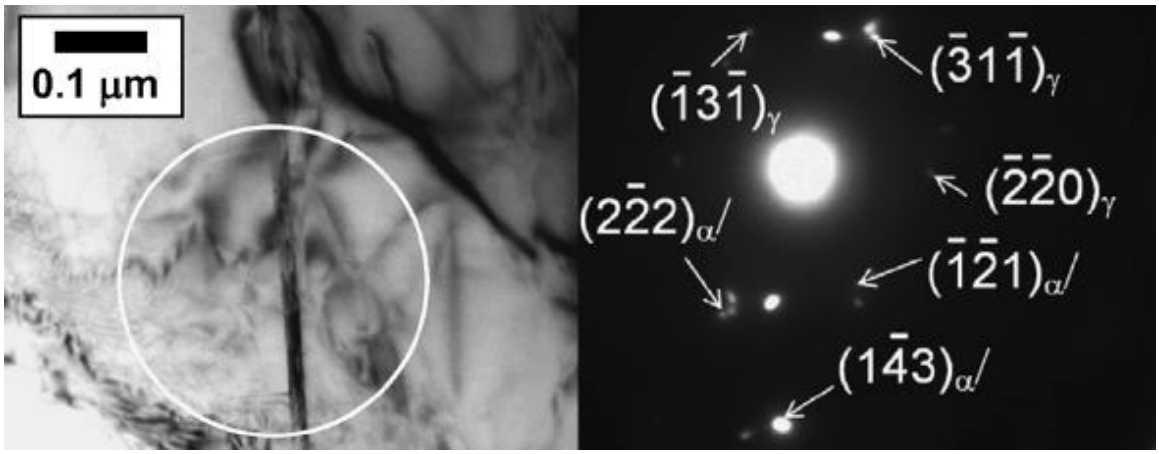

Figure 1.21 TEM showing the evolution of ε-martensite and α-martensite in γ-austenite from isolated shear band at strain amplitude of ±0.85%[18]

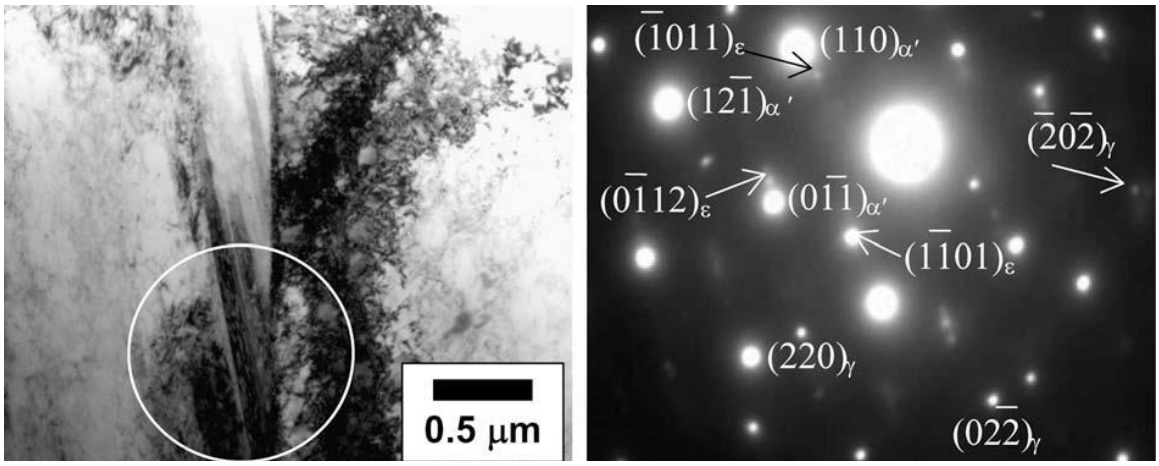

Figure 1.22 TEM showing the formation of ε-martensite and α'-martensite in γ-austenite at shear band-grain boundary intersection at SR of 0.0001/s[23]

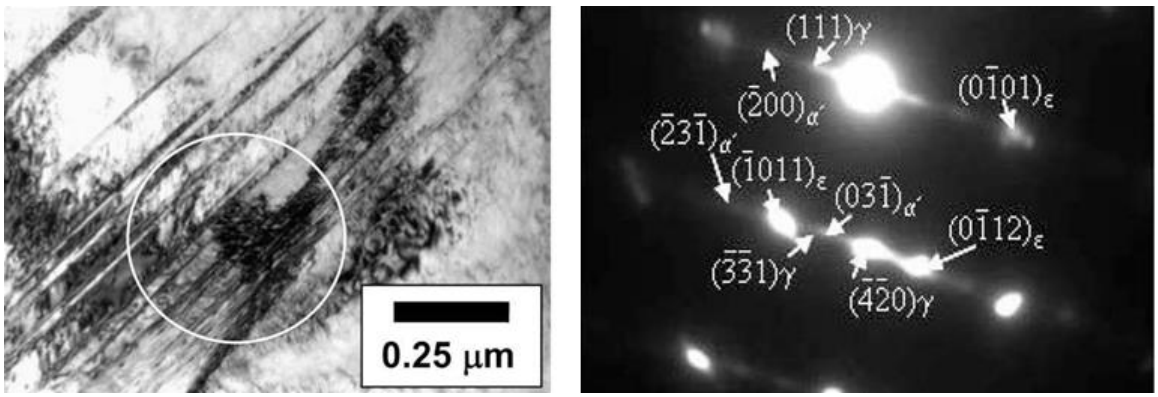

Figure 1.23 TEM showing the formation of ε-martensite and α'-martensite in γ-austenite on the parallel shear bands at SR of 0.01/s[23]

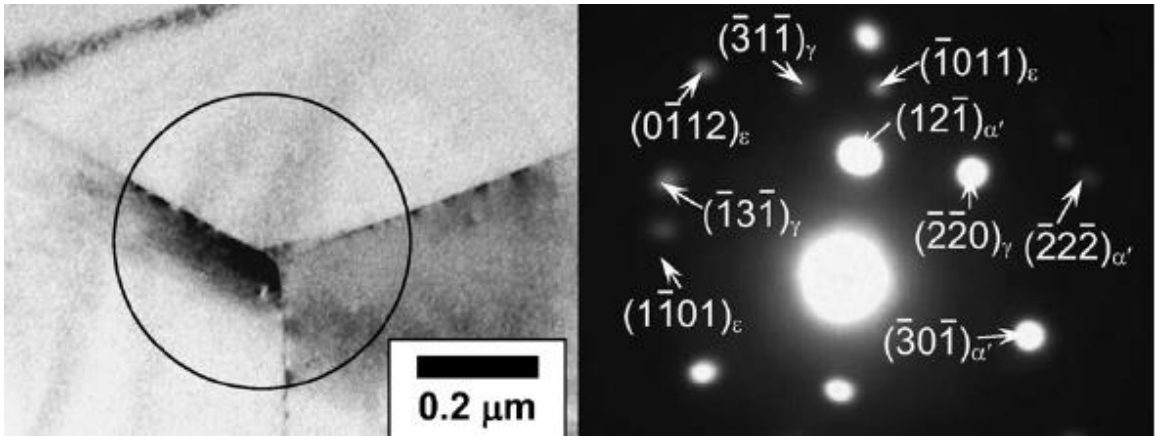

Figure 1.24 TEM showing the formation of martensite in austenite at grain boundary triple point at strain amplitude of ±0.7%[18]

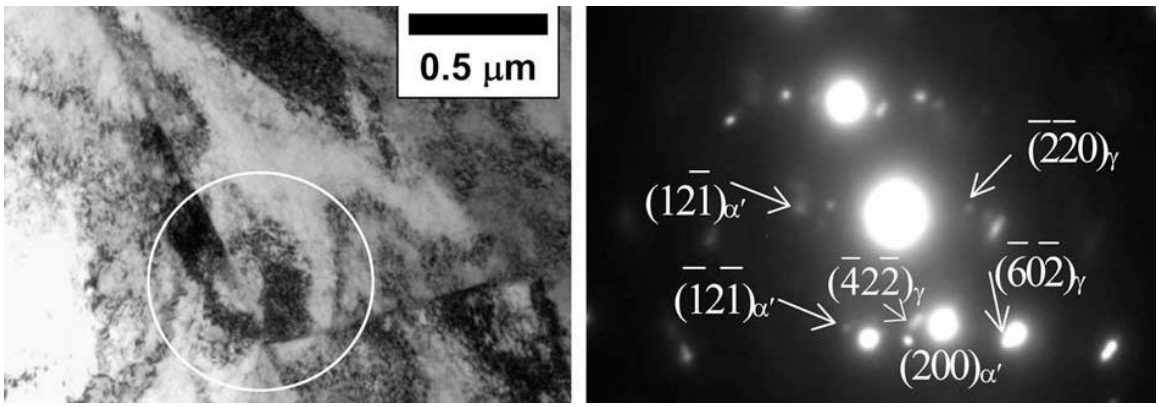

Figure 1.25 TEM showing the formation of martensite in austenite at grain boundary triple point at SR of 0.0001/s[23]

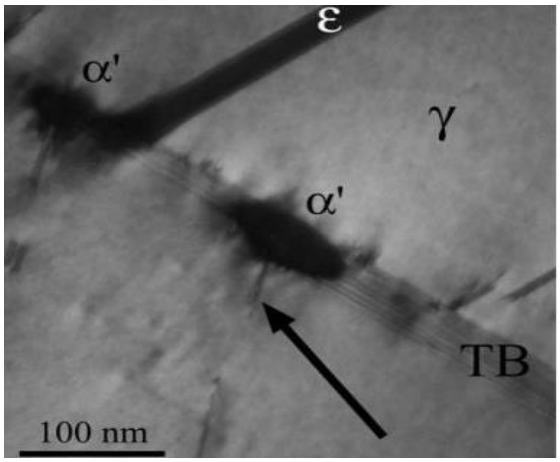

Figure 1.26 TEM showing the formation of martensite on twin boundary[38]

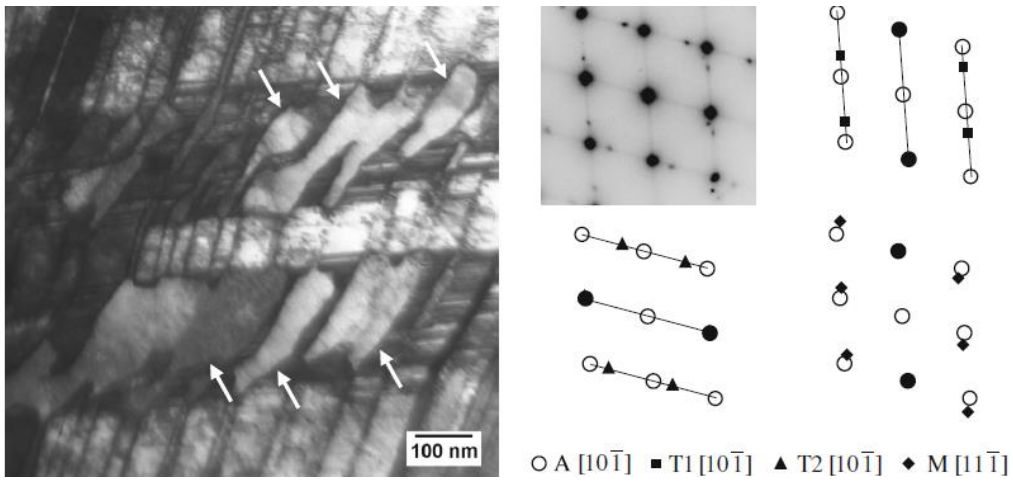

Figure 1.27 TEM showing the formation of martensite at the twin interactions[49]

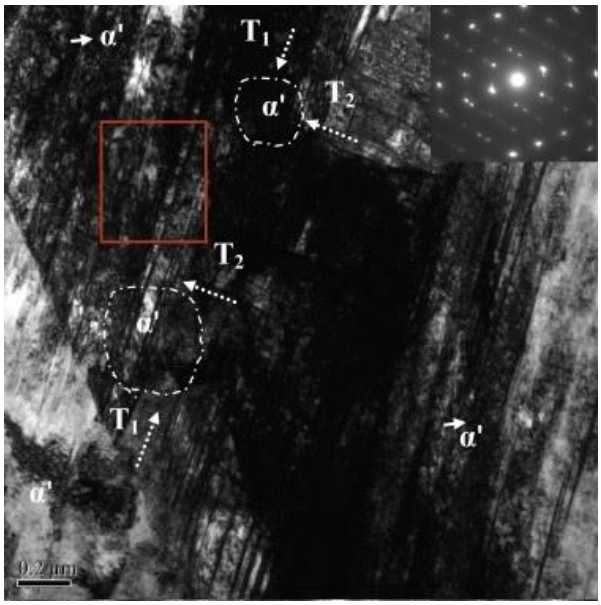

Figure 1.28 TEM showing the formation of martensite on twin interactions[24]

1.5.5. Stacking Fault Energy

Stacking fault energy is a key parameter in the plastic behavior of an alloy. Plastic deformation of high SFE materials (>45mJ·m^{-2}) mainly depends on the dislocation slip, as stacking faults are difficult to form so that it is easy for screw dislocation to cross slip. In contrast, for materials with low SFE (<45mJ·m^{-2}), partial dislocations can exist and originate the stacking fault[24]. In this case, both twinning and ε-martensite arcan form in this range of SFE. The difference between ε-martensite and twinning is the overlapping way of stacking fault. The formation of twinning need stacking faults to overlap on successive (111) planes which requires a high stress to overcome the repulsive forces between the two partial dislocations[50]. Byun[51] has given the critical stress for twinning as

$\sigma_T = 6.14\frac{SFE}{b}$ Where b is the magnitude of the burgers vector of the partial dislocation.

Even the SFE of 304SS is very low, twinning is not easily to be observed, because a very high stress is required.

Compared with twinning, ε-martensite can form directly from the overlapping stacking faults regularly on every second (111) plane. In that case, ε-martensite is more favored to be formed in material with low SFE (<18mJ·m^{-2})

The SFE of 304ss is evaluated as～14mJ/m^2.[24] For 316LN, SFE is valuated 14.2mJ/m^2[51]. Twinning is reported to occur at SFE at a range of 18-45mJ/m^2.[9] The method to calculate SFE can be found in Scharam's literature[52]. The corresponding SFE of austenite steels can be calculated by the below equation

$$SFE(mJ/m^2) = -53 + 6.2 \times Ni + 0.7 \times Cr + 3.2 \times Mn + 9.3 \times Mo \text{ [52]} \quad (1.9)$$

Where the alloying elements are in weight percentage.

SFE also has a dependence on temperature. It has been shown that SFE decreases with the decrease of temperature[53]. High temperature will result in a high SFE. Thus in theory, the transformation at higher temperature should mainly follow the direct sequence, γ→α'. When the temperature is high enough, higher SFE will certainly inhibit the transformation to occur.

1.6. Motivation for This Study

The martensitic transformation in general has been the object of many studies over several decades. Models have been proposed to explain possible mechanisms of the transformation. One limitation in the study of this transformation, as is the case for such phase transformations in general) is the lack of in-situ direct observation to validate underlying hypothesis or to discover the microstructural processes at play, particularly in the nucleation process. Usually experiments are done on bulk samples and microstructure

characterization is done post-experiment to look for clues on how the transformation may have happened. Hence, the usefulness of developing in-situ test capabilities.

In this context, for this particular study, in-situ tensile TEM is used in complement to bulk tensile experiments (carried out to rupture or interrupted) to induce the martensitic transformation in 304 SS and capture the growth of the martensitic phase on video as it develops under stress in the material.

This study is part of an overall effort funded by DOE with the motivation being essentially to demonstrate the feasibility of developing small scale testing methods that (i) allow to reproduce the same phenomenon observed during testing of bulk samples, (ii) to carry out property measurements when possible, and (iii) to use methods that allow in-situ observations to capture and characterize the phenomenon as it happens in the material to gain mechanistic understanding.

CHAPTER 2

MATERIALS AND EXPERIMENTAL METHODS

The chemical composition and characterization of the as-received materials are described in this chapter. The experimental methods including ex-situ testing procedures, sample preparation, and in-situ tensile tests are also presented.

2.1. Materials

304 stainless steel sheets with a thickness of 0.51mm were obtained from Yieh Mau Corp. A 304L stainless steel bar with a radius of 3.2mm bar was manufactured by Phoenix Tube Company. 304L stainless steel sheets with a thickness of 0.635mm were manufactured by North American Stainless.

2.1.1. Chemical Composition

The chemical composition (in wt. %) of materials is shown in Table 2.1. The M_s, M_{d30} and SFE calculated from equation (1.1-1.9) are included in Table 2.2.

Table 2.1 Chemical composition of 304 SS and 304L SS in wt. %

	C	Mn	P	S	Si	Cr	Ni	N	Mo	Cu	Fe
304 sheet	0.042	0.84	0.032	0.003	0.39	18.23	8.09	0.053	0	0	bal.
304L bar	0.03	1.82	0.03	0.04	0.31	18.08	8.02	0.08	0.33	0.41	bal.
304L sheet	0.017	1.723	0.034	0.003	0.368	18.23	8.066	0.084	0.324	0.425	bal.

Table 2.2 M_S and M_{d30} temperatures of 304 SS and 304L SS

Alloy	M_S (°C)			M_{d30} (°C)				SFE(mJ/m^2)
	Pickering	Morkman	Eichelmann	Angel	Giadman	Sjoberg	Nohara	
304 Sheet	-69.6	-92.0	-106.0	32.1	31.2	17.7	12.4	12.6
304L Bar	-139.2	-104.3	-150.5	14.6	14.4	-7.3	-15.7	18.3
304L sheet	-135.7	-99.1	-142.8	16.7	16.0	-6.4	-14.9	18.3

2.2. Characterization of As-received Samples

2.2.1. X-Ray Diffraction (XRD)

X-ray diffraction was used to identify the phases and their relative content in the as-received samples. Samples were mirror polished ending with a 1200-grit surface. X-ray diffraction characterization was conducted on a Rigaku D/Max 2100 powder X-ray diffractometer at USC. Measurements were made from 40° to 85° in a step of 0.02° at a scan rate of 0.12s/step. XRD spectra of as-received samples are shown in Figure 2.1.

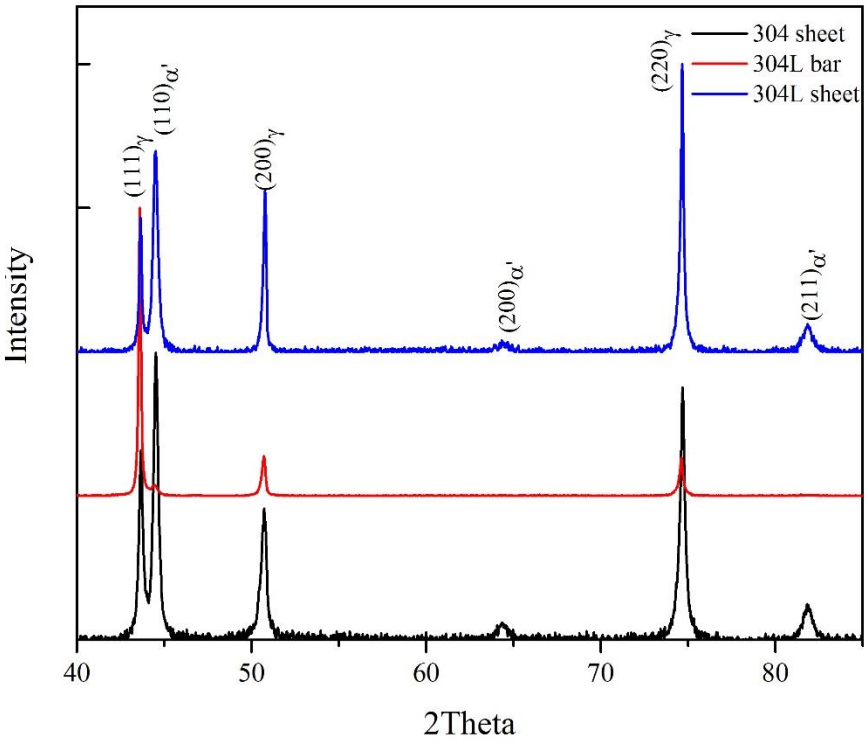

Figure 2.1 XRD pattern of as-received samples

From the spectra shown in Figure 2.1, it could be seen that α' phase is pre-existing in the initial samples. But the content of α'-martensite in 304L bar sample is less than that in 304 and 304L sheet sample which is due to the different processing methods.

2.2.2. Scanning Electron Microscopy (SEM)

The microstructure were revealed by electron polishing and observed with a Zeiss Ultra plus FESEM at USC. Initial microstructures are given in Figure 2.2. The SEM micrograph shown in Figure 2.2 indicates that the microstructure consisted of polygonal grains of austenite with twins interspersed in some grains. The pre-existing martensite is marked by the white arrows.

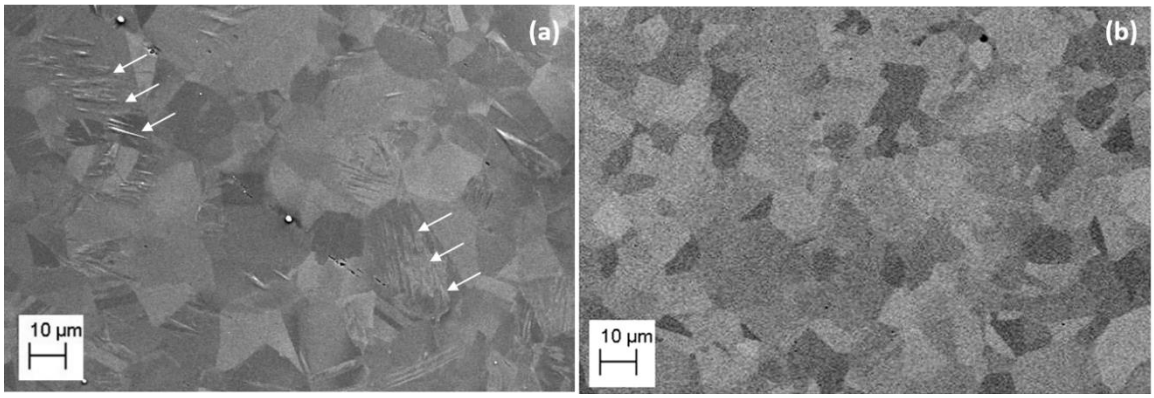

Figure 2.2 SEM characterization of as-received (a) 304 sheet and (b) 304L bar samples

The size of austenitic grains was determined using Image J software. Austenitic grains shown in Figure 2.2 were outlined and scanned into Image J. The software can provide the area of each grains automatically. Then an equivalent diameter of each grain could be derived. The average grain size (equivalent diameter) of 304 sheet and 304L bar shown in Figure 2.2 is about 21um and 24um respectively.

The precipitates in the 304 sheet were found to be essentially carbides rich in in Cr and Mn as shown in the corresponding EDX analysis in Figure 2.3.

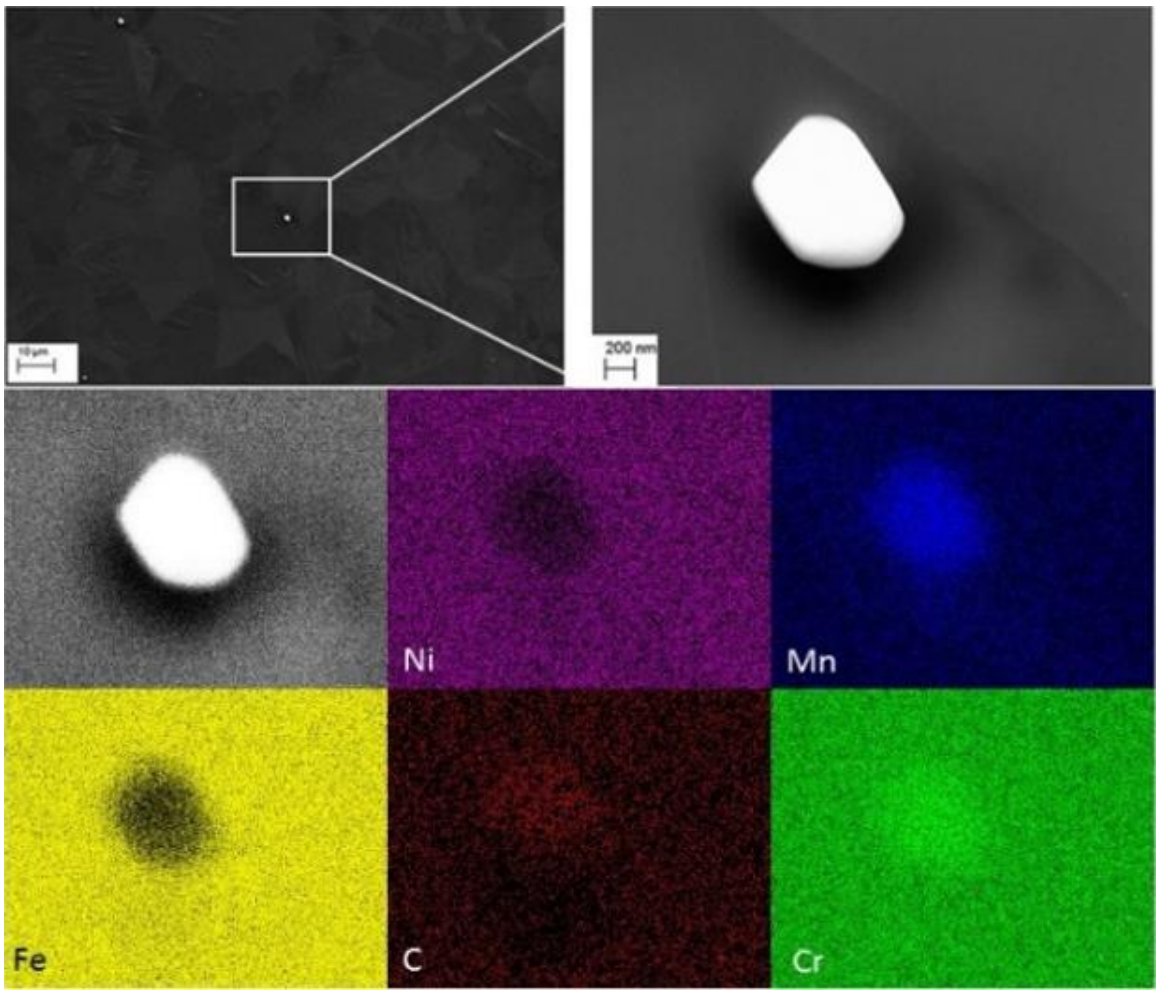

Figure 2.3 EDX analysis of Cr and Mn enriched carbides shown in 304 sheet

2.2.3. Transmission Electron Microscopy (TEM)

TEM characterizations of as-received samples are shown in Figure 2.4.

At low magnification, austenitic grains, dislocations can be observed in both 304 sheet and 304L bar sample. At high magnification, stacking faults are observed to be formed across the austenitic grains which are marked by the dash arrows. Meanwhile, the pre-existing martensite and shear bands could be observed in the 304 sheet sample (marked by the solid arrows) which also agree with the XRD characterization.

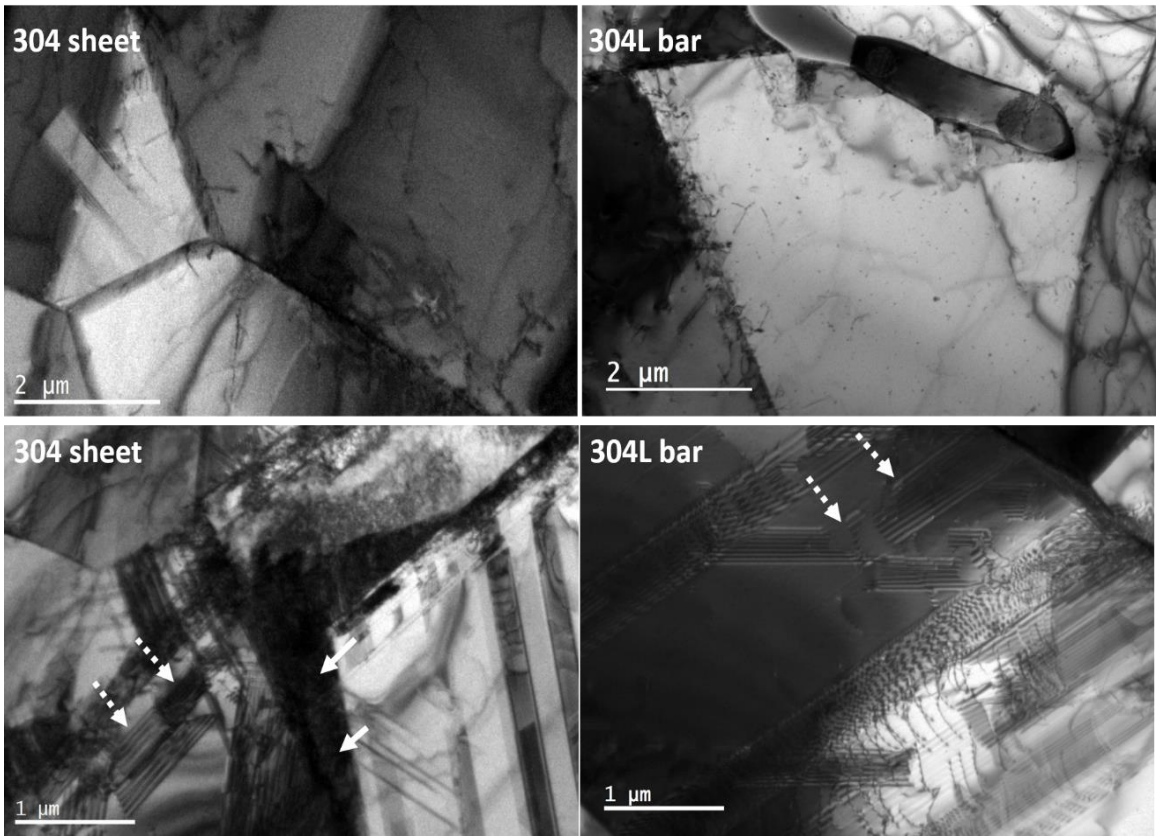

Figure 2.4 TEM characterization of as-received 304 sheet and 304L bar sample

2.3. Experimental Methods

2.3.1. Ex-situ Tensile Tests (bulk tests)

The tensile specimens were machined from 304 sheet and 304L sheet with a dog bone geometry shown in Figure 2.5 by EDM.

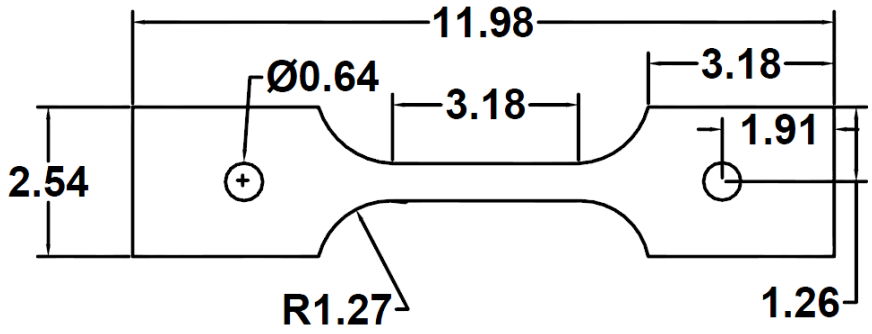

Figure 2.5 Geometry of tensile specimen (unit: cm)

Uniaxial tensile tests were performed on 304 sheet and 304L sheet specimen. Tensile tests were conducted at 25°C under a strain rate of 10^{-3} s^{-1} until rupture in an Instron 5984 machine in laboratory air. The fractured area was then examined under transmission electron microscopy (TEM) to investigate the resulting microstructure. Three tensile samples were interrupted after reaching an engineering strain of 7%, 18% and 30%, with the goal of investigating the intermediate microstructure. To investigate the mechanical properties at high temperature, two tensile tests were run at 50°C and 100°C. The corresponding engineering stress-strain curves of 304 sheet and 304L sheet are shown in Figure 2.6.

The stress-strain curves of 304SS deformed at low temperature have also been reported by De[25] in a similar shape which are shown in Figure 1.3. However, S-S curve of sample deformed at room temperature is not in S-shape anymore which may be due to adiabatic heating caused by the higher strain rate in De's research.

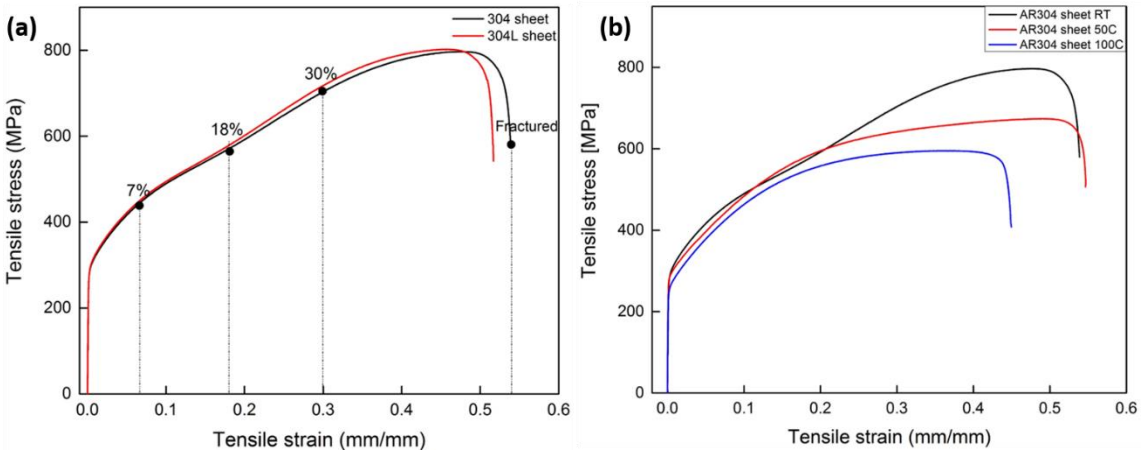

Figure 2.6 Engineering stress-strain curves of (a) 304 sheet 304L sheet at 25°C (b) 304 sheet at 25°C, 50°C and 100°C

The mechanical tests are summarized in Table 2.3 for different samples. And corresponding mechanical properties will be reported in Chapter 3.

Table 2.3 Testing Matrix of 304 sheet and 304L sheet

Material	Temperature (°C)	Strain Rate (S^{-1})	Atmosphere
304 sheet	25	10^{-3}	Air
304 sheet	50	10^{-3}	HP Air
304 sheet	100	10^{-3}	HP Air
304L sheet	25	10^{-3}	Air

2.3.2. TEM Samples Preparation

2.3.2.1. Ex-situ TEM Examination

The fractured area was cut from the tested specimen described in 2.2.1 using a low speed diamond saw. A piece at the center area of samples from the interrupted tests was cut. The sectioned samples were then mounted on aluminum stubs with the adhesive crystal-bond and ground on silicon carbide paper with a water lubricant to remove the burrs and ensure a flat surface. Grinding started with 400-grid paper, followed by 600 grid, 800-grid and end with 1200-grid paper. The final thickness was about 100um. 3mm disks were punched from the ground samples.

Electropolishing was performed on the 3mm disks in a twin jet Struers electro polisher. Electrolyte used in this process was a solution of 5% perchloric acid and 95% methanol. Parameters set for the electropolishing is shown in Table 2.4.

Table 2.4. Parameters set for the electropolishing

Temperature (°C)	Voltage (V)	Current (mA)	Flow rate
~-30	~20	~100	~14

2.3.2.2. In-situ TEM Samples (small scale tests)

The in-situ TEM tensile specimens were machined from 304 sheet and 304L bar as shown in Figure 2.7 by EDM.

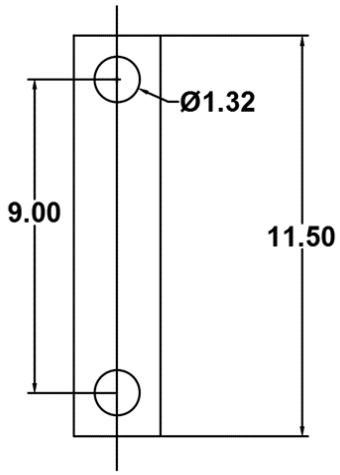

Figure 2.7 Geometry of in-situ TEM tensile specimen (unit: mm)

The specimens were ground using the same method described in 2.2.2.1 to a final thickness of 100um. The ground samples were then electropolished using the same parameters in Table 2.4 and a small hole was formed in the center part which area could be used for the in-situ TEM observation.

2.3.3. In-situ TEM Tensile Tests

In-situ tensile tests were conducted at Argonne National Laboratory (ANL) using the Intermediate Voltage Hitachi H-9000NAR TEM (IVEM). Figure 2.8 shows the IVEM facility and the special Gatan straining holder we used during the in-situ straining tests. The in-situ straining was conducted at 25°C down to -100°C at a pulling rate of about 2.0um/s.

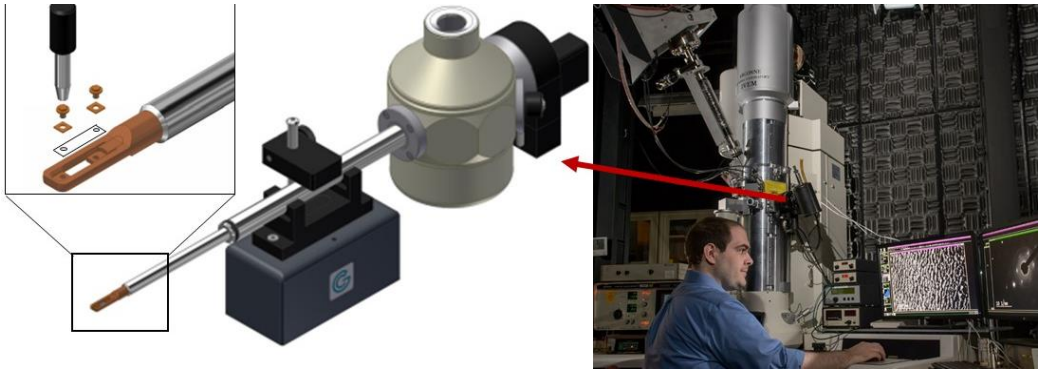

Figure 2.8 IVEM setup at Argonne National Laboratory and the special straining holder

During the in-situ experiments, the observations were recorded in videos in-situ. Occasionally the pulling was stopped when necessary to take to some pictures and diffraction patterns. Using Adobe Premier Pro CS4, pictures showing the evolution of the phase transformation were extracted from the in-situ videos.

A series of in-situ tests were conducted 25°C down to -100°C. The summary of tensile tests are shown in Table 2.5.

Table 2.5 Summary of in-situ tensile tests

Alloy	Conditions	Number of tests
304 sheet	25°C	6
	Cryogenic	6
304L bar	25°C	8
	Cryogenic	5

CHAPTER 3

RESULTS AND DISCUSSION

3.1. Mechanical Properties

Mechanical properties (yield stress, ultimate tensile strength and elongation) are summarized in Table 3.1 for different bulk tensile tests performed.

Table 3.1 Mechanical properties of 304 and 304L sheet sample at different temperatures

Material	Temperature °C	Strain Rate (s^{-1})	Atmosphere	YS (MPa)	UTS (MPa)	Elongation (%)
304 sheet	25	10^{-3}	Air	291.4	797	53.9
304 sheet	50	10^{-3}	HP Air	283.2	674.1	54.7
304 sheet	100	10^{-3}	HP Air	262.2	602	47.7
304L sheet	25	10^{-3}	Air	293.3	802.3	51.6

The 304L and 304 sheets exhibited similar properties at 25°C. As expected the YS and UTS decreased with increasing temperature.

3.2. X-Ray Diffraction (XRD) Characterization of tested samples

Figure 3.1 shows the x-ray diffraction of 304 sheet sample for different engineering strain levels. From 0% straining to 7% straining, there seems to be some reverse phase transformation from α'martensite to γ-austenite as relative intensity of the peaks of martensite e.g. $(110)_{\alpha'}$, $(200)_{\alpha'}$ and $(211)_{\alpha'}$ decreases in relative to the austenite peak e.g. $(200)_{\gamma}$. With further straining, martensitic transformation occurs again and the intensity of all the martensite peaks increase relative to the intensity of the austenite peaks. The expected peak location for the ε-martensite are marked on the pattern shown

in Figure 3.1. Lattice parameter of ε-martensite in pure iron provided by the Powder Diffraction File (PDF) are a_ε=0.245nm, c_ε=0.393nm. However, the lattice parameters of 304SS should be different from those of the pure iron considering the existence of alloying elements so that a deviation of the lattice parameters is allowed. When we set that a_ε=0.24nm, c_ε=0.405nm, the expected peaks of ε-martensite would overlap with those of γ-austenite. The lattice parameters used for the analysis of electron diffraction patterns in later chapter were calculated from the XRD patterns, which are a_γ=0.357nm, $a_{\alpha'}$=0.286, a_ε=0.24nm, c_ε=0.405nm.

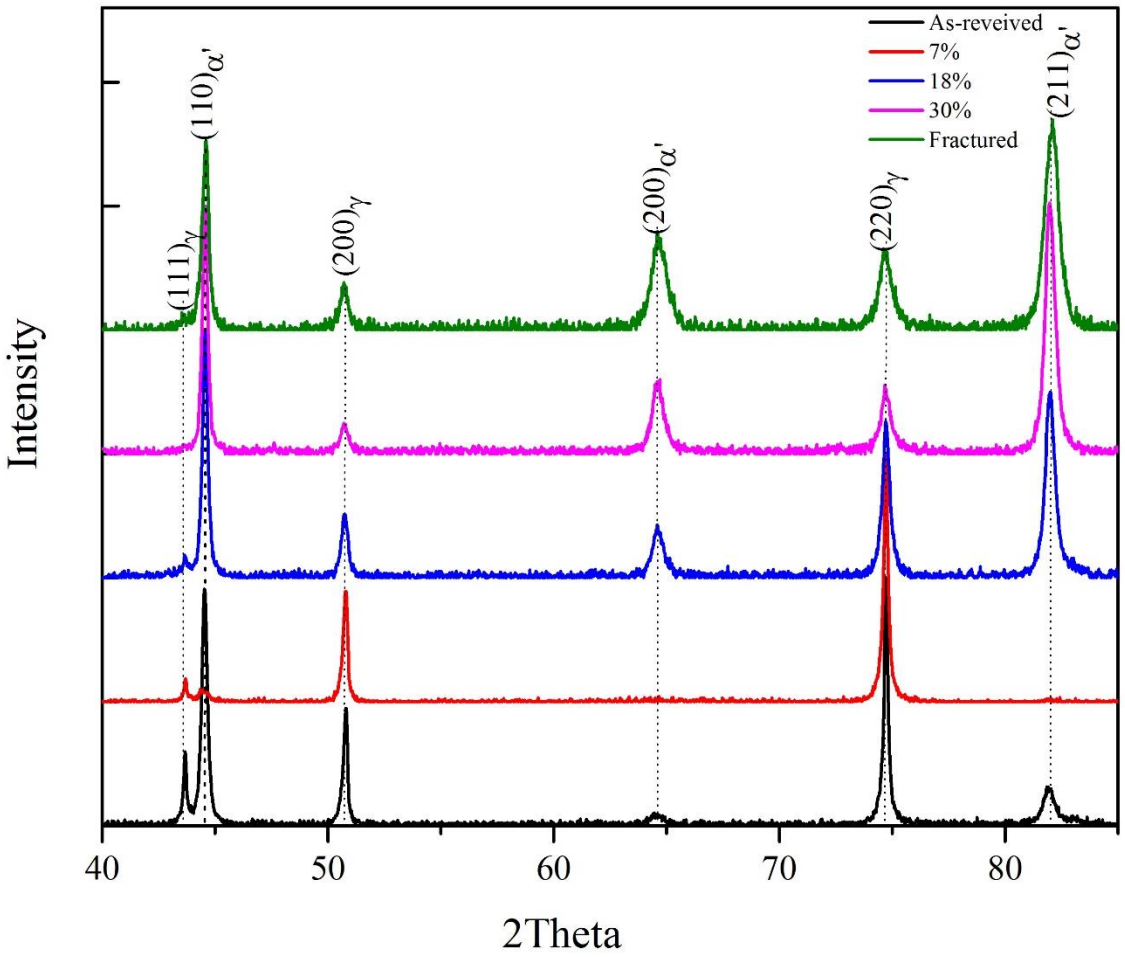

Figure 3.1 X-ray diffraction of 304 sheet samples at different strain level at 25°C

Figure 3.2 shows the x-ray diffraction of 304 sheet sample strained to rupture at different temperatures. From Figure 3.2, we can observe that deformation induced phase transformation is enhanced for lower temperatures (i.e. below 50°C).

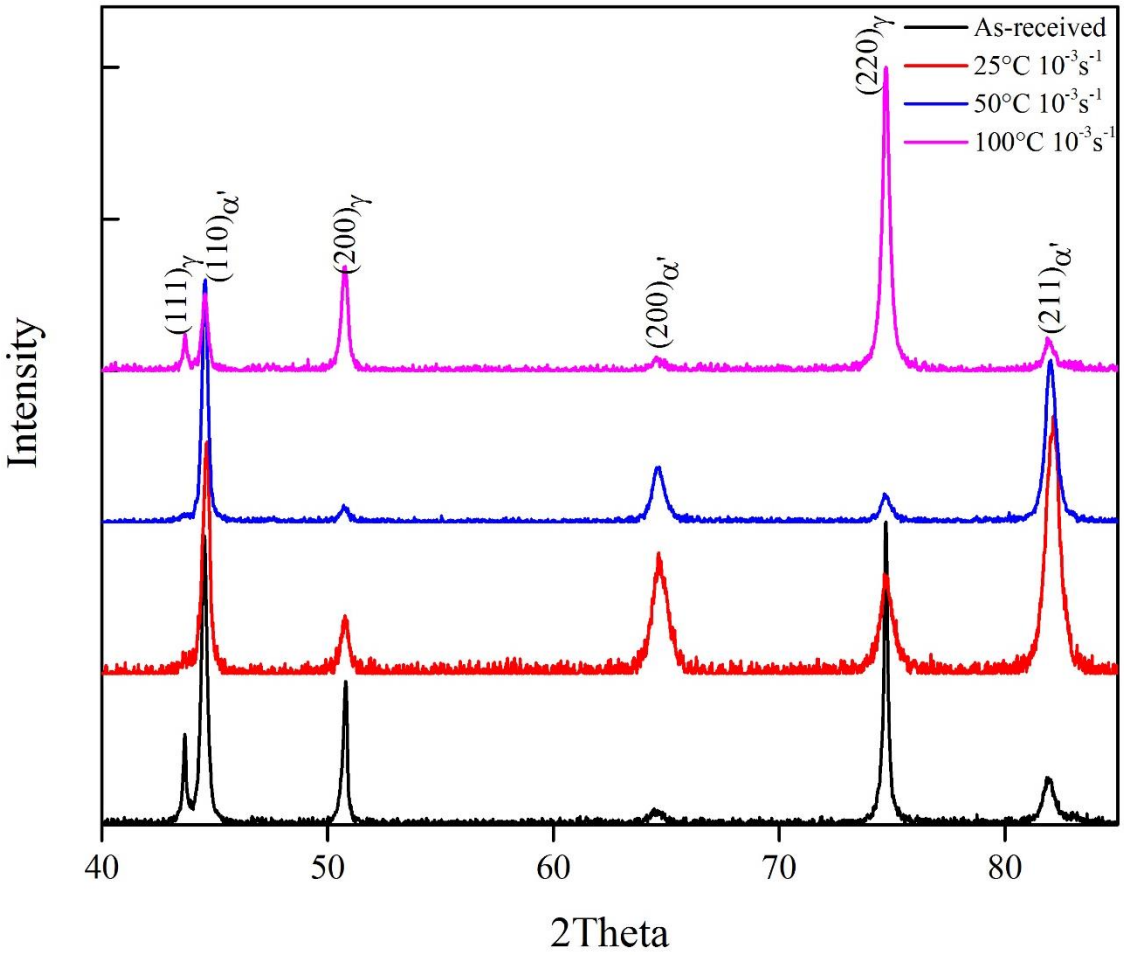

Figure 3.2 X-ray diffraction of 304 sheet sample strained at 25°C, 50°C and 100°C

3.3. Ex-situ TEM Microstructure Examination

3.3.1. 7% Interrupted (304 Sheet Sample, 25°C, $10^{-3}s^{-1}$)

The examination of the samples showed a lot of stacking faults at this strain level. High magnification TEM micrographs of the stacking faults are shown in Figure 3.3 both in bright field and dark field imaging modes.

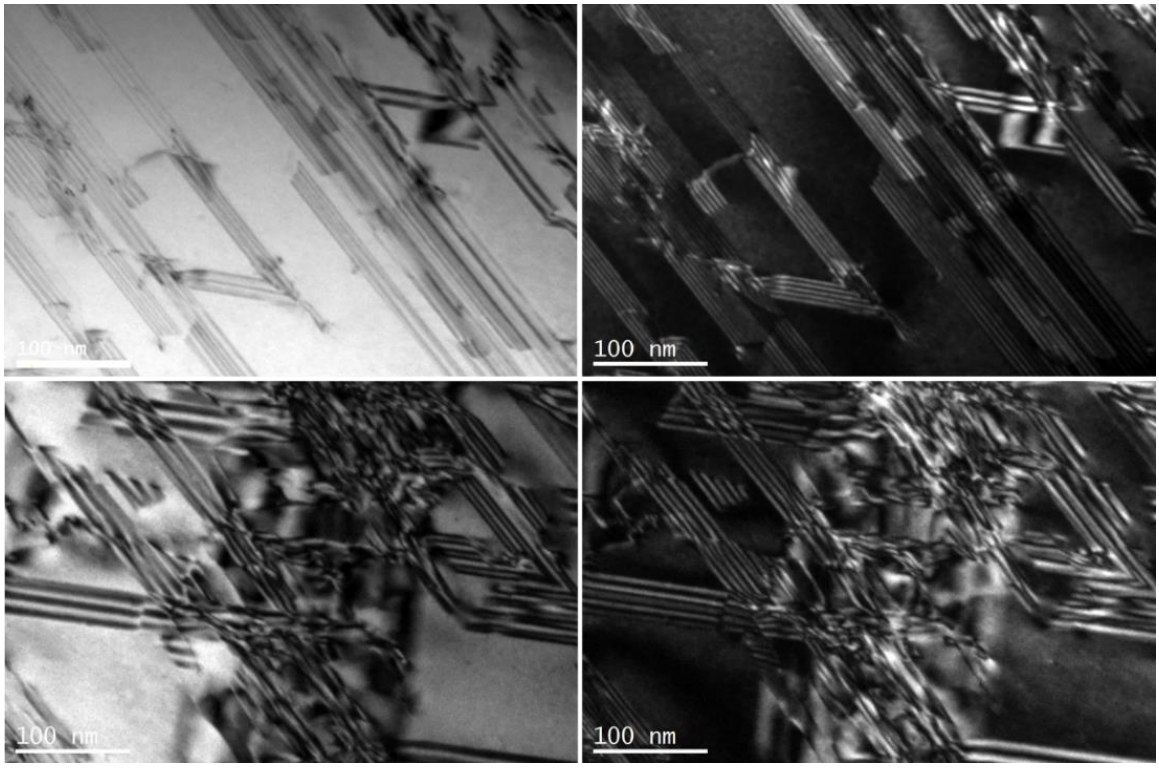

Figure 3.3 Stacking faults formed in 7% strained 304 sheet sample

Shear bands are formed in the 7% strained 304 sheet sample which are shown Figure 3.4 and Figure 3.5. SADs reveal the presence of hcp phase (ε-martensite). Dark field TEM highlights the shear bands to be ε-martensite. The orientation relationship in Figure 3.4 is close to that reported by Zhang[54], which is $[11\text{-}20]_{\varepsilon} \| [110]_{\gamma}$, $(0002)_{\varepsilon} \| (002)_{\gamma}$. The orientation relationship between fcc and bcc in Figure 3.5 is close to the G-T relationship which is $[112]\gamma \sim 2°$ to $[110]\alpha'$, $(011)_{\alpha'} \sim 1°$ to $(111)_{\gamma}$[45].

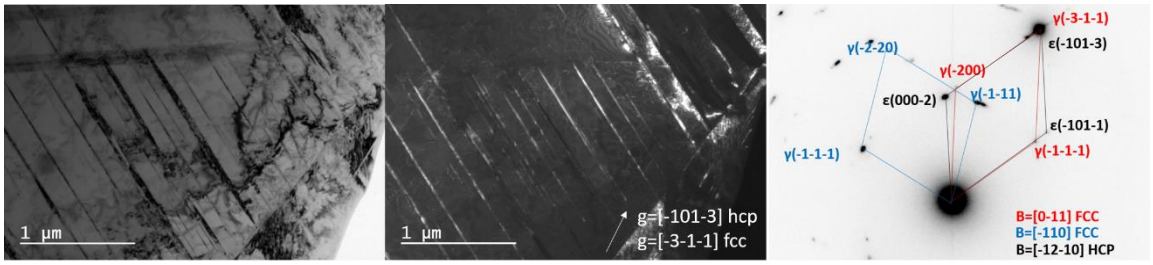

Figure 3.4 Formation of ε-martensite with zone axis of [1-210] in γ-austenite with zone axis of [0-11]

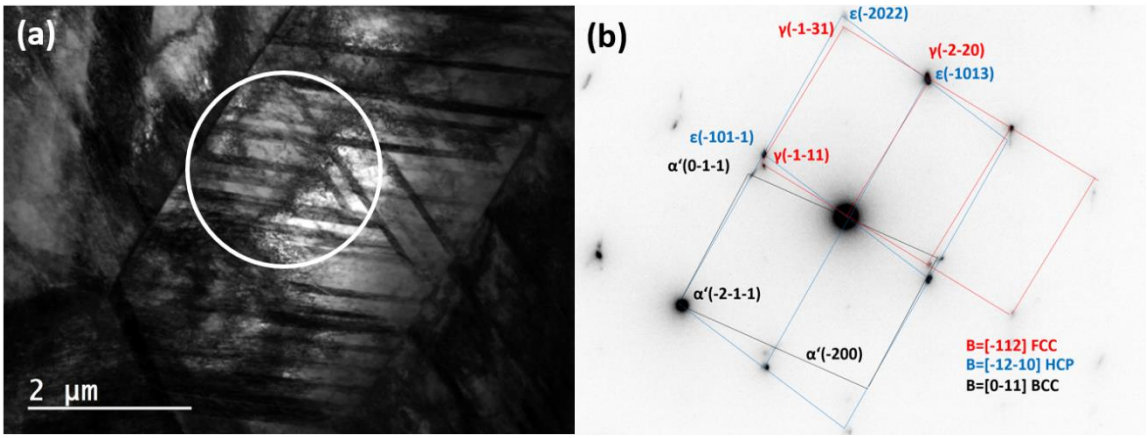

Figure 3.5 Formation of ε-martensite shear bands with zone axis of [-12-10] and α' with zone axis of [0-11] in γ with zone axis of [-112]

The existence of α'-martensite was also found in another area of the same sample, as shown in Figure 3.6 The observed orientation relationship in the diffraction pattern in Figure 3.6 is in accordance with the Nishiyama-Wassermann relation[55], which is usually observed when the bcc phase originates from the direct transformation (fcc phase to bcc phase). However, there is no way to assess for sure whether such martensite is not the pre-existing martensitic phase in the as received material as the observations are done ex-situ and the as-received sheets do have a small fraction of martensite to begin with, as shown by the initial XRD patterns. This reinforces the need for in-situ experiments.

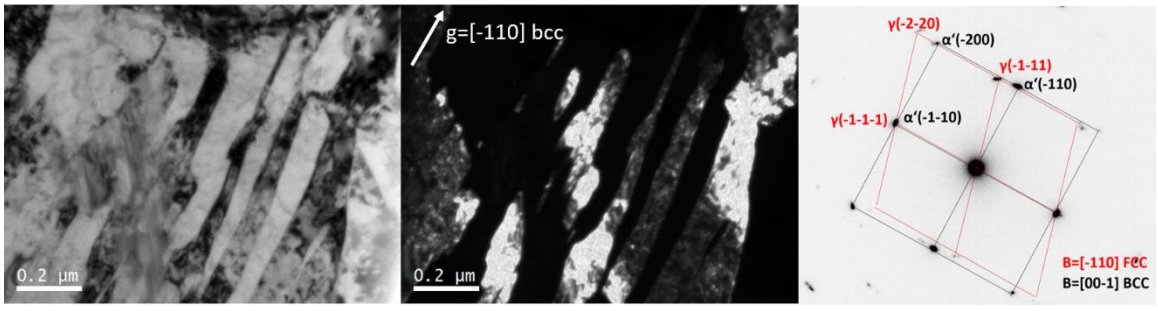

Figure 3.6 Formation of α'-martensite with zone axis of [00-1] in γ-austenite with zone axis of [-110]

3.3.2. 18% Interrupted (304 Sheet Sample, 25°C, $10^{-3}s^{-1}$)

The characterization of the specimen interrupted at 18% also revealed stacking faults and shear bands as shown in Figure 3.7.

The XRD results in Figure 3.1 revealed the presence of α'-martensite at this strain level which was also confirmed by the TEM characterization. SADs taken from three grains are shown in Figure 3.7. Bright field TEM micrograph from the first grain indicated the existence of shear bands. Corresponding SAD indicates the crystal structures to be FCC and HCP. Mechanical twinning can also be characterized from the SAD. And the dark field TEM highlights the shear bands and γ-austenite matrix. SAD taken from the second grain indicates the only crystal structure to be FCC. Both shear bands and lathlike martensite can be observed in the third grain. Corresponding SAD reveals the crystal structures in the third grain to be FCC, BCC and HCP. The dark field TEM highlights the existence of γ-austenite matrix, ε-martensite and α'-martensite bands. OR in the first area is close to the S-N relationship, which is $[11\text{-}20]_{\varepsilon} \| [1\text{-}10]_{\gamma}$, $(0002)_{\varepsilon} \| (111)_{\gamma}$.

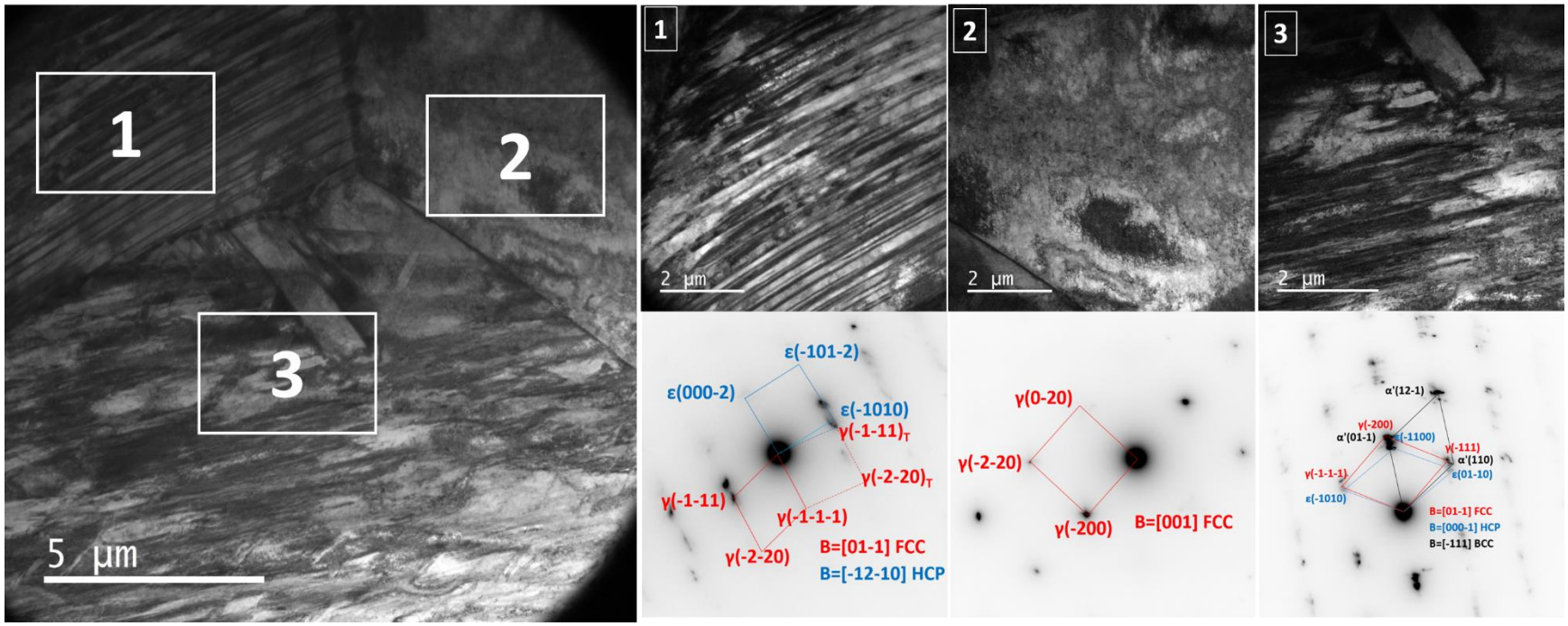

Figure 3.7 ε-martensite and α'-martensite formed in γ-austenite matrix in 18% strained 304SS specimen

3.3.3. 30% Interrupted (304 Sheet Sample, 25°C, $10^{-3}s^{-1}$)

TEM characterization of the 30% strained-interrupted specimen is shown in Figure 3.8. Lathlike martensite can be observed in the 1st, 3rd and 4th areas. SAD corresponding to the 1st area indicates the presence of FCC and BCC crystal structure i.e. α'-martensite phase in γ-austenite matrix. Shear bands are visible in the BF image of the 2nd area and the SAD reveals the existence of ε-martensite and γ-austenite matrix. The bright field TEM pictures of the 3rd area is similar to that of the 1st area with lathlike martensite. The corresponding SAD reveals the existence of ε-martensite, α'-martensite and γ-austenite matrix. The SAD taken from the 4th area also indicates the formation of α'-martensite in γ-austenite matrix. However, the shape of martensite in the 4th grain is different from that in the 1st and 3rd area, which may be due to a different orientation of α'-martensite from that in the other areas. The austenitic grain size may also play a role on the difference of α'-martensite shape in these grains. OR in the first area is close to the S-N relationship, which is $[11\text{-}20]_{\varepsilon} \| [1\text{-}10]_{\gamma}$, $(0002)_{\varepsilon} \| (111)_{\gamma}$.

Different from the observation in the 7% and 18% strained samples, in the 30% strained samples, less stacking faults are observed and α'-martensite is more readily found in the TEM examination.

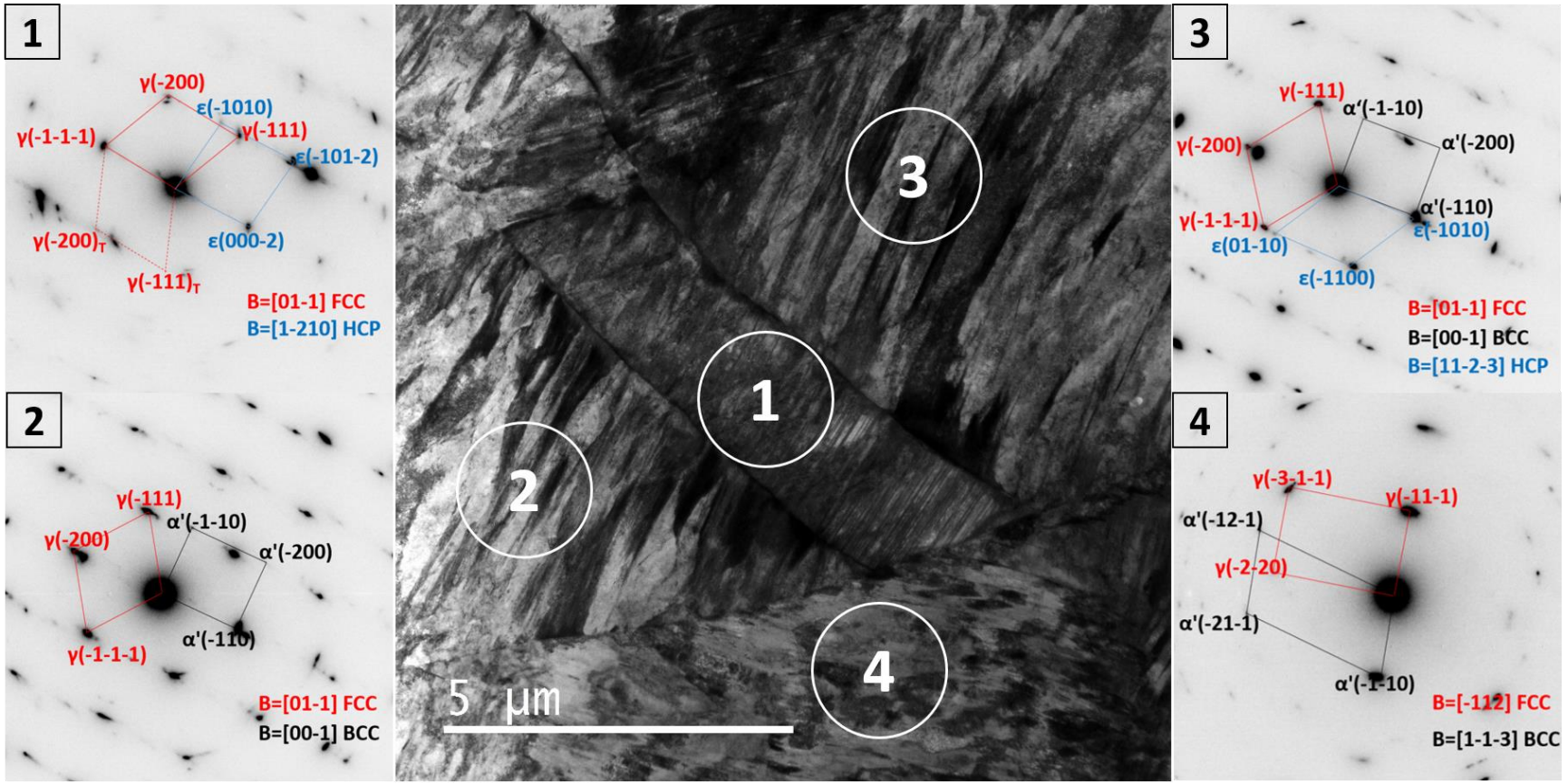

Figure 3.8 ε-martensite and α'-martensite formed in γ-austenite matrix in 30% strained 304SS specimen

3.3.4. Fractured (304 Sheet Sample, 25°C, $10^{-3}s^{-1}$)

Martensite phase can be observed in the fractured samples which are shown in Figure 3.9, Figure 3.10. OR in Figure 3.9 goes well with K-S and N-W relationship which is $[-101]_{\gamma} \| [-1-11]_{\alpha'}$, $(111)_{\gamma} \| (011)_{\alpha'}$ and $[-101]_{\gamma} \| [001]_{\alpha'}$, $(111)_{\gamma} \| (011)_{\alpha'}$.

Similarly to the 30% strained sample, stacking faults were not readily observed at this strain level, but martensitic phase could be found more easily. HCP phase (ε-martensite) is also found as shown in Figure 3.10.

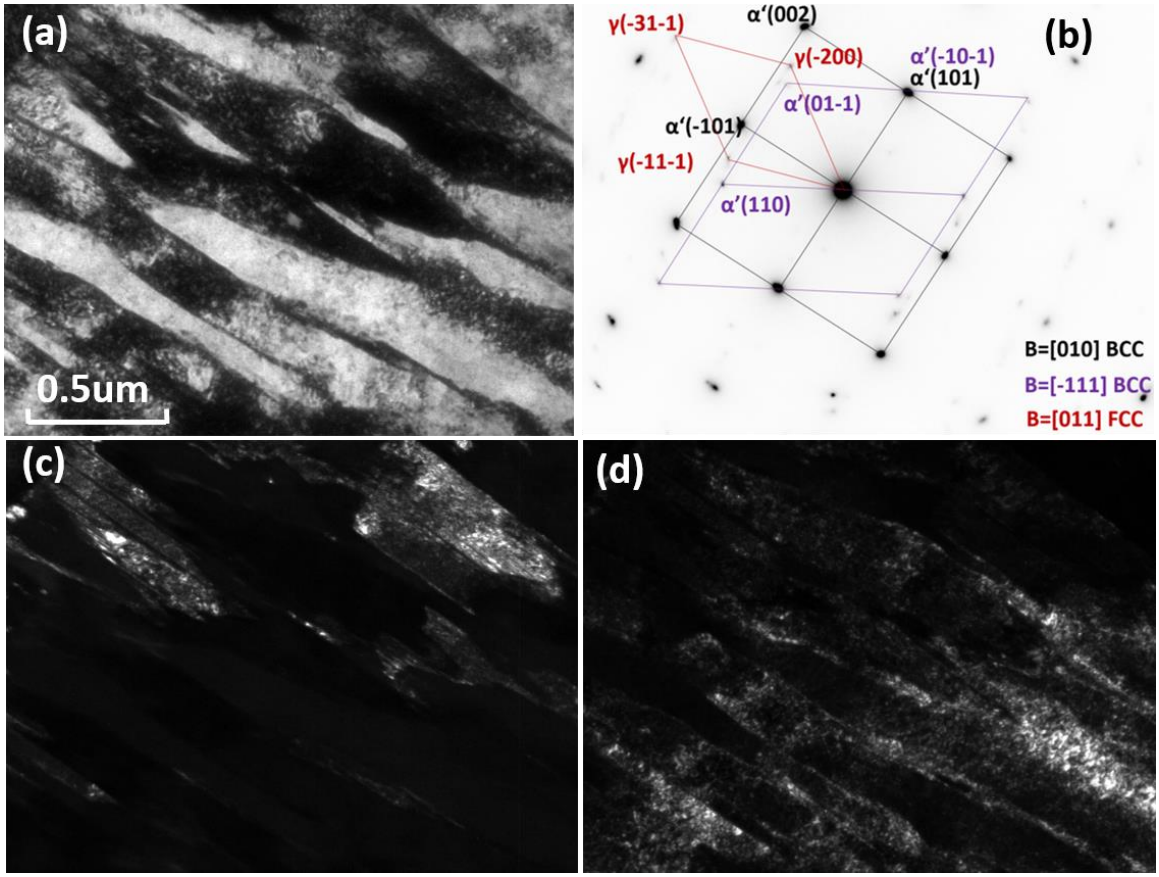

Figure 3.9 Formation of and α'-martensite with zone axis of [010] and [-111] in γ-austenite with zone axis of [011]

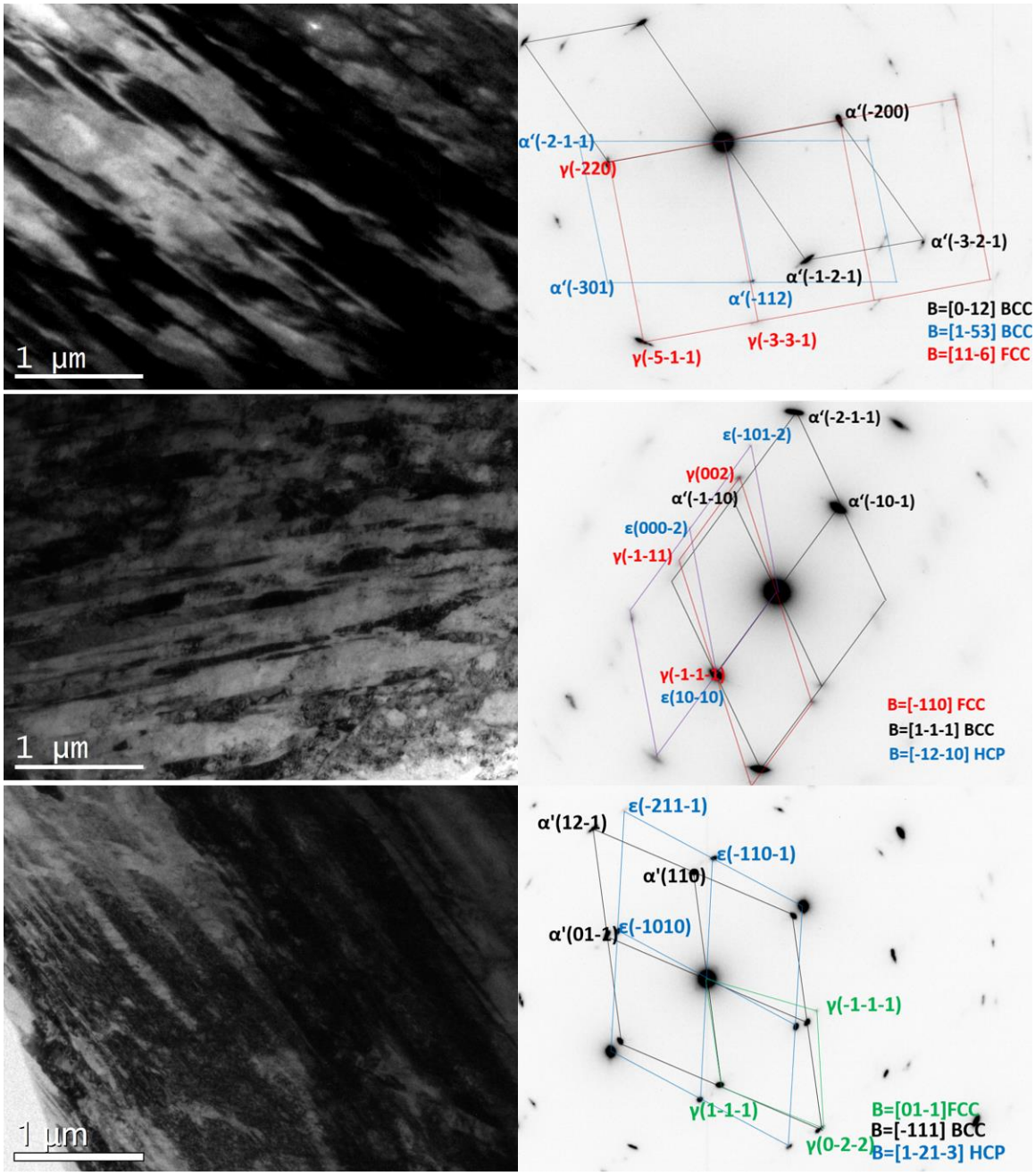

Figure 3.10 Formation of ε-martensite shear bands and α'-martensitein in fractured 304 sheet sample

3.3.5. Summary of Ex-situ TEM Examination

Stacking faults are more favored to be observed at lower strain level (as-received state, 7% and 18% strained). Mechanical twinning is observed only at the intermediate strain level (18% and 30%) and α'-martensite is more readily found at higher straining

level (30% and fractured). At high straining level, stacking faults are not easy to distinguish anymore. One reason is that with further straining, stacking faults are tangled together and transform into shear bands and further transformed into ε-martensite. Another reason may be the local temperature rise resulting from the adiabatic heating, which leads to an increase in the SFE and make it hard to form new stacking faults.

De[35] reported by XRD characterization that the ε-martensite is formed in the range up to 15% engineering strain, after that the content of ε-martensite will decrease due to the further transformation into α'-martensite. Similar results are also confirmed by the TEM examination of interrupted tensile tests, which in the 7, 18% strained sample, ε-martensite bands are more easily to be observed than that in the fractured sample.

As introduced in the first chapter, possible martensitic nucleation sites like shear-band intersections parallel shear-bands, twin boundary are observed in the ex-situ TEM examination in accordance with literature[23, 38, 56].

Meanwhile, orientation relationships like N-W, K-S, G-T and S-N are confirmed.

Although the ex-situ examination allowed to reveal the influence of the strain level on the microstructure, particularly the presence of SFs, ε-martensite shear bands and α'-martensite, and orientation relationships between the phases, there lacks in-situ observation to determine the mechanism by which the microstructure evolves. Henceforward, in-situ tests were done as described in Chapter 2.

3.4. In-Situ TEM Tensile Tests at 25°C

3.4.1. Evolution of Stacking Faults and Formation of ε-martensite

The process of stacking faults evolution and formation of ε-martensite is recorded during the in-situ experiments.

Steps of stacking faults changes were recorded in 304L bar sample during the in-situ tensile tests which are shown in Figure 3.11, Figure 3.12 and Figure 3.14.

The rectangle in Figure 3.11 indicates the formation and changes of stacking faults in 304L bar sample at different straining level. The white rectangle marks the area where stacking faults were formed and changed. In the initial stage (pulling distance <163um), stacking faults cannot be observed in that area. When the pulling distance was 325um, some stacking faults nucleated nearby the grain boundary and began to grow inside the austenitic grain. When the pulling distance was 396um, due to the formation of more stacking faults, overlapping can be observed. And when the pulling distance is 452um, bundles of stacking faults seems to be formed in that area.

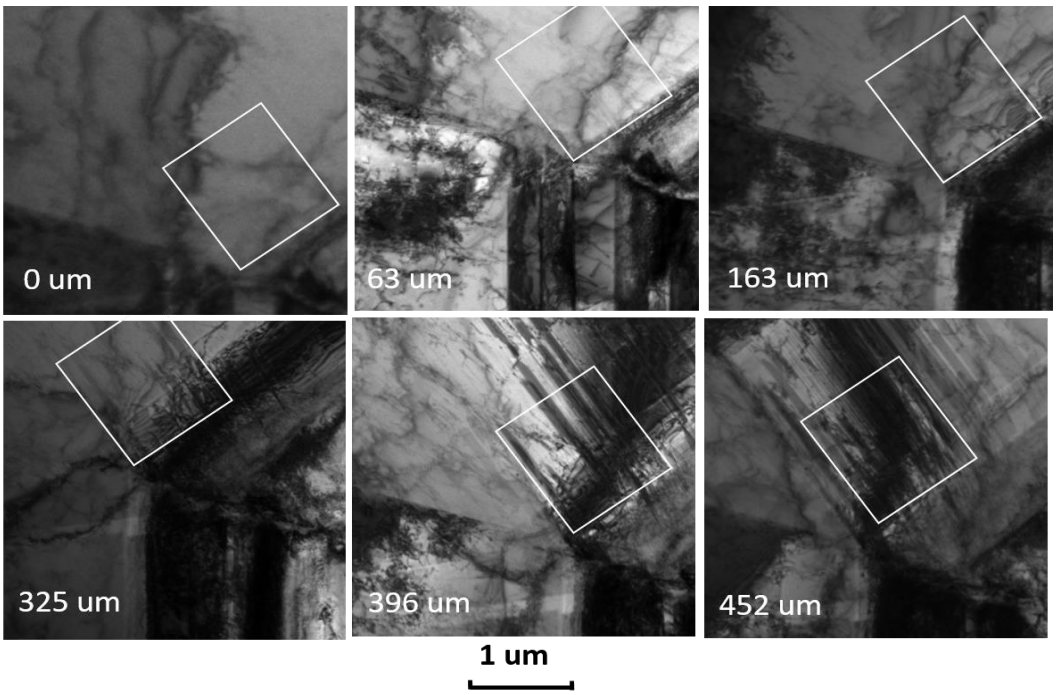

Figure 3.11 Steps of formation of stacking faults and α'-martensite in 304L (sample 5)

Stacking faults can serve as an intermediate step for the transformation from γ to ε. ε-martensite nucleates in the area with overlapping and tangling stacking faults, which is further confirmed by other in-situ TEM characterizations.

More formation and evolution of stacking faults in 304L bar sample are shown in Figure 3.12. The steps of stacking faults formation and evolution are similar to that shown in Figure 3.11. New stacking faults marked by the dash arrow seem to firstly nucleate at the grain boundary and then extend into the austenite grain. Width of stacking fault bundle is changed due to the formation of new stacking faults which is marked by the solid arrow and the dash rectangle. Meanwhile, some new stacking faults can form when the previous ones extended so that overlapping and tangling can occur.

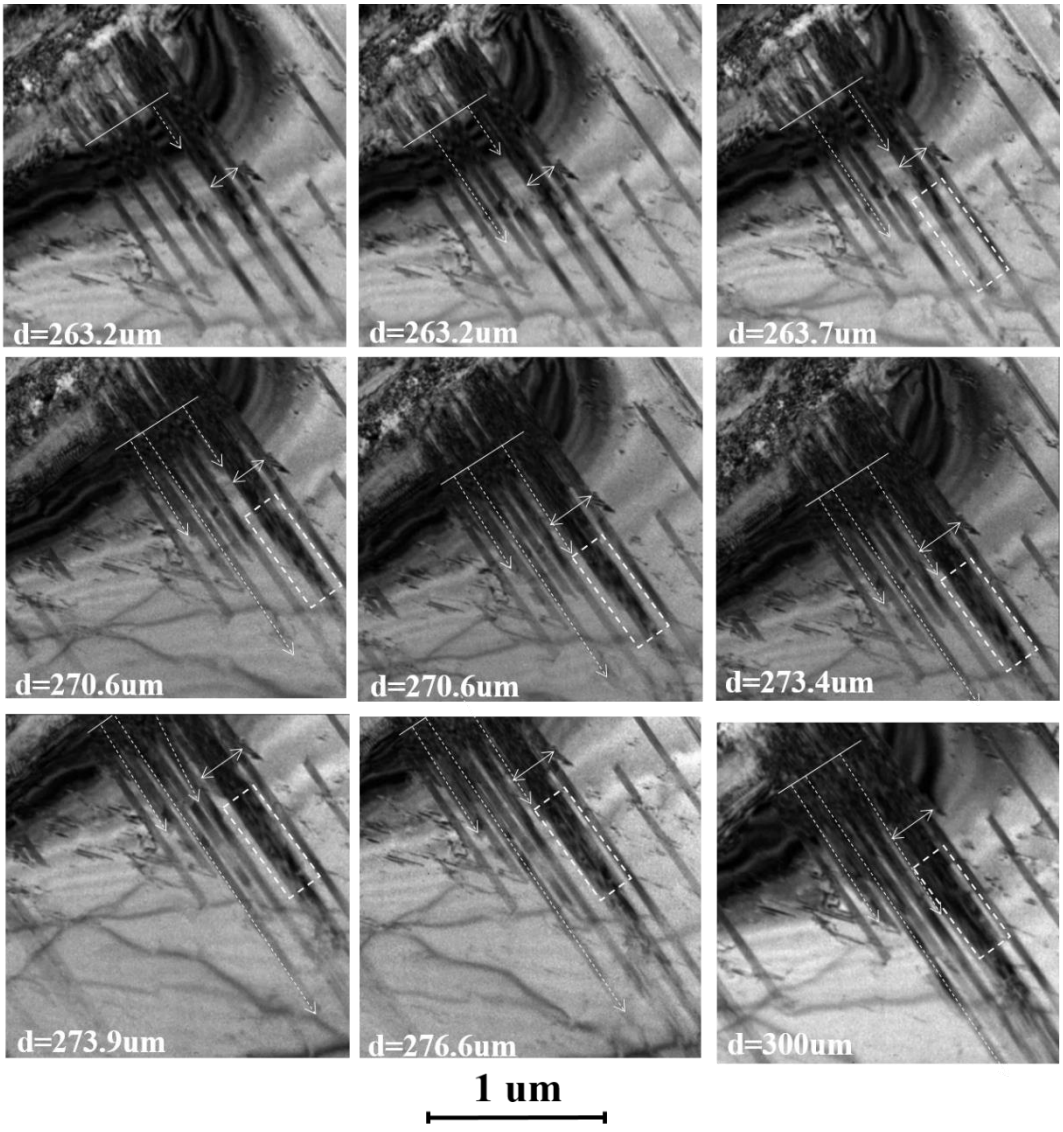

Figure 3.12 Steps of changes of stacking faults in 304L bar (sample 5)

When the pulling distance is 325um, the area is highly deformed and stacking fault "bundling" can be observed. One SAD was taken from this area which is shown in Figure 3.13. Analysis of SAD indicates the crystal structures to be fcc and hcp, which means the formation of ε-martensite phase in γ-austenite matrix.

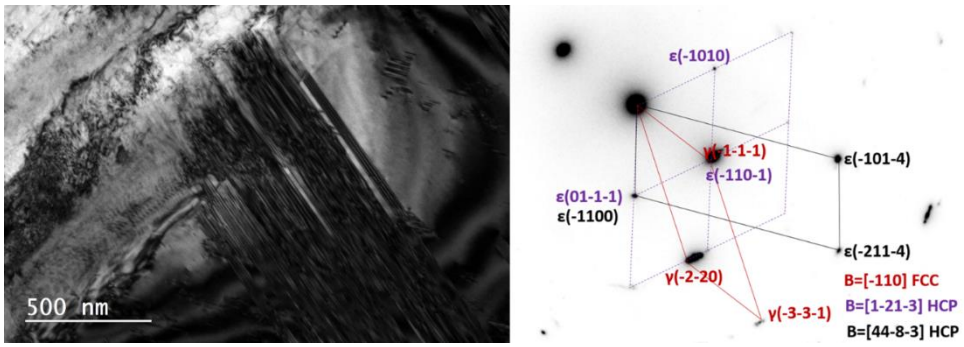

Figure 3.13 Formation of ε-martensite shear bands with zone axis of [1-21-3] and [44-83] in γ-austenite with zone axis of [-110] in 304L bar (sample 5)

Similar stacking faults evolution phenomenon was also recorded in another 304L bar sample shown in Figure 3.14. One austenite grain was followed, stacking faults were recorded to originate from grain boundaries and grow across the grain. With increasing straining, more stacking faults are formed and some began to intersect and overlap with each other, which can be seen when the pulling distance was 325.1um.

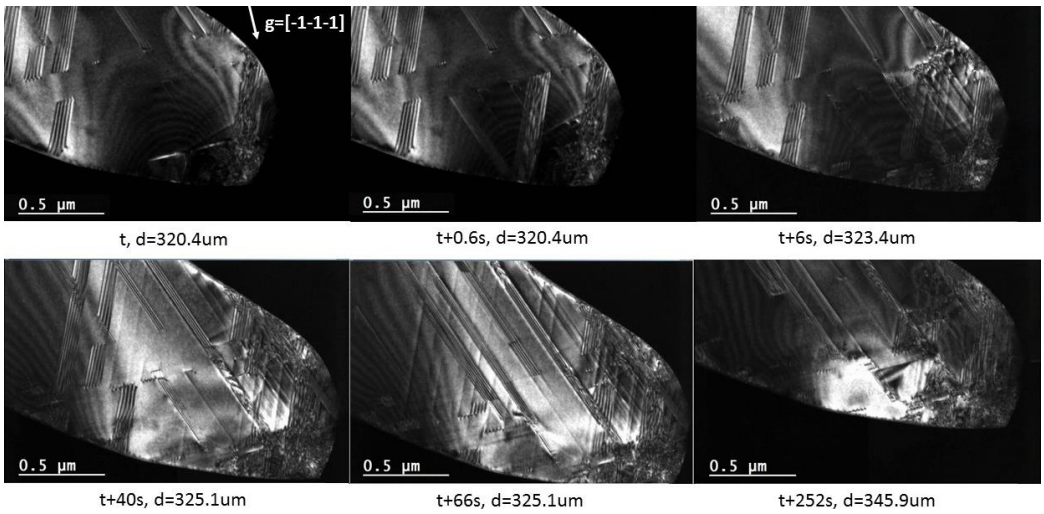

Figure 3.14 Steps of changes of stacking faults in 304L bar (sample 3)

When some stacking faults overlap together, the micro "shear band" may be observed, which can be seen in Figure 3.15. As for the definition of "shear band", it can be either ε-martensite, twinning austenite, faulted austenite or faulted ε martensite.

The formation process of such shear bands was recorded and shown in Figure 3.15. Similarly, stacking faults seemed to firstly form across the grain. With further straining, stacking faults were mainly tangled into bands instead which can be seen in the dash rectangle when the pulling distance was 327um. After the pulling distance reaches 427um, the area was highly deformed. SAD and high magnification TEM micrographs using both bright field and dark field modes were taken from the area that marked by the white circle, which are shown in Figure 3.16. Analysis of SAD confirms the formation of ε-martensite in γ-austenite matrix with the orientation relationship $[1\text{-}1\text{-}2]_{fcc} \parallel [000\text{-}1]_{hcp}$, $(\text{-}11\text{-}1)_{fcc} \parallel (\text{-}1010)_{hcp}$.

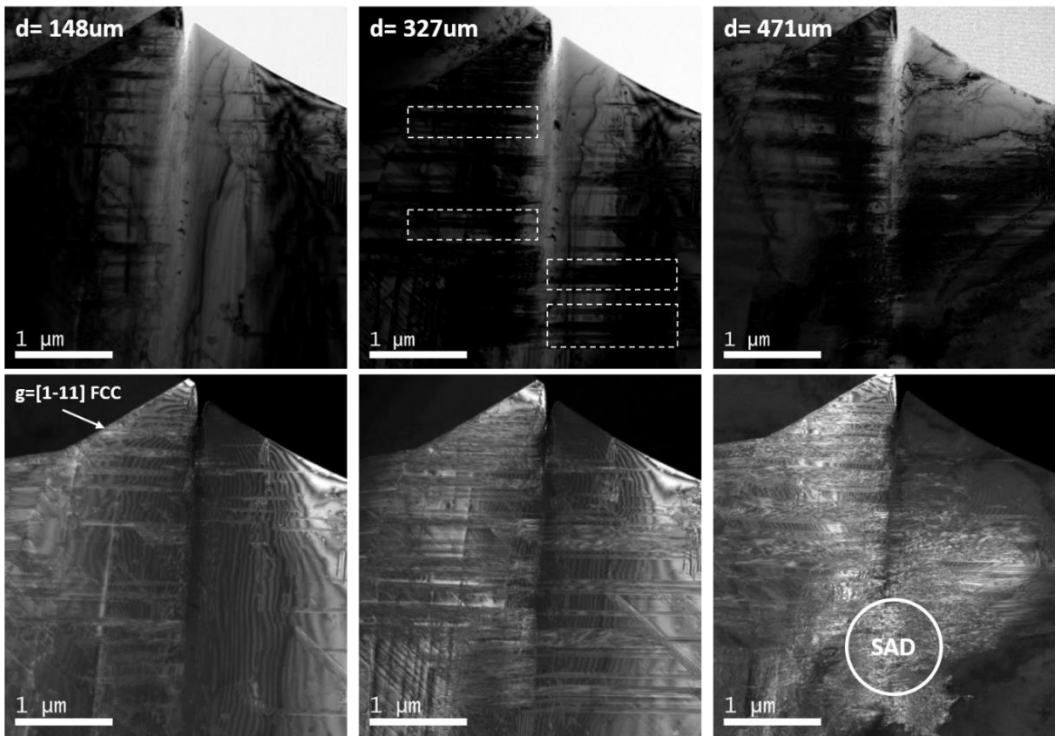

Figure 3.15 Shear bands evolution and formation of ε-martensite in 304L bar (sample 6)

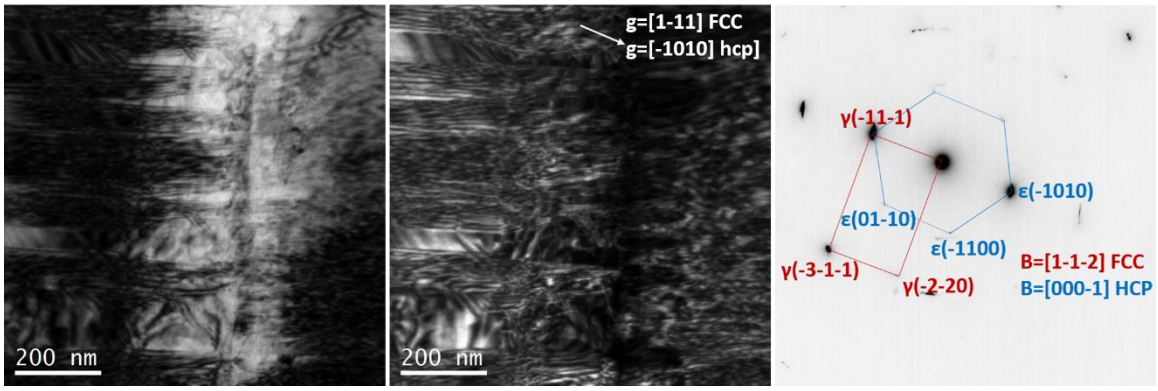

Figure 3.16 Formation of ε-martensite with zone axis of [000-1] in γ-austenite with zone axis of [1-1-2] in 304L bar (sample 6)

In this part, formation and evolution of stacking faults were evidenced by the in-situ in the TEM. Shear bands formed by overlapping and tangling stacking faults can serve as the intermediate/nucleation sites for ε-martensite.

3.4.2. Twinning as the intermediate

When the stacking faults overlap on successive $(111)_\gamma$ plane, it can produce a mechanical twin, which is also one kind of morphologies of shear bands[50]. Mechanical twinning is reported to be favored when the stacking fault energy is in a range of 18-45mJ/m^2[9]. In our case, the stacking faults energy is below but not far from 18 mJ/m^2 so that mechanical twinning may also occur. As discussed in the first chapter, twinning boundary can serve as the nucleation sites for martensite. The morphology of mechanical twin in 304 stainless steels has been reported by Luo[57] and Shen[24]. Similar mechanical twins are also observed in our in-situ experiments, which are shown in Figure 3.17 and Figure 3.18.

Mechanical twinning in 304L bar sample was observed when the pulling distance was 389.2um in Figure 3.17(a). Another bright field TEM image was taken when the pulling distance was 693.8um to see the changes of mechanical twinning, which is shown

in Figure 3.17(b). From the bright filed TEM in Figure 3.17(b), stacking faults fringes were observed to be formed between twinning boundaries.

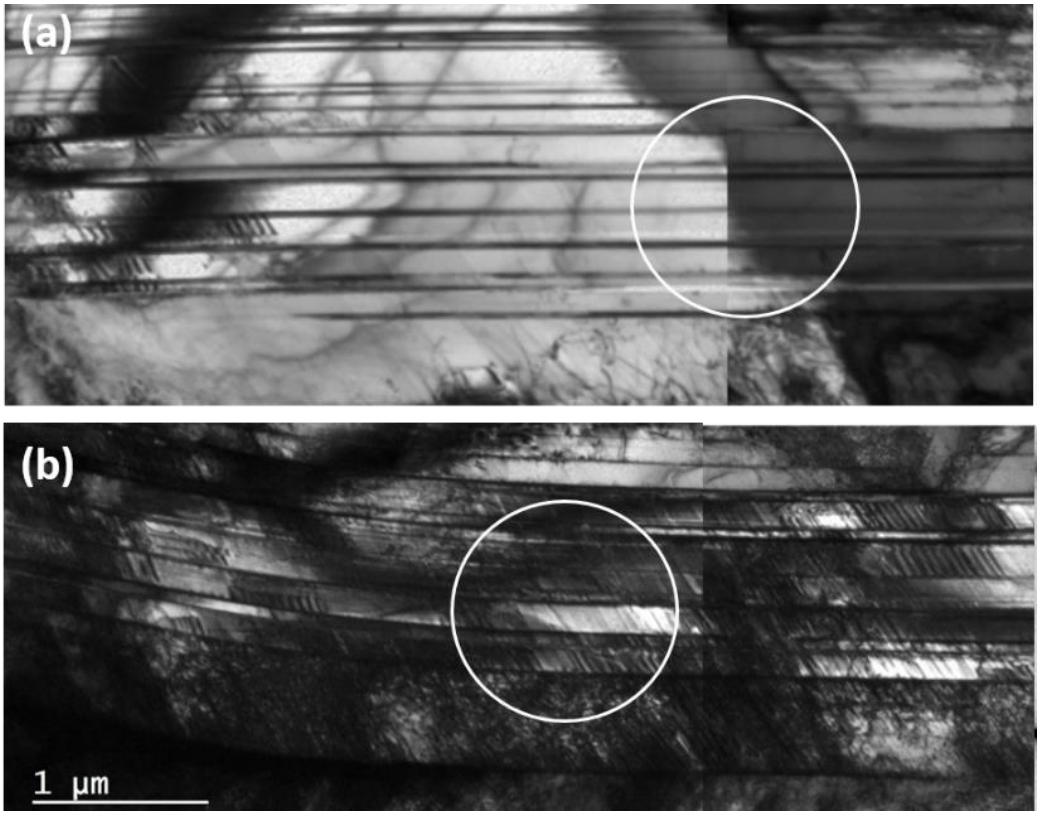

Figure 3.17 BF TEM images of same region at different pulling distance (a) 389.2um (b) 693.8um in 304L bar (sample 1)

Another two bright field TEM and corresponding SADs of the same area in 304L bar sample were taken at different strain levels and shown in Figure 3.18. Figure 3.18(a) shows presence of ε-martensite with zone axis [01-1-1] and γ-austenite matrix with zone axis [0-11]. Mechanical twinning can be confirmed from the SAD. Figure 3.18(b) shows presence of α'-martensite with zone axis [011] and γ-austenite matrix with zone axis [0-1-1] with twins. By comparison of (a) and (b) in Figure 3.18, we can conclude that ε can be further transformed into α' and twinning boundary may serve as the nucleation sites for α'-martensite.

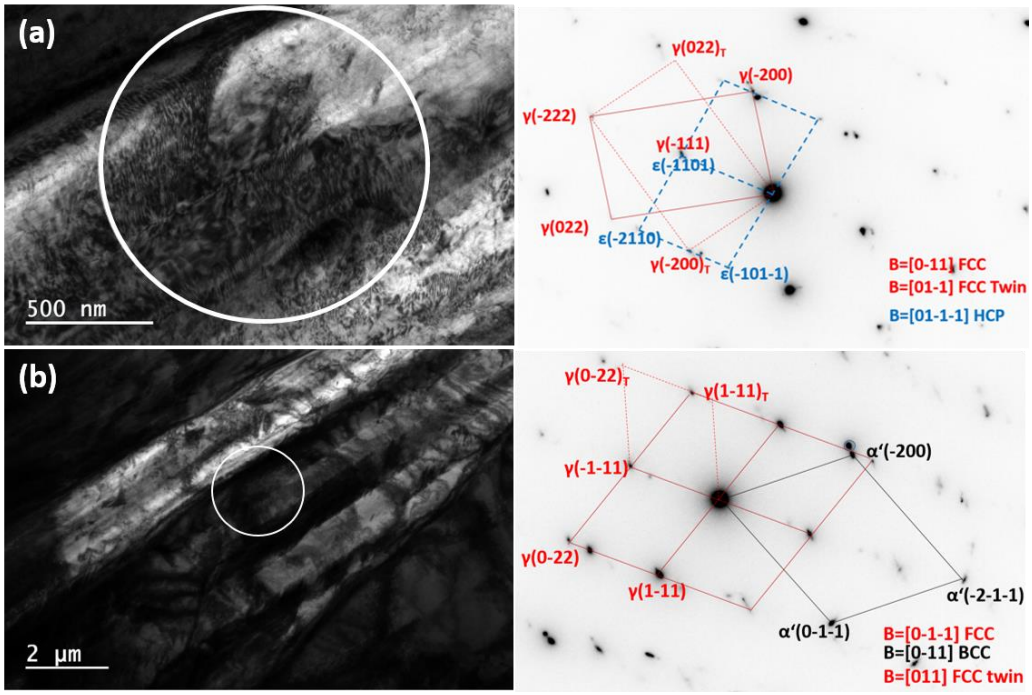

Figure 3.18 Formation of α'-martensite with zone axis of [0-11] following the formation of ε-martensite with zone axis of [01-1-1] in γ-austenite with zone axis of [0-11] in 304L bar sample (a) 131um (b) 161um (sample 4)

Twinning can play a role in the martensitic transformation. Mechanical twins can provide more nucleation sites for martensite. However, based on the TEM characterization, mechanical twinning has less possibility to be formed in 304 and 304L compared with the formation of stacking faults, which is due to the low SFE of 304 type steels as explained before.

3.4.3. Direct Transformation (with the assistance of ε bands)

ε-martensite bands are firstly formed. Then, α'-martensite will nucleate between ε-martensite and γ-austenite and grow into the γ-austenite. This theory was proposed by Nishiyama[44], which is confirmed by in-situ TEM characterization.

Migration of interface is highlighted by the white arrows in Figure 3.20. Corresponding SAD taken before straining is shown in Figure 3.19. The matrix of γ-austenite and ε-martensite shear bands are highlighted in the dark field imaging mode in

Figure 3.19. When the pulling distance reaches 452um, another SAD shown in Figure 3.21 is taken and confirms the formation of α'-martensite. It can be concluded that shear bands may be pre-existing in the austenitic matrix and with further straining, α' can nucleate between shear bands and the austenitic grain and grow into the austenitic grain.

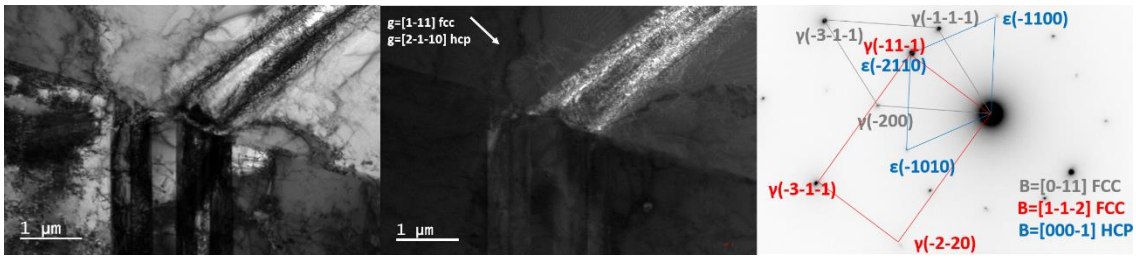

Figure 3.19 Formation of ε-martensite with zone axis of [000-1] in γ with zone axis of [0-11] and [1-1-2] in 304L bar (sample 5)

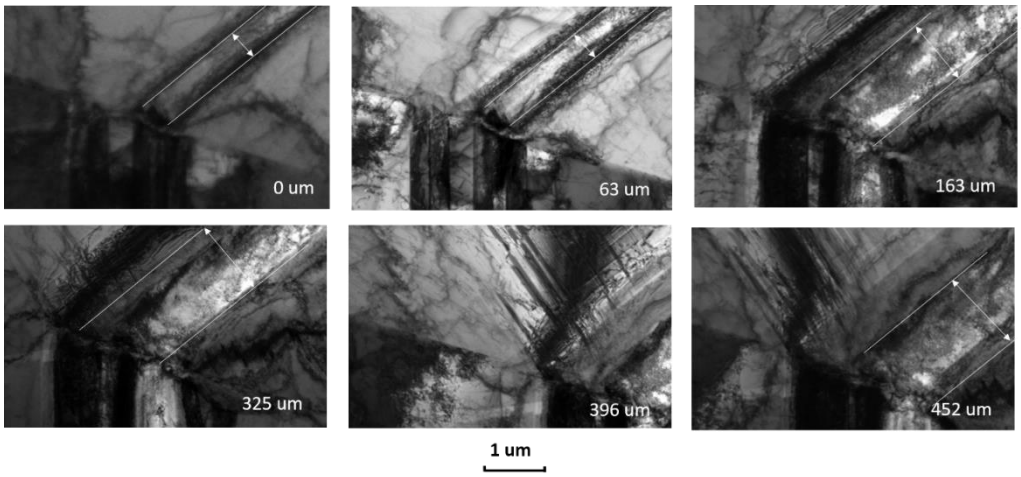

Figure 3.20 Steps of formation and growth of α'-martensite in 304L bar (sample 5)

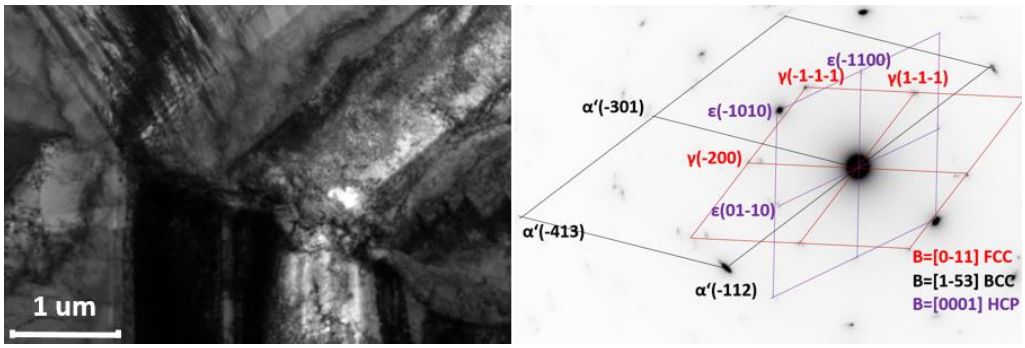

Figure 3.21Bright field TEM of the area followed showing the formation of α'-martensite in 304L bar (sample 5)

Similar transformation mechanism, formation of α' between ε plates is confirmed in Figure 3.22. Growth of new crystal is determined by bright field and dark field TEM micrograph that taken at different pulling distance, which are shown in Figure 3.22. The SAD in Figure 3.23 can reveal the crystal structure of the new phase to be α'-martensite. Dark field TEM micrograph in Figure 3.24 and SAD 2 in Figure 3.23 confirm the existence of ε-martensite.

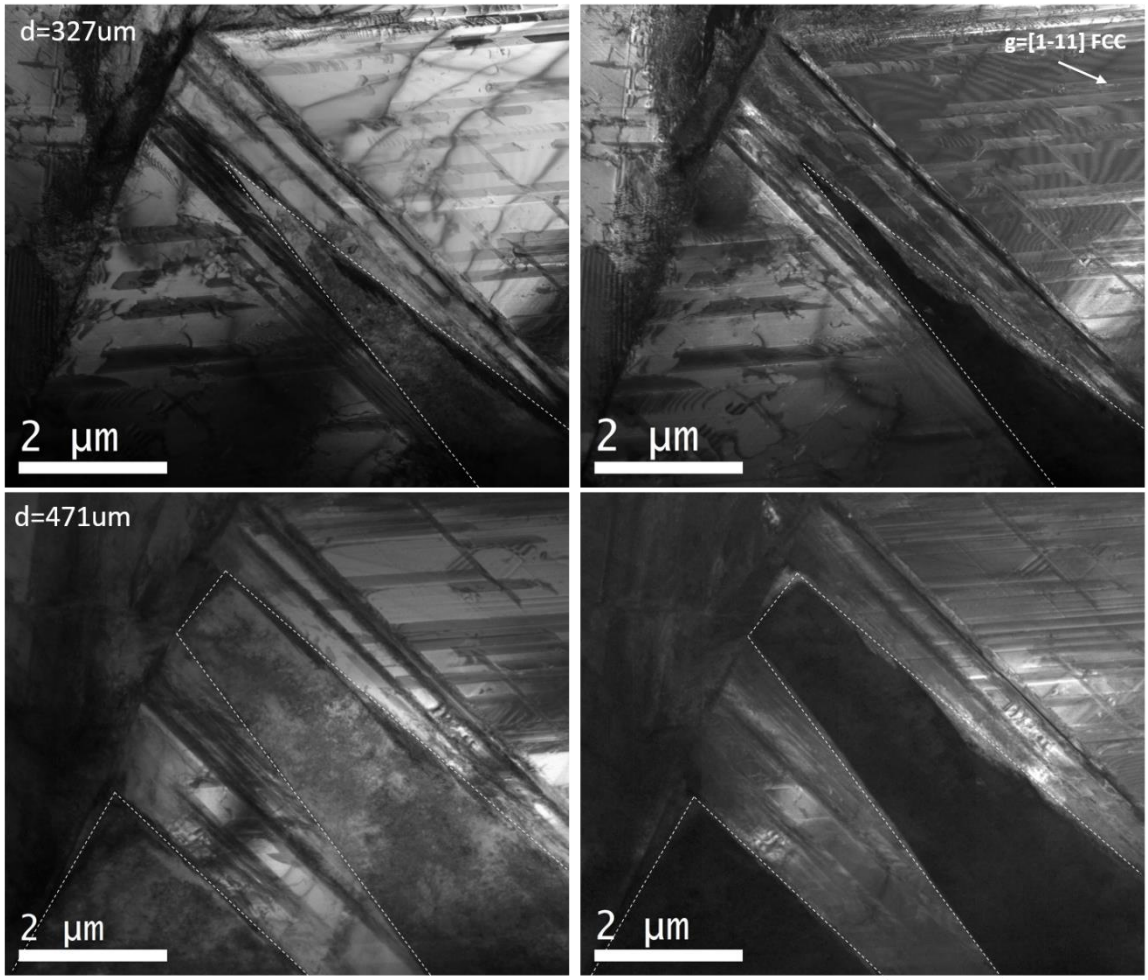

Figure 3.22 Growth of α' and εmartensite in γ-austenite in 304L bar (sample 6)

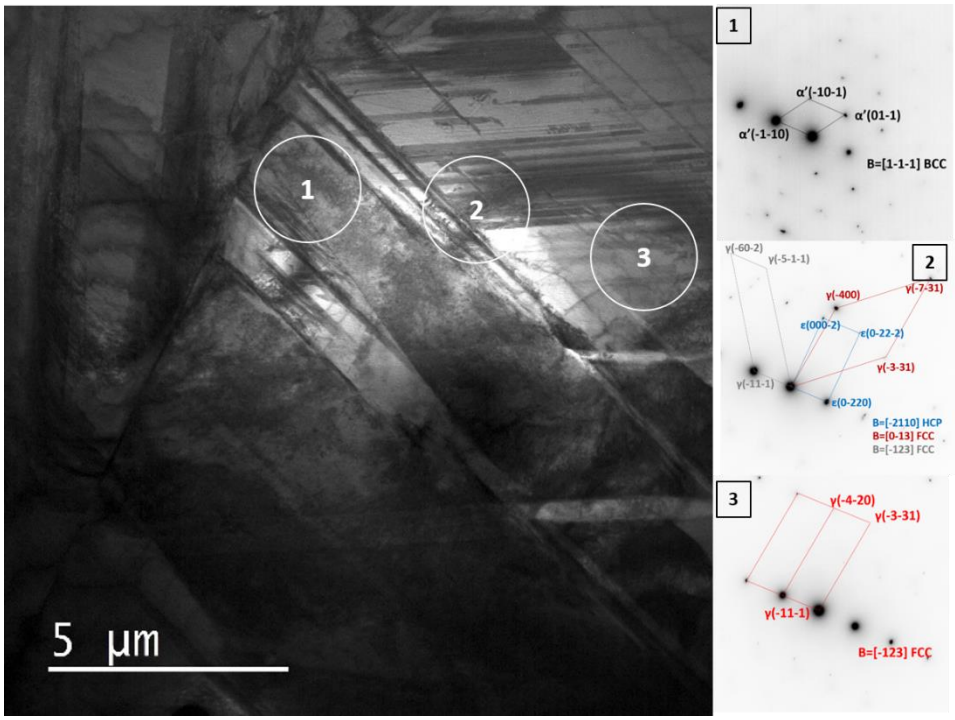

Figure 3.23 BF taken at pulling distance equal to 471um and SAD from different area revealing the crystal structure of the new phase in 304L bar (sample 6)

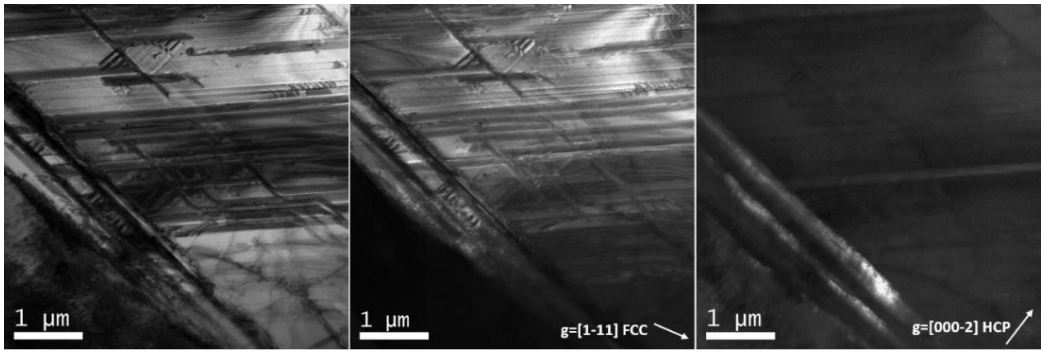

Figure 3.24 BF and DF TEM showing the matrix and ε-martensite in 304L bar (sample 6)

Formation of α' between ε plates and γ matrix is noticed in Figure 3.25 and Figure 3.26. The shear bands (marked by the dash arrow) are firstly formed in the matrix when the pulling distance is 148um. And α'-martensite (marked by the solid arrow) is formed between the shear bands and the matrix when the pulling distance is 327um. With further straining, α'-martensite continues growing. When the pulling distance is 471um, SADs in Figure 3.26 are taken from the newly formed and previous phases, which prove the

formation of α' and the existence of ε martensite bands in γ-austenite matrix. In addition, it could be observed that during the transformation, the ε-martensite bands are serving as the boundary between γ and α'.

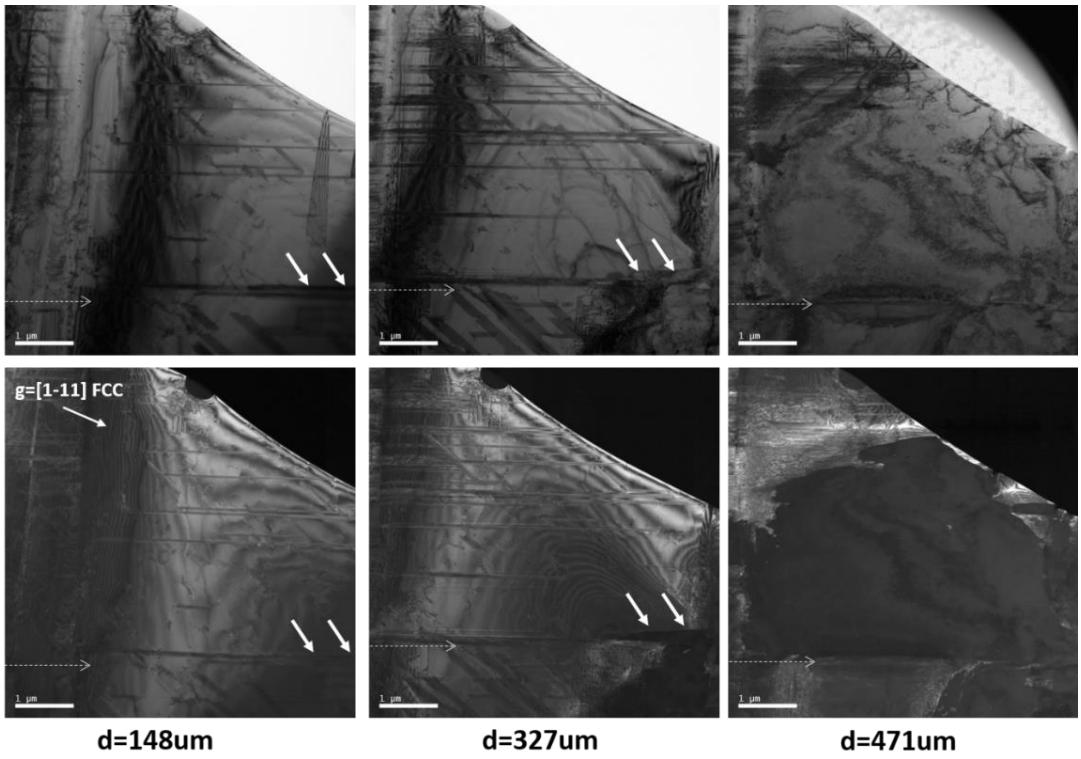

Figure 3.25 Changes of microstructure at different strain levels in 304L bar (sample 6)

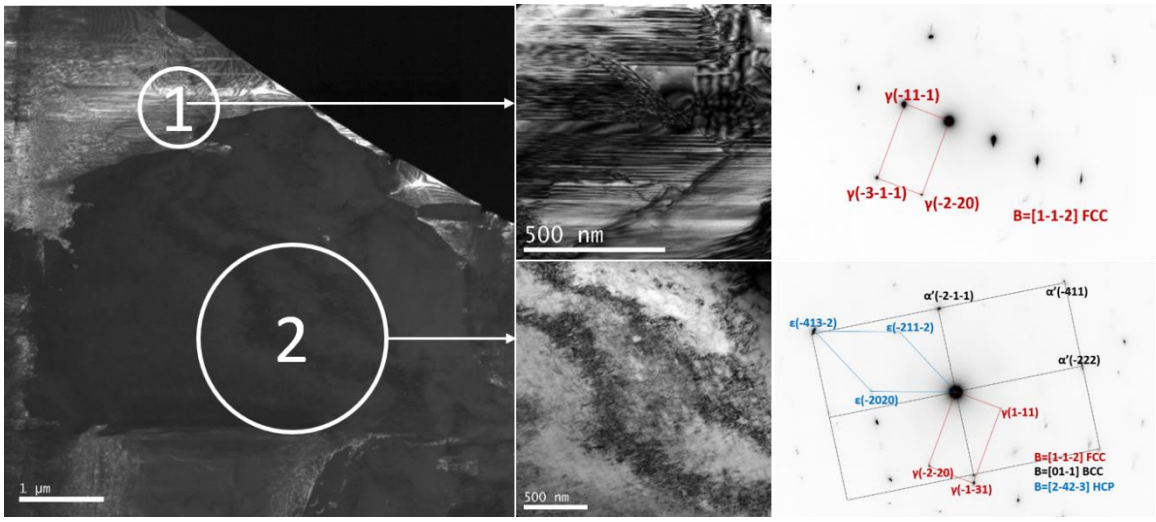

Figure 3.26 SADs revealing α' with zone axis of [01-1] and εwith zone axis of [2-42-3] and the matrix to be fcc with zone axis of [1-12] in 304L bar (sample 6)

3.4.4. Direct Transformation (without the assistance of ε bands)

α'-martensite appears to nucleate at the grain boundary, and with further straining, the interface between α'-martensite and γ-austenite migrates into the γ-austenite as the γ-austenite is transformed into α'-martensite. Meanwhile, dislocations are formed nearby the interface to relieve the internal stress. Details of this kind of transformation are shown in Figure 3.27, Figure 3.29, Figure 3.32 and Figure 3.33

Bright filed TEM micrographs were taken at different pulling distance and are shown in Figure 3.27, from which we can observe the interface migration. Analysis of corresponding SAD in Figure 3.28 reveals the new crystal to be α'-martensite with zone axis of [1-1-1]. There is no ε existing around.

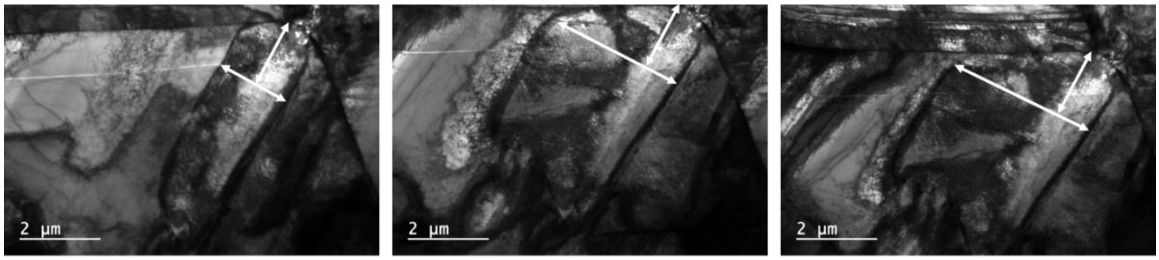

Figure 3.27 TEM of region 2 in figure 2 showing the growth of α' in 304L bar (sample 1)

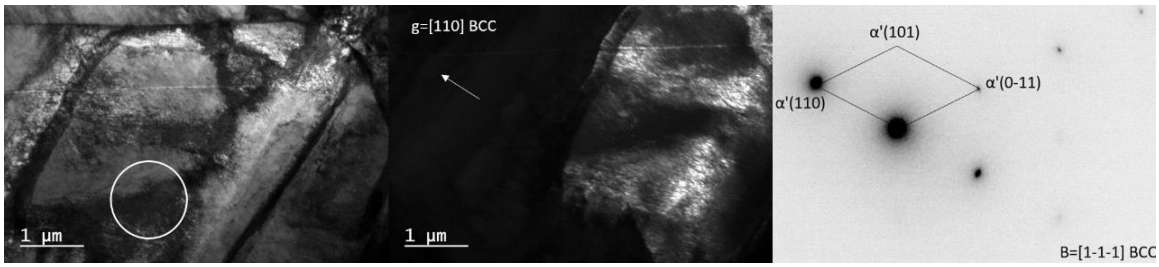

Figure 3.28 BF, DF TEM and SAD taken from region 2 showing the α' with zone axis of [1-1-1] at pulling distance to be 534.2um in 304L bar (sample 1)

This type of direct transformation was also recorded in another test. The steps are shown in Figure 3.29. The speed of the pulling stage is about 0.625um/s. The motion of

grain boundary is indicated by the white arrow. Speed of the interface motion is about 22nm/s. And the migration of the interface would stop when the pulling was stopped.

SAD taken from both sides of the interface are shown in Figure 3.30 and indicate the matrix to be γ e and newly formed phase to be α'. Based on the dark field TEM characterization, here the ε-martensite may be existing in the austenitic grain but rather than between α' and γ. So the transformation mechanism in this experiment should also be the direct transformation from γ to α without the assistance of ε plates.

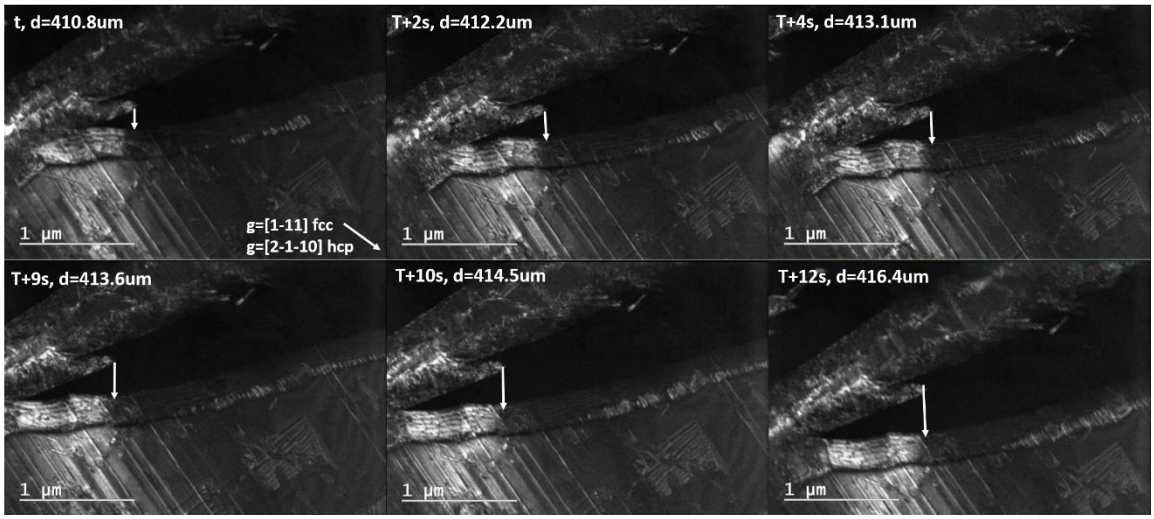

Figure 3.29 steps of interface migration in 304L bar (sample 5)

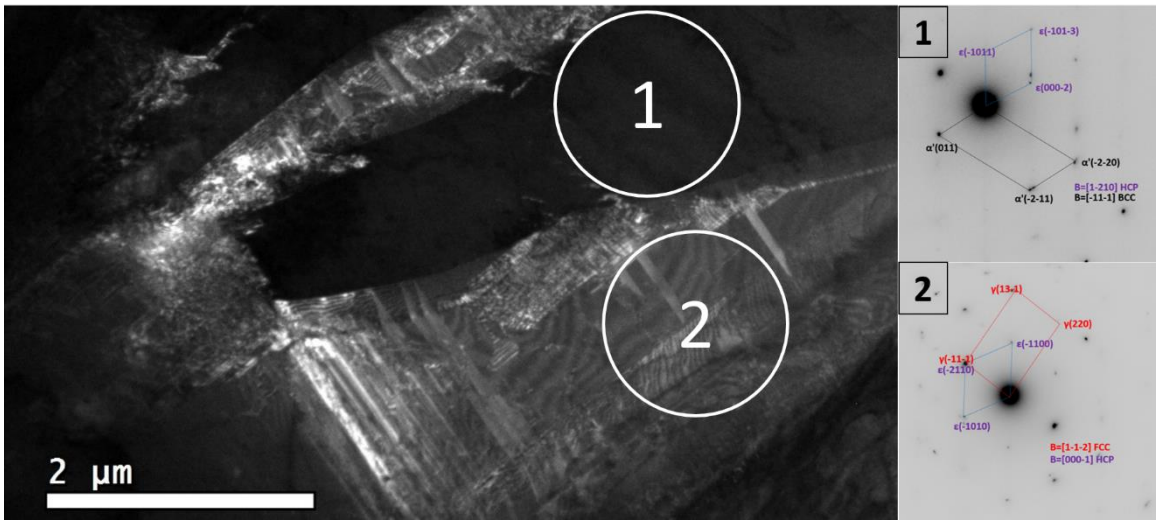

Figure 3.30 SADs taken from matrix and new phase

In Figure 3.31bright and dark filed TEM micrographs were taken at different pulling distance. Corresponding SADs indicated the formation of α'-martensite phase. α'-martensite may firstly nucleate in the austenitic grain. Then, with further straining, the newly formed α'-martensite divides the previous austenitic grain into two separated grains and continues growing into one austenitic grain. The zone axis of newly formed α'-martensite is [0-12] and the previous austenitic matrix is [-12-1].

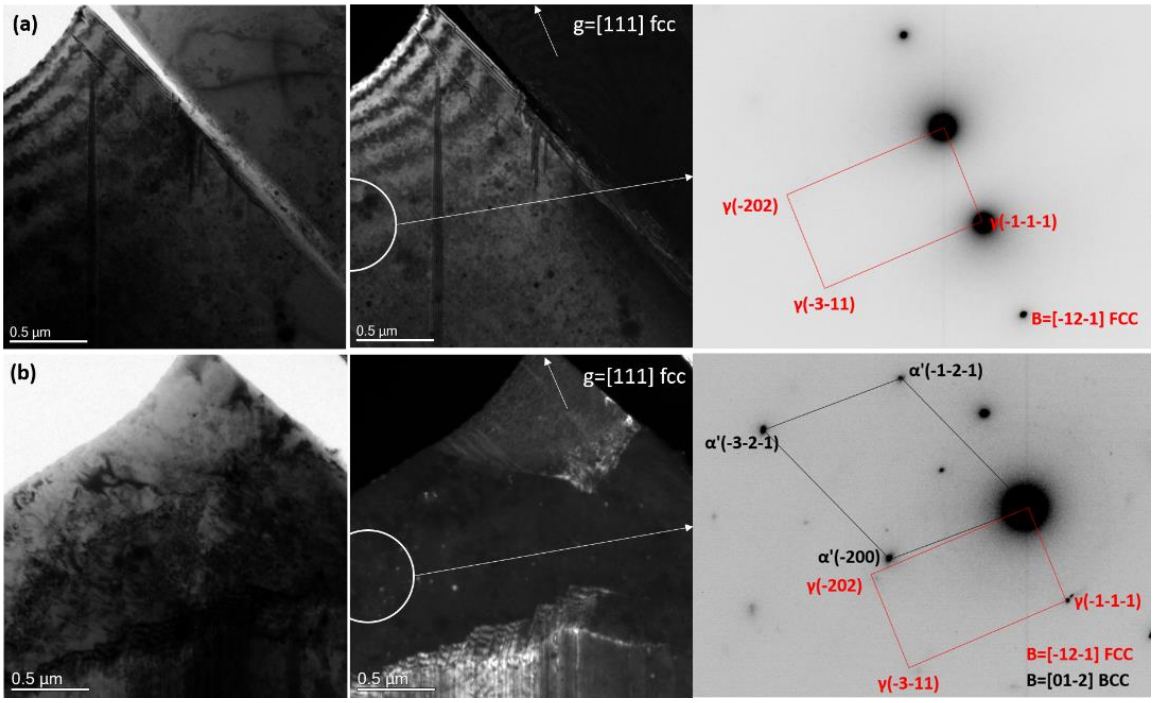

Figure 3.31 Bright field, dark field TEM and corresponding SAD from the same area at different strain level (a) d=644 um (b) d=811um in 304L bar (sample 2)

The details of martensitic transformation in Figure 3.31 were revealed by the in-situ straining video in Figure 3.32. Motion of the interface between α'-martensite and γ-austenite was recorded when the pulling distance was 709.9 um. The dark field TEM highlights the matrix γ-austenite. The elapsed time between the first and the last pictures is 6 seconds. The migration of the interface would stop when the pulling was stopped.

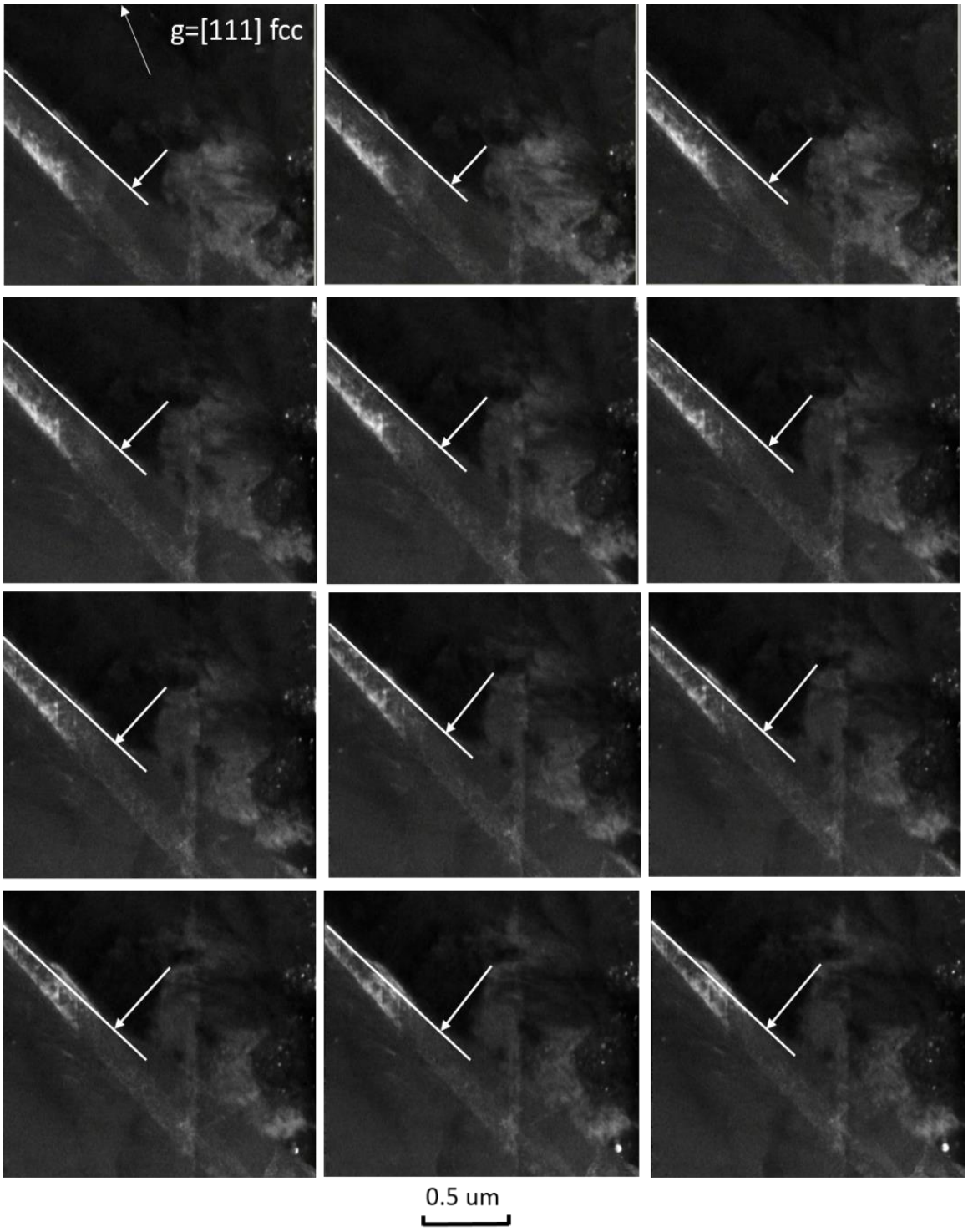

Figure 3.32 Steps of interface motion between α' and γ in 304L bar (sample 2)

In one 304L sample, one new crystal was observed at grain boundary between austenitic grains which is shown in Figure 3.33. Analysis of SAD in Figure 3.33 reveals

the crystal structure of the new phase to be bcc (α'-martensite). The dark filed TEM micrograph in Figure 3.33 also confirms the formation of α'.

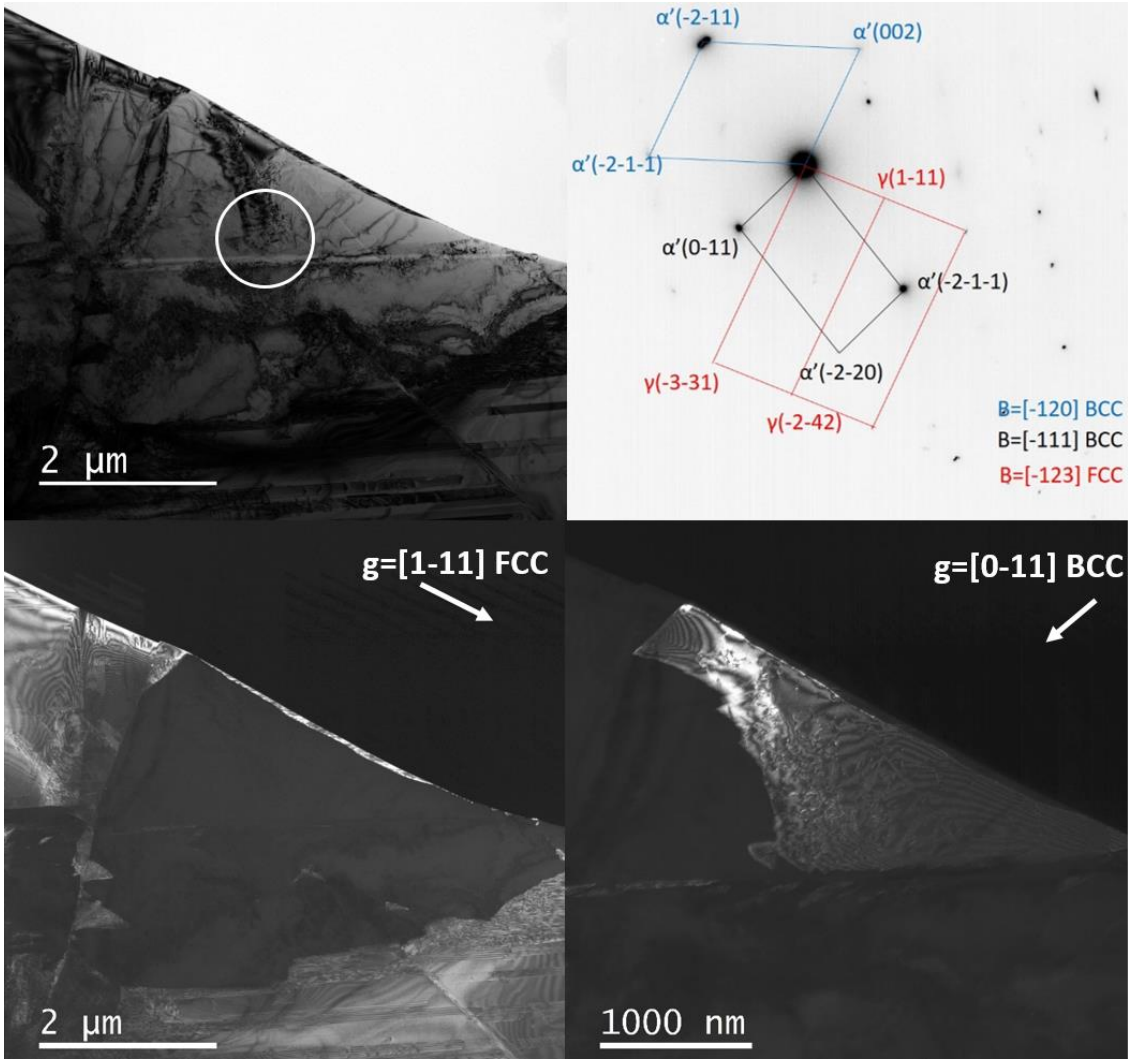

Figure 3.33 BF and DF TEM taken at pulling distance equal to 327um and SAD from the new crystal revealing the crystal structure to be α'-martensite in 304L bar (sample 6)

In another 304L bar sample, direct γ→ α'transformation without ε bands formed was also observed. The steps of interface migration are shown in Figure 3.35 using both bright filed and dark field imaging modes. Selected area diffractions in Figure 3.34 were taken from the new phase and the matrix.

In Figure 3.34, SAD 2 and SAD 3 were taken from the matrix besides the newly formed phase and show γ-austenite phase with zone axis of [-123] and [-12-1]. SAD 1 was taken from the new phase and shows the formation of α'-martensite with zone axis of [1-37] and ε-martensite with zone axis of [7-81-6]. The signals of γ-austenite in SAD 1 may come from the nearby austenitic grain. SAD 4 was taken from the interphase area between γ and α' and shows the formation of ε-martensite. The matrix and newly formed α'-martensite are also highlighted in the dark field TEM micrograph in Figure 3.34.

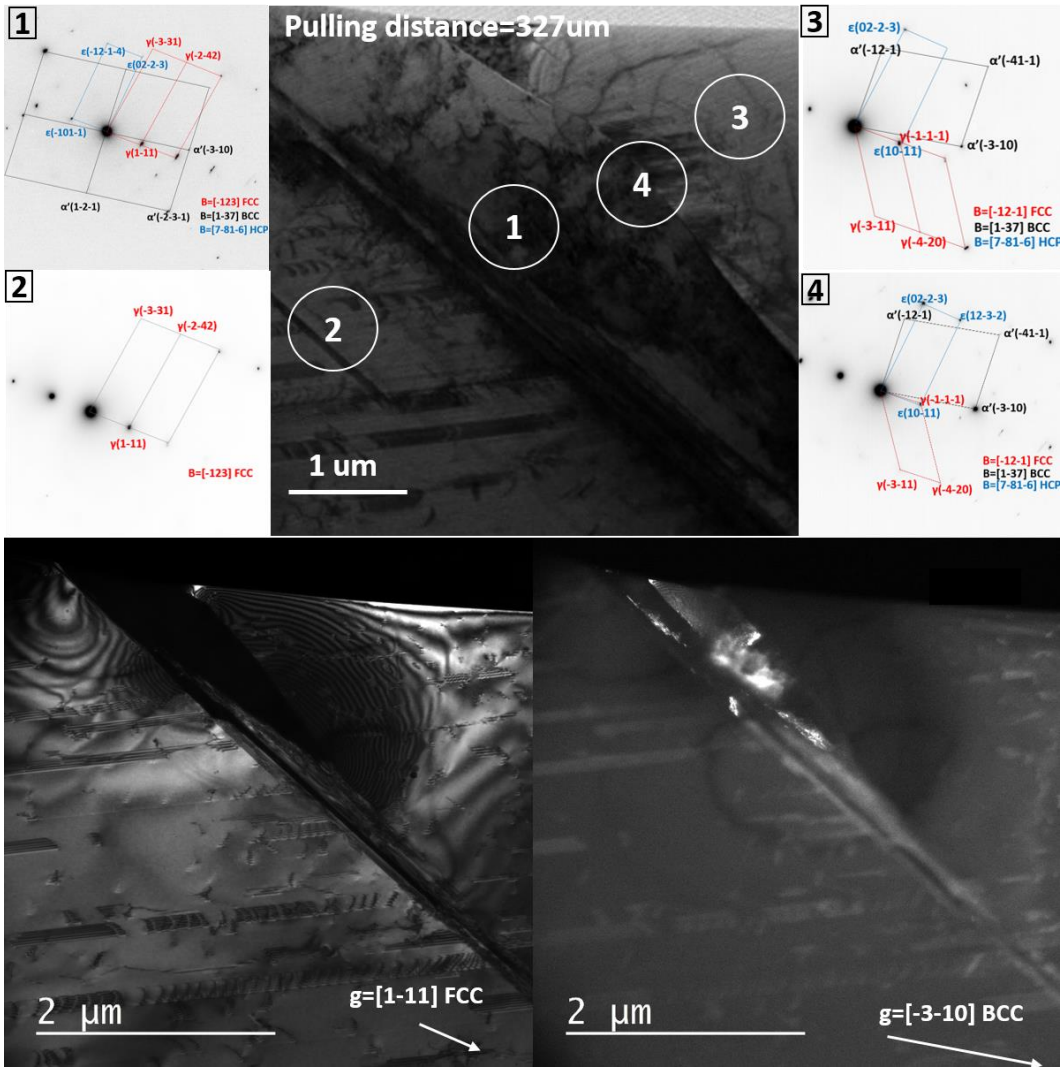

Figure 3.34 BF and DF TEM taken at pulling distance equal to 327um and SAD from different area revealing the crystal structure in (1),(3) the matrix phase and (2) the new phase in 304L bar (sample 6)

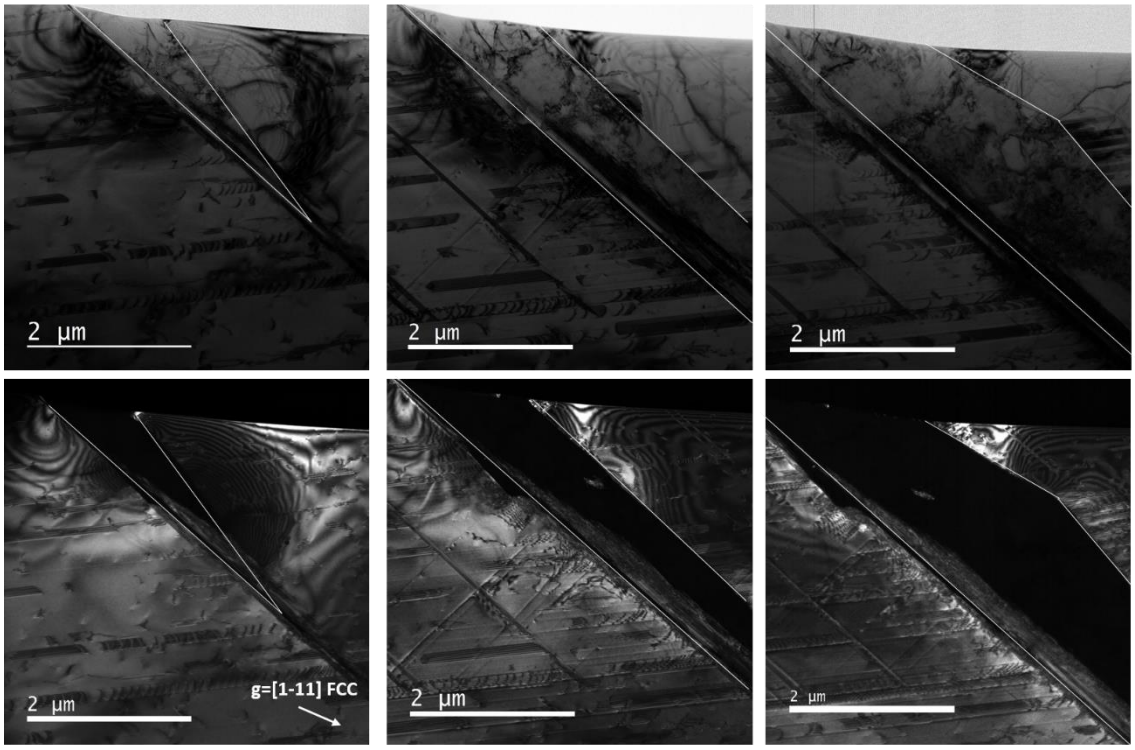

Figure 3.35 Steps of interface migration between γ and α' in 304L bar (sample 6)

3.5. In-Situ TEM Tensile Tests at Cryogenic Temperature

3.5.1. Evolution of stacking faults and formation of ε-martensite

At lower temperature, the SFE is expected to be lower than at room temperature [53, 58, 59]. In these series of experiments, tensile tests were done at cryogenic temperature ranging from 0°C to -100°C.

The nucleation sites for stacking faults seem to be random in the material with low SFE at cryogenic temperature. Figure 3.36 reveals the existence of stacking faults well dispersed in a large range area in 304L. These stacking faults may nucleate nearby the grain boundary, dislocation pile-ups and precipitates.

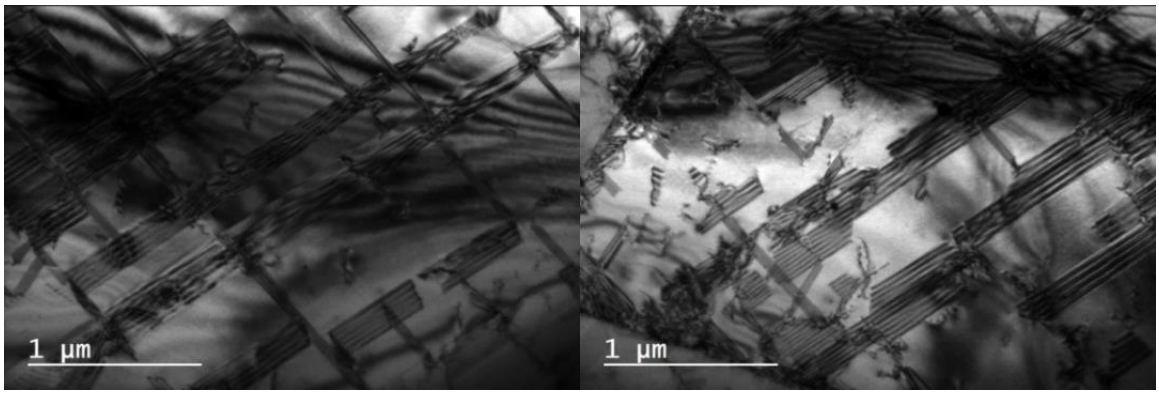

Figure 3.36 Formation of stacking faults at -50°C in 304L bar in 304L bar (sample 1)

The detailed processes of stacking faults are similar to those occurs at room temperature. The evolution of stacking faults in one austenitic grain was recorded when the pulling distance was 263um, which is shown in Figure 3.37.

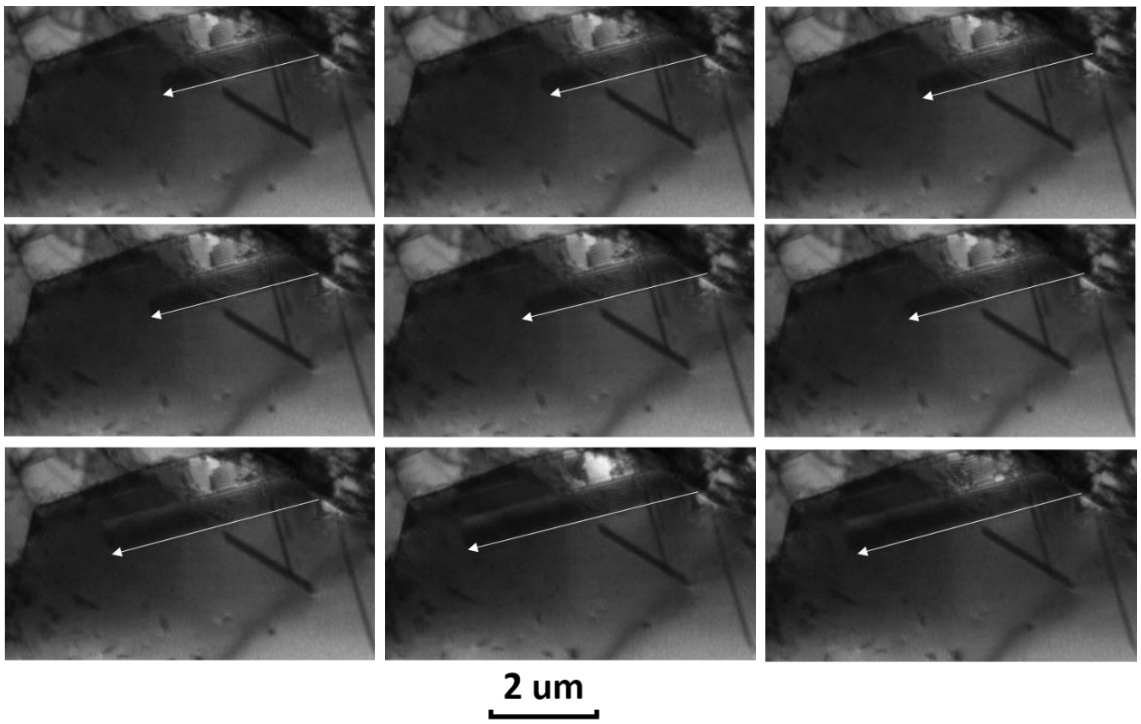

Figure 3.37 Stacking faults growth at cryogenic temperature in 304 sheet (sample 5)

Similar evolution of stacking is also shown in Figure 3.38. Stacking faults are observed to extend at -3.5°C when the pulling distance was 56.4um.

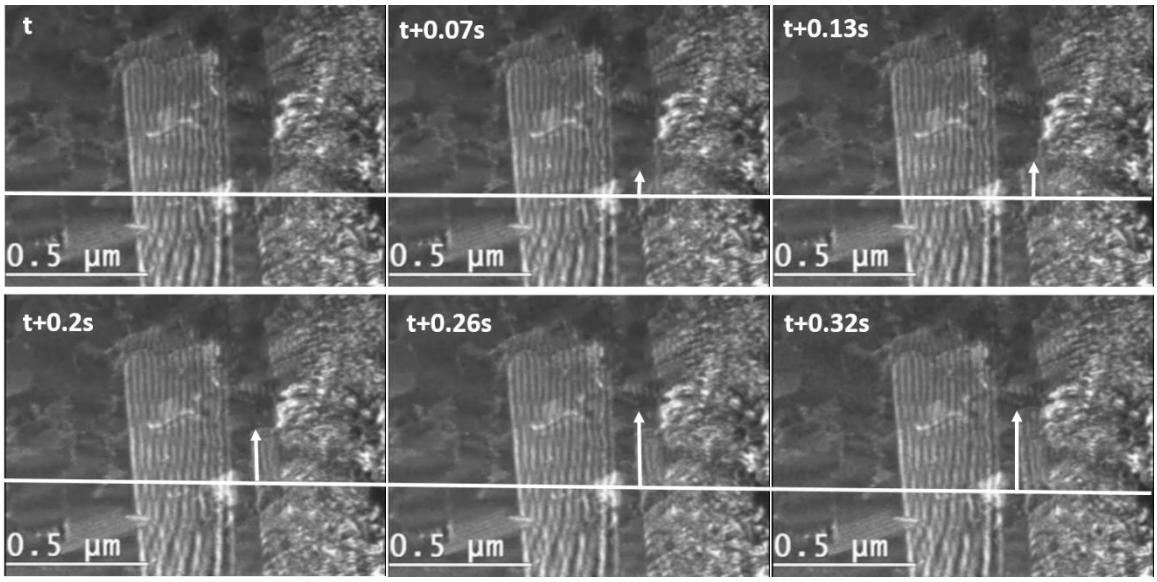

Figure 3.38 Steps of stacking faults growth at cryogenic temperature in 304L (sample 4)

The morphology of ε-martensite in austenitic matrix can be either perfect ε bands or stacking faults bundles. When the stacking faults overlap regularly on every second $(111)_\gamma$ plane, it can produce a perfect ε-martensite crystal structure[50]. When the overlapping is irregular, then it may result in a faulted ε-martensite[50]. In one of the cryogenic in-situ tensile tests, one small austenitic grain was characterized at different cooling stage. Corresponding SADs were taken to reveal the crystal structure changes, which are shown in Figure 3.39.

The sample was firstly cooled to 0°C. Bright and dark field TEM with SAD taken at this temperature are shown in Figure 3.39(a) revealing the matrix to be γ-austenite. Stacking faults seem to nucleate at grain boundary and grow across the austenitic grain. After cooling down to -6°C and keeping the sample at that temperature for 40 minutes, bright and dark TEM with SAD were taken from the same grain which are shown in Figure 3.39(b). The microstructure is heavily deformed with stacking fault bundles and ε-martensite as revealed by the SAD, which result from two different overlapping ways.

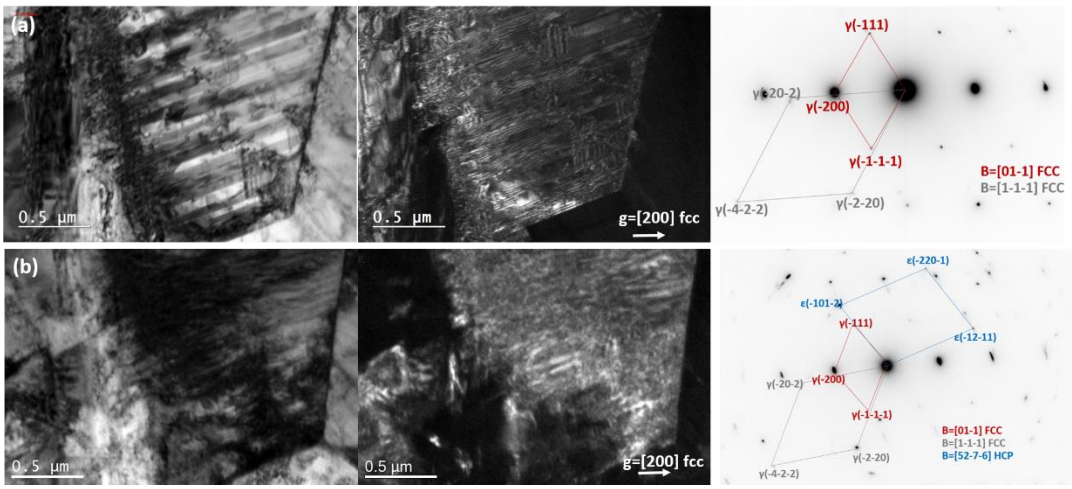

Figure 3.39 Formation of ε-martensite with zone axis of [52-7-6] in γ-austenite with zone axis of [01-1] and [1-1-1] (a) 39um, 0°C, (b) 56um, -6°C in 304L bar (sample 4)

This experiment gives us visible evidence that stacking faults can serve as the embryos for ε-martensite.

3.5.2. γ –austenite →α'-martensite

Similarly to room temperature, the direct γ→α' transformation at cryogenic temperature was also observed with the phenomenon of interface migration.

Pictures extracted from in-situ videos showing the direct transformation from γ to α' is shown in Figure 3.40 with the phenomenon of interface migration. The interface migration would stop as soon as the pulling was stopped.

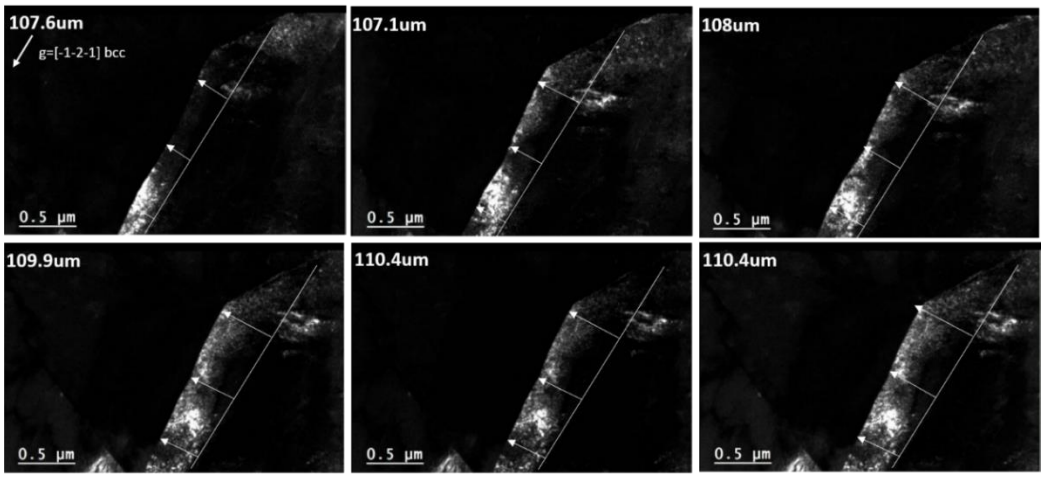

Figure 3.40 steps of interface migration in 304L bar (sample 3)

The position of the interface before and after the migration are shown in Figure 3.41. The speed of interface migration is about 0.1um/s while the pulling speed is about 2.0um/s. Corresponding SAD of the area in Figure 3.40 taken after the interface migration is shown in Figure 3.42. Analysis of SAD indicates the new phase to be α'-martensite. And there is no ε-martensite found.

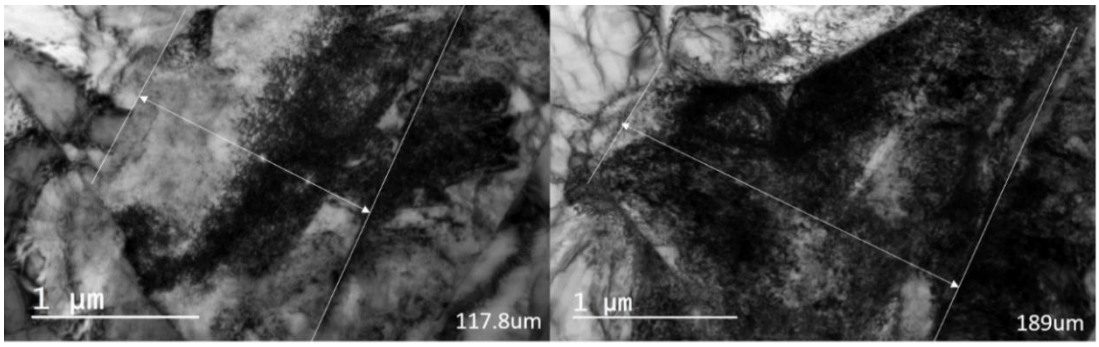

Figure 3.41 Initial and final position of interface in 304L bar (sample 3)

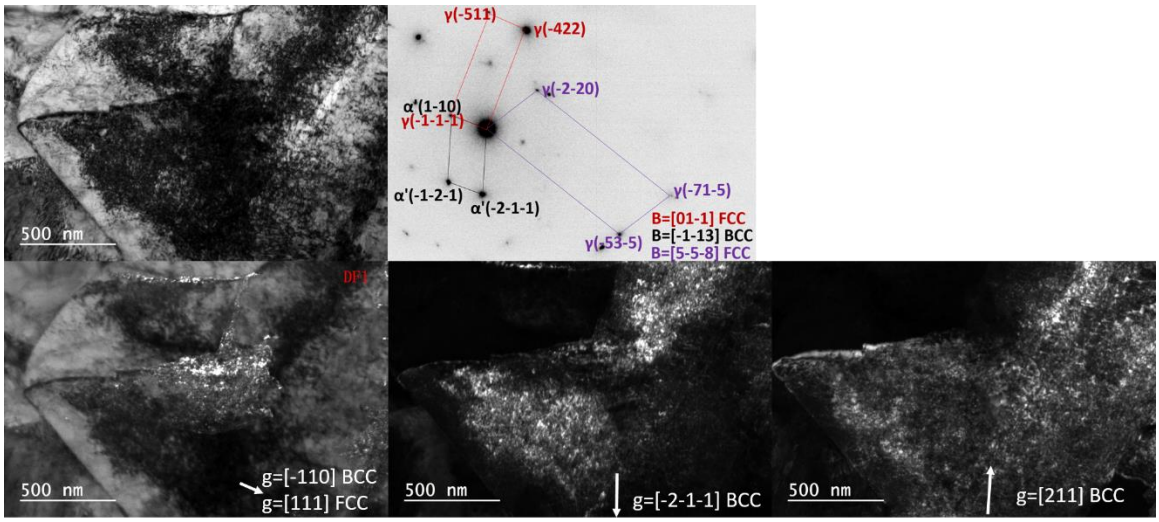

Figure 3.42 Formation of α'-martensite with zone axis of [-1-13] in γ-austenite with zone axis of [01-1] and [5-5-8] at pulling distance 189um in 304L bar (sample 3)

This type transformation mechanism is also proved by the pictures extracted from in-situ videos in Figure 3.43. Interface migration was recorded during the cooling experiment with limited strain. The sample was hold at a pulling distance of 73 um,

instead of inducing more straining, sample was further cooled. The migration of interface was observed when the sample was cooled from -7°C to -14.9°C. The motion speed is about 0.2um/s. α' may firstly nucleate between at the grain boundary. Subsequently, it grew into γ with the phenomenon of interface migration.

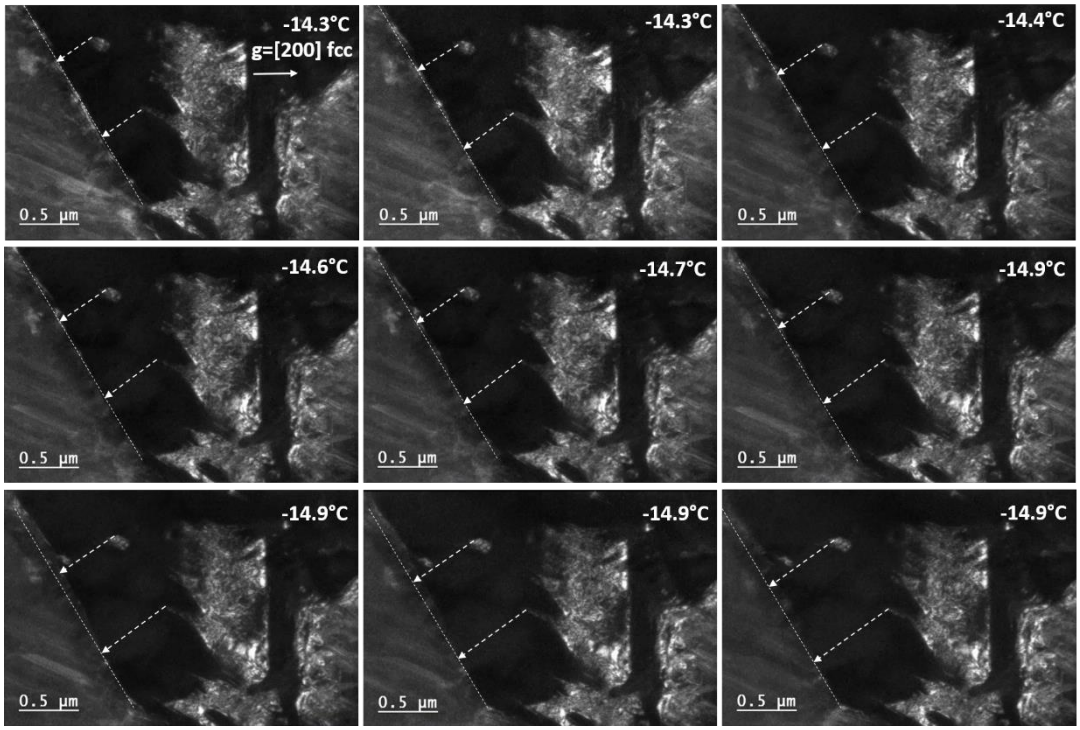

Figure 3.43 Steps of interface migration during cooling process with strain in 304L bar (sample 4) from -14.3°C to -14.9°C

CHAPTER 4

CONCLUSIONS

Both ex-situ and in-situ methods were used in this work to investigate the mechanism of deformation-induced martensitic transformation in 304SS samples at different temperatures.

Uniaxial tensile tests were conducted on bulk samples under a strain rate of $10^{-3}s^{-1}$ until rupture, followed by microstructure investigation using TEM and XRD. Some samples were interrupted after reaching a strain of 7%, 18%, and 30% with the goal of investigating the intermediate microstructure.

The initial microstructure in form of cold rolled sheets already contains a fraction of α'-martensite (bcc) as shown by XRD analysis and the presence of stacking faults. At 7% strain, there seems to be some reverse phase transformation from α'martensite to γ-austenite as the relative intensity of the peaks of martensite decreases relative to the austenite peak e.g. with further straining (18% and 30%), martensitic transformation occurs again and the intensity of the α'-martensite peaks increase relative to the intensity of the austenite peaks.

TEM characterization of the interrupted samples shows presence of stacking faults throughout the material and regions of ε-martensite (hcp) as well as some α'-martensite (bcc) at 7% strain. At higher strain level, stacking faults are not easy to distinguish anymore. At 18%, stacking faults are indeed less easy to discern, and ε-

martensite (hcp) and α'-martensite (bcc) are easily found under TEM. Compared with the samples strained to 7% and 18%, discernable stacking faults are even harder to observe in the 30% strain-interrupted sample and more martensite is more readily found during the TEM examination.

As far as temperature effect, the XRD analysis confirms that the fraction of martensite in the fractured samples decreases as the testing temperature increases (from 25°C to 100°C). In terms of mechanical properties, the Stress-Strain curve at 25°C shows an acceleration of the strain hardening rate (marked by an inflection point on the S-S curve typical of TRIP alloys) around 18-20% strain, which is not observed at 50°C and 100°C. The UTS decreases with temperature, which can be related to the smaller amount of martensite formed at those higher temperature.

In complement to the ex-situ investigation, tensile tests were conducted in-situ in a TEM at 25°C down to cryogenic temperatures (-100°C) using a special straining-stage with the goal of capturing the growth of the martensitic phase as it develops under stress in the material. Through such experiments, it was observed that the austenitic phase γ (fcc) can transform into both ε-martensite (hcp) and α'-martensite (bcc), and ε-martensite (hcp) can further transform into α'-martensite (bcc).

Regardless of the temperature, stacking faults (SFs) were observed to form as an intermediate step during the transformation from γ-austenite to the ε-martensite. They usually originated from grain boundaries. Their formation and growth could be readily captured in-situ due to the relatively low stacking fault energy of 304 stainless steels. Whether further transformation (into ε -martensite) occurred or not depended on either further cooling or further straining or the combination of these two conditions.

In the case where ε-martensite formed, it could further transform into α'-martensite as evidenced in some cases by the evolution of the diffraction pattern. As an alternative, ε-martensite shear bands could also serve a nucleation sites for α' which will grow into the γ matrix- in which case, interface migration was also observed. α'-martensite was also observed to nucleate at austenite grain boundaries and then grew into the γ matrix. When such direct transformation of γ austenite phase into α'-martensite occurred directly during the in-situ experiments, the interface was observed to migrate upon pulling the sample and stopped when the stage was at rest, indicating that the transformation was a direct effect of the strain applied.

At cryogenic temperature, the formation and growth of SFs was observed in situ. Three cases of transformations were witnessed: (i) the case where accumulation of SFs resulted in formation of ε- martensite (γ →SFs →ε), (ii) the case where γ transformed into α' directly (with interface migration upon pulling the sample) γ→ α' and (iii) the case where after inducing some stress in the sample by pulling at -7°C, the γ→ α' transformation occurred upon further cooling from -7°C to -14.9°C (no further pulling), indicating again how stress and temperature are both effective on the transformation.

In-situ tensile TEM as a new method was applied to study the martensitic transformation which can capture and characterize the microstructure changes as the martensitic transformation processing. Thanks to this work, in-situ tensile TEM, as a small scale tensile technique, is proved to be a useful and effective tool for investigating mechanisms of phase transformations as shown here, which may also be applied in studying phase transformation in other alloys to provide the kinetics information.

REFERENCES

1. Cunat, P.-J., Alloying elements in stainless steel and other chromium-containing alloys. International Chromium Development Association, 2004. 45(6): p. 122-131.

2. Hedström, P., Deformation induced martensitic transformation of metastable stainless steel AISI 301. 2005, Luleå University of Technology.

3. Lippold, J. C., Kotecki, D. J., Welding Metallurgy and Weldability of Stainless Steels. 2005: Wiley.

4. Linderov, M., et al., Deformation mechanisms in austenitic TRIP/TWIP steels at room and elevated temperature investigated by acoustic emission and scanning electron microscopy. Materials Science and Engineering: A, 2014. 597(0): p. 183-193.

5. Bhadeshia, H.K.D.H., TRIP-Assisted Steels. ISIJ International, 2002. 42(9): p. 1059-1060.

6. Grässel, O. and Frommeyer, G., Effect of martensitic phase transformation and deformation twinning on mechanical properties of Fe–Mn–Si–AI steels. Materials Science and Technology, 1998. 14(12): p. 1213-1217.

7. Kovalev, A., et al., Characterization of the TRIP/TWIP effect in austenitic stainless steels using Stress-Temperature-Transformation (STT) and Deformation-Temperature-Transformation (DTT) Diagrams. Steel Research International, 2011. 82(1): p. 45-50.

8. Dumay, A., et al., Influence of addition elements on the stacking-fault energy and mechanical properties of an austenitic Fe–Mn–C steel. Materials Science and Engineering: A, 2008. 483–484(0): p. 184-187.

9. Allain, S., Chateau, J.P. and Bouaziz, O., A physical model of the twinning-induced plasticity effect in a high manganese austenitic steel. Materials Science and Engineering: A, 2004. 387–389(0): p. 143-147.

10. Hokka, M., et al. Characterization of strain rate and temperature dependent mechanical behavior of TWIP steels. Journal de Physique IV (Proceedings). 2006. EDP sciences.

11. Ashbya, M. and Smidmana, M., Materials for nuclear power systems. 2011.

12. 304, 304L and 304H grade Data Sheet. Available from: http://www.atlassteels.com.au/documents/Atlas_Grade_datasheet_304_rev_Jan_2011.pdf. 13. Product Data Sheet. STAINLESS STEEL GRADE 304 VS 304L [cited 2016 05/26]; Available from: http://www.australwright.com.au/technical-data/advice/stainless-steel/grade-304-vs-304l/.

14. Hahnenberger, F., Smaga, M. and Eifler, D., Microstructural investigation of the fatigue behavior and phase transformation in metastable austenitic steels at ambient and lower temperatures. International Journal of Fatigue, 2014. 69(0): p. 36-48.

15. Bhadeshia, H.K.D.H. Martensite in Steels. Available from: http://www.msm.cam.ac.uk/phase-trans/2000/C9/lectures45.pdf.

16. Nishiyama, Z., Introduction to Martensite and Martensitic Transformation, in Martensitic Transformation, 1978, Academic Press. p. 1-13.

17. Martensite and Martensitic Phase Transformations. Available from: http://www.msm.cam.ac.uk/phase-trans/2002/martensite.html.

18. Das, A., et al., Morphologies and characteristics of deformation induced martensite during low cycle fatigue behaviour of austenitic stainless steel. Materials Science and Engineering: A, 2011. 528(27): p. 7909-7914.

19. Olson, G. and Cohen, M., A mechanism for the strain-induced nucleation of martensitic transformations. Journal of the Less Common Metals, 1972. 28(1): p. 107-118.

20. Maxwell, P.C., Goldberg, A., and Shyne, J.C., Influence of martensite formed during deformation on the mechanical behavior of Fe-Ni-C Alloys. Metallurgical Transactions, 1974. 5(6): p. 1319-1324.

21. Lecroisey, F. and Pineau, A., Martensitic transformations induced by plastic deformation in the Fe-Ni-Cr-C system. Metallurgical Transactions, 1972. 3(2): p. 391-400.

22. Das, A., et al., Morphologies and characteristics of deformation induced martensite during tensile deformation of 304 LN stainless steel. Materials Science and Engineering: A, 2008. 486(1–2): p. 283-286.

23. Das, A. and Tarafder, S., Experimental investigation on martensitic transformation and fracture morphologies of austenitic stainless steel. International Journal of Plasticity, 2009. 25(11): p. 2222-2247.

24. Shen, Y.F., et al., Twinning and martensite in a 304 austenitic stainless steel. Materials Science and Engineering: A, 2012. 552(0): p. 514-522.

25. De, A.K., Speer, J.G. and Matlock, D.K., Deformation-Induced Phase Transformation and Strain Hardening in Type 304 Austenitic Stainless Steel. Metallurgical & Materials Transactions. Part A, 2006. 37(6): p.1875-1886.

26. Tomota, Y., et al., Tensile behavior of TRIP-aided multi-phase steels studied by in situ neutron diffraction. Acta Materialia, 2004. 52(20): p. 5737-5745.

27. Li, N., et al., In situ X-ray microdiffraction study of deformation-induced phase transformation in 304 austenitic stainless steel. Acta Materialia, 2014. 64(0): p. 12-23.

28. Nishiyama, Z., Crystallography of Martensite (General), in Martensitic Transformation. 1978, Academic Press. p. 14-134.

29. Eichelman, G.H., Hull, F.C., the Effects of Composition on the Temperature of Spontaneous Transformation of Austenite to Martensite in 18-8 Type Stainless Steels, in Transactions: American Society for Metals. 1953. p. 77-104.

30. Monkman, F.C., Cuff, F.B. and Grant, N.J., Computation of Ms for Stainless Steels. Metal Progress, 1957. 71(04): p. 94.

31. Pickering, F.B., Physical metallurgy and the design of steels. 1978: Applied Science Publishers.

32. The Journal of the Iron and Steel Institute. 1954: Iron and Steel Institute.

33. Gladman, T., Hammond, J., Marsh F.W., Austenitic stainless steels for cold forming. Sheet Metal Industries, 1974. 51(5): p. 219.

34. Sjoberg, J., Influence of Analysis on the Properties of Stainless Spring Steel. Wire, 1973. 23(4): p. 4.

35. Nohara, K., Ono, Y. and Ohashi N., Strain induced martensitic transformation in metastable austenitic stainless steel in multi stage tensile deformation at various temperatures. Proceedings of the first JIM International Symposium, 1976: p. 6.

36. Nohara, K., Ono, Y., and Ohashi, N., Composition and Grain Size Dependencies of Strain-induced Martensitic Transformation in Metastable Austenitic Stainless Steels. Tetsu-to-Hagane, 1977. 63(5): p. 772-782.

37. Olson, G.B. and Cohen, M., Kinetics of strain-induced martensitic nucleation. Metallurgical Transactions A, 1975. 6(4): p. 791-795.

38. Spencer, K., et al., The strain induced martensite transformation in austenitic stainless steels: Part 1 – Influence of temperature and strain history. Materials Science and Technology, 2009. 25(1): p. 7-17.

39. Curtze, S., et al., Thermodynamic modeling of the stacking fault energy of austenitic steels. Acta Materialia, 2011. 59(3): p. 1068-1076.

40. Xu, Y., Martensitic Transformation and Martensite. 1999: Science Publisher.

41. Kurdjumow, G. and Sachs, G., Über den Mechanismus der Stahlhärtung. Zeitschrift für Physik, 1930. 64(5-6): p. 325-343.

42. Nishiyama, Z., Shimizu, K. and Morikawa, S., Transmission electron microscopic observation of the martensite transformation in 304-type stainless steel. Journal of the Japan Institute of Metals, 1963. 27(10): p. 497-502.

43. Wasserman, G., Arch. Eisenhuttenwea, 1933. 16: p. 647.

44. Nishiyama, Z., Rep. Tohoku Univ., 1934(23): p.637-664

45. Greninger, A.B, Troiano, A.R., Transactions AIME. Vol. 145. 1941.

46. Shoji, H., Z. Kristallogr, 1931. 77: p. 381.

47. Nishiyama, Z., Sci. Rep. Tohoku Imp. Univ, 1936. 25.

48. Talonen, J., Nenonen, P. and Pape, G., Effect of strain rate on the strain-induced γ →α'-martensite transformation and mechanical properties of austenitic stainless steels. Metallurgical & Materials Transactions. Part A, 2005. 36(2): p. 421-432.

49. Lehnhoff, G.R. and Findley, K.O., The martensitic transformation and strain-hardening behavior of austenitic steels during fatigue and tensile loading. Journal of Materials, 2014. 66(5): p. 756-764.

50. Talonen, J. and Hänninen, H., Formation of shear bands and strain-induced martensite during plastic deformation of metastable austenitic stainless steels. Acta Materialia, 2007. 55(18): p. 6108-6118.

51. Byun, T.S., On the stress dependence of partial dislocation separation and deformation microstructure in austenitic stainless steels. Acta Materialia, 2003. 51(11): p. 3063-3071.

52. Schramm, R.E. and Reed, R.P., Stacking fault energies of seven commercial austenitic stainless steels. Metallurgical Transactions A, 1975. 6(7): p. 1345-1351.

53. Wan, J., Chen, S. and Xu Z., The influence of temperature on stacking fault energy in Fe-based alloys. Science in China Series E: Technological Sciences, 2001. 44(4): p. 345-352.

54. Zhang, M. X., et al., Crystallography of the Simple HCP/FCC System. Metallurgical and Materials Transactions A, 2008. 39(5): p. 1077-1086.

55. Nishiyama, Z., X-ray investigation of the mechanism of the transformation from face centered cubic lattice to body centered cubic. Sci. Rep. Tohoku Univ, 1934. 23: p. 637-664.

56. Talonen, J., Effect of strain-induced α'-martensite transformation on mechanical properties of metastable austenitic stainless steels. 2007.

57. Luo, K.Y., et al., Effects of laser shock processing on mechanical properties and micro-structure of ANSI 304 austenitic stainless steel. Materials Science and Engineering: A, 2011. 528(13–14): p. 4783-4788.

58. Klein, M.J., The effect of temperature on stacking fault energies derived from X-ray diffraction analyses. Scripta Metallurgica, 1967. 1(2): p. 65-69.

59. Rémy, L., Pineau, A. and Thomas, B., Temperature dependence of stacking fault energy in close-packed metals and alloys. Materials Science and Engineering, 1978. 36(1): p. 47-63.